UNIVERSIDADE FEDERAL DO RIO GRANDE DO SUL
INSTITUTO DE FÍSICA
PROGRAMA DE PÓS-GRADUAÇÃO EM FÍSICA

GUILHERME MÜLLER PECCINI

Exclusive processes described by QCD at electron-ion colliders*
(Processos exclusivos descritos pela QCD em colisores elétron-íon)

Porto Alegre
2022

*This work was financed by the Brazilian funding agency CNPq.

GUILHERME MÜLLER PECCINI

Exclusive processes described by QCD at electron-ion colliders*

(Processos exclusivos descritos pela QCD em colisores elétron-íon)

Doctoral Thesis submitted to the Institute of Physics at Federal University of Rio Grande do Sul in candidacy for the degree of Doctor in Science.

Research area: High Energy Physics Phenomenology.

Supervisor: Dr. Magno Valerio Trindade Machado

Porto Alegre

2022

I dedicate this work to my beloved mother Nádia. I am sure that my passion for physics was inherited from her...

Acknowledgments

First of all, I would to like to express my gratitude to my advisor, Prof. Magno Valerio Trindade Machado, who has been always available and willing to help whenever necessary. His strong knowledge in particle physics and corresponding literature has been crucial for the development of this work.

Secondly, I am quite grateful to Lucas Soster Moriggi. We could build a strong collaboration and so far have already published five papers in high-impact scientific journals.

I am also thankful to Profs. Daniel A. Fagundes (UFSC - Brazil), Emmanuel G. de Oliveira (UFSC - Brazil), Hannes Jung (DESY - Germany), Igor Ivanov (Technical University of Lisbon - Portugal) and Wolfgang Schäfer (Institute of Nuclear Physics - Poland) for collaboration and fruitful correspondence throughout the realization of our papers.

For these difficult times, we should follow what Martin Luther King once said: "We must accept finite disappointment, but never lose infinite hope."

Abstract

In this work we aim to investigate electron-ion collisions, a highly important type of process with huge potential to deeply study the structure of matter. In particular, three processes that involve eA collisions are analyzed: diffractive gluon jet production, timelike Compton scattering (TCS) and exclusive Z^0 production. All of them and their corresponding observables are calculated at the center-of-mass energies of upcoming and planned future electron-ion machines, namely the EIC (Electron-Ion Collider), the LHeC (Large Hadron electron Collider) and the FCC (Future Circular Collider). The measurement of diffractive gluon jets opens the possibility of extracting the saturation scale from the experiments, which would be quite relevant for the phenomenology associated with the field of high energy physics. Regarding the TCS, it is performed in eA collisions using the k_T-factorization formalism for the first time. The computed predictions will be highly useful for future comparisons against measured data at these machines, leveraging the study and investigation of the structure of matter through electron-ion collisions. Finally, the Z^0 production is a traditional baseline SM signal and investigating this process within electron-ion collisions may be quite advantageous since it has a clear experimental signature if compared to the Z^0 signal coming from hadroproduction and is also perturbatively calculable with not so large uncertainties due to the high mass of the boson.

Keywords: Quantum chromodynamics, electron-ion collisions, diffractive gluon jet production, timelike Compton scattering, exclusive Z^0 production.

Resumo

Neste trabalho buscamos estudar as colisões elétron-ion, um processo altamente importante e que tem grande potencial de realizar uma investigação profunda da estrutura da matéria. Em particular, três processos que envolvem colisões eA são analisados: produção difrativa de jatos de glúons, espalhamento do tipo-tempo (em inglês, timelike Compton scattering - TCS) e produção exclusiva de Z^0. Todos esses processos e observáveis correspondentes são calculados nas energias de centro de massa de futuras máquinas elétron-ion, como por exemplo o Colisor Elétron Íon (em inglês, Electron-Ion Collider - EIC), o Grande Colisor elétron Hádron (em inglês, Large Hadron electron Collider - LHeC) e o Futuro Colisor Circular (em inglês, Future Circular Collider - FCC). Medidas de jatos difrativos de glúons possibilitam que se extraia a escala de saturação dos experimentos, o que seria extremamente relevante para a fenomenologia associada à física de altas energias. Em relação ao TCS, esse é realizado em colisões eA utilizando-se o formalismo de fatorização k_T pela primeira vez. As predições calculadas nesses processos serão muito úteis para futuras comparações com dados medidos nessas máquinas citadas acima, potencializando o estudo da estrutura da matéria através de colisões elétron-ion. Por fim, a produção de Z^0 é um tradicional parâmetro de sinal do Modelo Padrão (em inglês, Standard Model - SM) e investigar esse processo no contexto de colisões elétron - íon pode ser bem vantajoso uma vez que possui um sinal claro de assinatura em comparação ao proveniente de hadroprodução e também é calculável perturbativamente com incertezas não muito grandes devido à alta massa do bóson.

Palavras-chave: Cromodinâmica quântica, colisões elétron-íon, produção de jatos difrativos de glúons, espalhamento do tipo-tempo, produção exclusiva de Z^0.

Contents

1 Introduction

The field of nuclear science is concerned to explore and investigate the nuclear content of the atoms. The nucleus is composed by protons and neutrons, being these latter referred as nucleons. About one hundred years ago scientists were studying the atom's structure, which led to the development of chemistry, electronic devices and basically all the technologies that we have nowadays. Now, the scales are much smaller since we are looking into the objects that compose those protons and neutrons.

Investigations along the 60's and 70's (see a review about that in Ref. [1]) revealed that nucleons are composed by fundamental particles called quarks that interact via the exchange of gluons. Such investigations gave rise to the fundamental theory of strong interactions, the Quantum Chomodynamics (QCD) [2], which is one of the cornerstones of the Standard Model (SM) of particle physics. The latter is the theory that describes matter and its interaction (except the gravitation) in nature and encompasses QCD along with the other two theories that address the electromagnetic and weak forces, i.e., Quantum Electrodynamics (QED) and Electroweak Theory, respectively. Unlike the QED in which the photons have no electric charge, in QCD gluons carry color charge and such fact enables them to interact with themselves. This mechanism of self-interaction among gluons assigns to QCD a high complexity whether compared to QED. Thanks to new experimental facilities and their increasing collision energies throughout the last decades, several QCD phenomena not directly evident in the Lagrangian density have been enlightened. Such phenomena include color confinement[1] and chiral symmetry breaking[2], for instance.

Albeit its remarkable success, the SM has major problems, what can be outlined through the following questions [3]:

- **Elementary particles:** The SM is composed by 61 particles: 36 quarks and anti-quarks, 12 leptons, 12 interaction mediators and 1 Higgs boson. Are there more particles to be discovered? Do right-handed neutrinos exist? What makes quarks and leptons different? Do leptonquarks exist?

[1] Color confinement is a phenomenon that color charged particles (quarks and gluons) are not able to exist as isolated objects. However, if a temperature of about 2 TK is achieved (known as Hagedorn temperature), such objects deconfine and originate the Quark-gluon Plasma (QGP).

[2] Chiral symmetry breaking is a spontaneous symmetry breaking of a chiral symmetry related to a gauge theory such as QCD, for example. It is observed at experiments where masses of the octet of pseudoscalar mesons(the pion, for instance) are much lighter than the next heavier states of the octet of vector mesons (as is the case of the rho meson, for example).

- **Strong interactions:** How to explain color confinement and how partons hadronize? What is the real parton dynamics in the proton, in other hadrons and inside nuclei? How can QCD elementary fields describe the many bodies of QGP (Quark-gluon plasma)[3]?
- **Dark matter:** Is dark matter composed of elementary particles or does it have a different origin? What about hidden and dark sectors? Do they exist? If yes, how would they be detected at experiments?
- **GUT[4]:** Is there a unification of the interactions at high scales? Would it include gravitation? What is the correct value of the strong coupling constant? Is Lattice QCD[5] correct about that? Is the proton a stable object?
- **Neutrinos:** What about sterile and Majorana neutrinos? Do they exist? Is there CP violation[6] in the neutrino sector?

The questions above, among others, are still open in particle physics and therefore demand further investigation.

Despite the phenomenological success of the SM, the research in particle physics is far from its end. As pointed out above, many questions remain open and their answers elusive. Furthermore, countless periods of revolution in science throughout the history led us to realize that declaring a theory as finished is in contradiction with past experience. Theoretical hypothesis such as SUSY particles[7], extra dimensions, unparticles, embedding on higher gauge groups (like E8[8]) are strong reasons to keep evolving the efforts towards high energy physics. In this context, it is needed a substantial increase of energy, precision

[3] The Quark-gluon plasma is a state of the matter in which quarks and gluons are freed of their strong attraction for each other. Such state is only achievable at extremely high energy densities, the same conditions present in the early Universe.

[4] GUT is the acronym for Grand Unified Theory, which is a model in particle physics that predicts that, at very high energies, the three gauge interactions (strong, electromagnetic and weak) would merge into a single one.

[5] Lattice QCD is a method for solving the QCD Lagrangian by means of discretizing space-time. After the numerical solution evaluation, the continuum QCD is recovered.

[6] CP violation is the breaking of C-P (charge-parity) symmetry and it states that physics laws should remain unalterable when a particle is interchanged with its antiparticle (C-symmetry) while its spacial coordinates are reversed (P-symmetry).

[7] In few words, SUSY (acronym for Supersymmetry) is an extension of the SM that is intended to fill some of its gaps. It predicts that every particle in the SM has a partner particle. These new particles would fix the mass of the Higgs boson and resolve a major issue in the SM.

[8] An Exceptionally Simple Theory of Everything, commonly denoted as E8, aims to describe all the fundamental interactions in the SM plus the gravitation in terms of quantum excitations of a single Lie group geometry, the E8 group.

and kinematic coverage at upcoming and future machines in order to enable deeper analyses on the issues cited above [3].

Lattice QCD shows that the complex structures of the QCD vacuum are due to gluon dynamics, which are the objects responsible for intermediating the strong interactions, as are the photons in the case of QED. The self-interactions between gluons determine all the essential properties of QCD and leads to the fact that gluons dominate the structure of matter. For example, 98% of the nuclear matter is due to gluon interactions. Nevertheless, most part of gluon properties in matter remains unexplored. It is necessary to perform high energy probes to execute a profound investigation and explore gluon dynamics experimentally. The accelerators DESY-HERA[9], BNL-RHIC[10], Fermilab-Tevatron[11] and CERN-LHC [12] have highly increased both the theoretical and the experimental understandings concerning the behavior of gluons. In general, lepton beams are ideal probes of gluons through DIS (Deep Inelastic Scattering) processes. The gluonic part embedded in the wave function modifies the well known electromagnetic interaction, which allows one to infer the gluon properties. In order to obtain a precise inference, DIS should be performed within a large range of energies and scattering angles (also, using different kinds of targets). Experimental results of DIS at HERA of electron-proton collisions constrained further the structure function of the proton in the longitudinal and transverse directions, especially at small momentum fraction of the partons with respect to the hadron. This was a completely new domain of measurement reached until then. Data showed evidence that gluons were by far the most dominant parton, by over an order of magnitude [4]. In particular, the results revealed that the increase of gluons in the region of small momentum fractions, x, presented unlimited behavior, as predicted by linear QCD equations. However, there is an upper limit on the total cross section, where the hadron behaves as a "Black-disk", given by $\sigma_{tot} \leq 2\pi R^2$, being R the target radius. The way the system reaches this bound is through saturation. Gluons are no longer independent from each other and recombination effects start to set in. This phenomenon prevents

[9] DESY (Deutsches Elektronen-Synchrotron) is a German national research center and HERA (Hadron-Elektron-Ringanlage) was an accelerator which collided electron and positrons with protons.

[10] BNL (Brookhaven National Laboratory) is a national laboratory that belongs to the U.S. Department of Energy and RHIC (Relativistic Heavy Ion Collider) is a collider of protons and heavy ions.

[11] The Tevatron, located at Fermilab in U.S., collided protons and anti-protons with a center-of-mass energy of 1.96 TeV.

[12] CERN (Conseil Européen pour la Recherche Nucléaire) is an European organization for nuclear research and LHC (Large Hadron Collider) is an accelerator that collides protons and heavy ions and is the most energetic in the world so far.

the unlimited growth of the total cross section, what would violate the fundamental principle of unitarity. As the gluons are self-interacting, linear QCD equations, such as DGLAP (Dokshitzer-Gribov-Lipatov-Altarelli-Parisi) [5–7] and BFKL (Balitsky-Fadin-Kuraev-Lipatov) [8,9], can describe the high-gluon contribution at small-x via the splitting of high-x gluons into smaller-x gluons. To achieve the saturation required to limit the growth of the cross section, small-x gluons start to recombine into higher-x gluons. This process is described by non-linear QCD equations, such as BK (Balitsky-Kovchegov) [10,11] and JIMWLK (Jalilian-Marian-Iancu-McLerran-Weigert-Leonidov-Kovner) [12, 13]. The scale at which this phenomenon sets in is called saturation scale, Q_s^2, typically a few GeV^2 for $x < 10^{-4}$. Consequently, the phase-space covered at HERA is at the interface between the saturation and the non-perturbative domains of QCD and does not lead to a clear conclusion about the former [14].

The origin of the saturation regime, successfully described by the "Colour Glass Condensate" (CGC) [15–20] effective field theory, states that it should also occur in nuclei [13]. Strong gluon fields resulting from the large number of nucleons in a heavy nuclei lead to gluon saturation. Within this regime, the gluon density can become so large that the dense object can behave like a coherent one, as a glass. This is why such object is termed a color glass condensate. Using a classical image, it is not possible to fill in protons with as many gluons as one would like to, since the available space is limited. This new regime of QCD, dominated by high gluon density and where usual equations are no longer valid, has not been clearly observed yet. An electron ion collider would enable the clarification of this new domain. It is easily understandable that, in order to see these new phenomena, one needs heavy objects where the number of gluons is large. Additionally, as the nucleus is a more dense object, saturation should happen at a higher scale than at HERA, which means that it is contained in the domain of perturbative QCD. Most of the existing experiments on nuclear DIS probe the high-x range of the nuclei structure, far away from the saturation regime. On the other hand, it is hoped that experiments at a new electron-ion collider will be able to study this regime, as such machine allows the measurement of inclusive and exclusive observables that are affected by the enhancement of non-linear effects in terms of the nuclear mass number [2, 21]. Increasing the nuclear mass number allows amplifying saturation effects through the nuclear saturation scale, $Q_{s,A}^2$. Particularly, within the parton saturation framework the nuclear saturation scale, $Q_{s,A}$, is enhanced with respect to the nucleon one by a factor A^{Δ} , with $\Delta \approx 4/9$. For

instance, for lead targets this increases the nuclear saturation momentum, $Q_{s,A}$, by a factor 3 in contrast to the proton one, where $Q_{s,p}(x = 10^{-5}) \simeq 1\ GeV$ [22].

HERA set electron-proton processes as a fundamental part of modern high energy particle physics. It evidenced the richness of DIS physics and the feasibility of building and operating high energies at ep colliders. Amid striking learning and progress accomplished with HERA, the reasons for constructing future ep and eA colliders are several, including the need of [3]

- Higher energies, what is motivated by three things: 1) to make charged currents a real, accurate part of ep physics, and this is important in order to completely unfold the flavor composition of the sea and valence quarks, for example. 2) to produce particles with greater masses (Higgs, top, exotics, etc) 3) to study the gluon saturation region for which one needs to perform measurements at smaller-x, i.e., higher energies that had been available at HERA;
- Much higher luminosity: since HERA provided just a hundred pb^{-1}, it could not accurately achieve the high-x region. In addition, the machine was limited regarding the statistics in solving puzzling event fluctuations;
- Dealing with the complexity involved in the interaction region when a bent electron beam caused synchrotron radiation while the opposite proton beam generated great halo background through beam-gas and beam-wall proton-ion interactions;
- Using nuclei as targets: as discussed previously, increasing the atomic mass number of the targets enhances the saturation scale, and this is necessary to study the non-linear regime of QCD, one of the main goals of an electron - ion collider.

Here is how this work is organized. In the next chapter, we introduce the main concepts of DIS in electron-proton processes and expose the modifications that take place when we consider a nucleus as the target instead of a proton. The phenomenon of nuclear shadowing is examined alongside other phenomena such as anti-shadowing, EMC effect and the Fermi motion region. Chapter II mostly aims to present and contextualize the reader towards an historical and theoretical analysis concerning nuclear DIS from which the physics of electron-ion collisions is based on.

Chapter III concerns to the theoretical framework of small-x QCD. In particular, we introduce the k_T-factorization formalism and the QCD color dipole picture. In addition, the phenomenon of parton saturation is also discussed.

Following to Chapter IV, we discuss about the upcoming and possible future electron-ion machines, such as the Electron-Ion Collider (EIC), the Large Hadron electron Collider (LHeC) and the Future Circular Collider (FCC). The design projects associated to these facilities are briefly exposed and we also point out the main gains that these colliders are able to bring to the particle physics community.

Chapter V addresses the studied processes involving electron-ion collisions. We have investigated the diffractive gluon jet production, timelike Compton scattering and exclusive Z^0 production. Adopting the dipole picture, the first delivers the possibility of extracting the saturation scale from the experiments, which would be timely at electron-ion collision experiments. For the timelike Compton scattering, we apply the k_T-factorization approach for the first time in such process with nuclear targets, and this could be useful for several reasons that we outline in that chapter. Regarding the exclusive Z^0 production, we also look into this process within the k_T-factorization framework and discuss on the advantages of studying it in the context of electron - ion collisions.

Finally, in the last chapter we expose the main conclusions extracted from the studied processes. We perform a thorough analysis on the applicability of the referred processes for the future electron-ion facilities.

2 Hadronic and nuclear structures

In general, lepton beams (like electrons and muons, for example) are the best microscope of partons because they act as a probe of the target‘s structure. Electrons and positrons couple directly to the quarks. By applying high energies to the collision, one can deeply investigate quarks and gluons with small momentum fraction x, studying their behavior over a wide range of Q^2 (the so called photon virtuality).

Deep Inelastic Scatteing is the standard process to probe the hadronic structure and is one of the simplest scattering process that occur at short distances. In this process, the electron emits a virtual photon that interacts with the target (a nucleon or a nucleus). Throughout the subsections below, we start discussing DIS in proton targets and then introduce the main aspects concerning DIS in nuclei targets, exposing the modifications that take place when the electron interacts with a nucleus instead of a proton.

2.1 Deep inelastic electron-proton scattering

In the case of DIS in electron-proton processes, the electron emitts a virtual photon with virtuality Q^2 (where the virtuality is equal to minus the four momentum squared of the photon, i.e., $Q^2 = -q^2$) which then interacts with the proton. As a result, the hadron breaks up and allows one to investigate its partonic content. The quantity Q^2 sets the hard scale of the problem, and the reaction is the following [23]:

$$e + P \rightarrow e' + X \ , \tag{2.1}$$

where e and e' represent the incoming and outgoing electrons, respectively. The variable P denotes the proton target and X stands for a set of unknown produced particles since this is an inclusive process. The scattering diagram can be seen in Fig. 2.1. Usually, the following Lorentz invariants are defined to describe DIS:

$$Q^2 = -q^2 \ , \qquad y = \frac{P.q}{P.p} \ , \qquad x_B = \frac{Q^2}{2P.q} \ . \tag{2.2}$$

In the expressions above, x_B is the so-called Bjorken variable and y is the inelasticy, also written as $y = (E - E')/E$, where E (E') is the energy of the incoming (outgoing) electron. Combining the previous three equations, the following relation is obtained:

$$Q^2 = 4EE' sen(\theta/2) \ , \tag{2.3}$$

where θ is the angle between the momenta of e and e', that is, $\vec{p}$ and $\vec{p'}$. Alongside the definitions above, there are also the following quantities that are important in the context of DIS:

$$s = (P+p)^2 \ , \qquad s^* = (P+q)^2 = m_p^2 - Q^2 + 2P.q \ , \qquad \nu = \frac{p.q}{m_p} = E - E' \ . \tag{2.4}$$

In the previous relations, s is the center-of-mass energy squared of the electron-proton system, s^* is the center-of-mass energy squared of the photon-proton system and ν is the energy difference between the incoming and scattered electrons in laboratory system. Eqs. (2.2) and (2.4) can be gathered together to get what follows:

$$x = \frac{Q^2}{Q^2 + s^* - m_p^2} = \frac{Q^2}{2m_p\nu} \ , \tag{2.5}$$

$$Q^2 = xy(s - m_p^2 - m_e^2) \approx xys \ , \tag{2.6}$$

where it was considered that $s^2 >> m_p^2 >> m_e^2$, being these inequalities valid in the high energy regime. Taking the scattering amplitude concerning the diagram in Fig. 2.1, after several steps one obtains the DIS inclusive cross section (see Ref. [24] for a detailed analysis):

$$\sigma^{ep} = \int \frac{d^3\vec{p'}}{(2\pi)^2 EE'} \frac{1}{16} \sum_X \sum_{\epsilon,s,s'} |M_{\epsilon,s,s'}(X)|^2 (2\pi)^4 \delta^4(P + q - p_X) \ . \tag{2.7}$$

In Eq. (2.7), s and s' stand for the spin of the incoming and scattered electrons, respectively, while ϵ is the spin of the proton target. P is the proton momentum and p_X is the net momenta of all produced particles. It is convenient to express the differential cross section in terms of x and Q^2, parameterizing it in terms of adimensional structure functions in the form [25]

$$\frac{d^2\sigma}{dxdQ^2} = \frac{4\pi\alpha_{em}^2}{xQ^4} \left[\left(1 - y + \frac{y^2}{2}\right) F_2(x,Q^2) - \frac{y^2}{2} F_L(x,Q^2) \mp \left(y - \frac{y^2}{2}\right) F_3(x,Q^2) \right] \ . \tag{2.8}$$

Above, α_{em} is the QED coupling (taken as $1/137$ for most processes). F_2 is named inclusive structure function of the proton, F_L is its longitudinal part and F_3 is related to parity

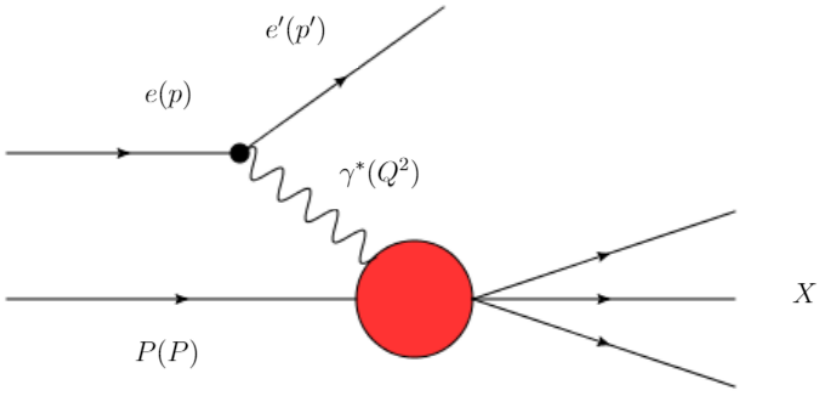

Figure 2.1 – Deep Inelastic electron-proton Scattering.

violating effects depending on what particle projectile is chosen (for values of Q^2 lower than Z^0 mass, F_3 is often neglected). The longitudinal structure function, $F_L(x, Q^2)$, is related to F_2 by $F_2 = F_T + F_L$ (F_T is the transverse structure function of the proton) and is mainly driven by the gluon content of the target.

Structure functions are a measure of the partonic structure of hadrons, and this is relevant for any process that involves colliding hadrons. They are key ingredients for deriving PDFs, which in turn are the non-perturbative inputs of the collinear factorization approach[1]. It is worth carrying out a short discussion on PDFs since these functions will be mentioned several times throughout the text.

In summary, the PDFs give the probability to find partons (quarks and gluons) in a hadron in terms of the proton's momentum fraction, x, carried by the parton and of the momentum scale under which this proton is subject.

In the seminal work of Ref. [26] it is computed the cross section $d\sigma$ that involves short distances. As an example, one may take into consideration the following process: hadron A + hadron $B \to$ jet $+X$, where the jet has a large transverse momentum P_T. Intuitively, the observed jet initiates as a single quark or gluon coming out from a parton-parton scattering event with high P_T, as seen in Fig. 2.2. With that, the large P_T parton fragments into the observed jet of hadrons.

In Fig. 2.2, a parton a is originated from a hadron A and carries a fraction x_A of the hadron A's transverse momentum. One then writes the probability to find this parton

[1] In the collinear factorization approach, the interactions between partons are considered as occurring collinearly, that is, without any transverse momenta contribution. This will be discussed in detail along the next chapters.

as $f_{a/A}(x_A)dx_A$. Similarly, a parton b that comes from a hadron B takes a fraction x_B of the hadron B's transverse momentum. The probability to find the parton b is therefore $f_{b/B}(x_B)dx_B$. The functions $f_{a/A}(x_A)$ and $f_{b/B}(x_B)$ are called PDFs, acronym for Parton Distribution Functions. By utilizing the intuitive picture described above, one may write the cross section for jet production as follows:

$$\frac{d\sigma}{dP_T} \sim \sum_{a,b} \int dx_A \; f_{a/A}(x_A, \mu) \int dx_B \; f_{b/B}(x_B, \mu) \frac{d\hat{\sigma}}{dP_T} \; , \tag{2.9}$$

where $d\hat{\sigma}$ is the cross section for the partons to produce the observed jet. In other words, this is the parton level cross section and is calculated with perturbative QCD. Its expression is a expansion in powers of α_S:

$$\frac{d\sigma}{dP_T} \sim \sum_{N} \left(\frac{\alpha_S(\mu)}{\pi} \right) H_N(x_A, x_B, P_T; a, b, \mu) \; . \tag{2.10}$$

In the above expression, H_N is obtained from perturbative QCD. For a careful analysis and further details on Eqs. (2.9) and (2.10), the reader may refer to Ref. [26].

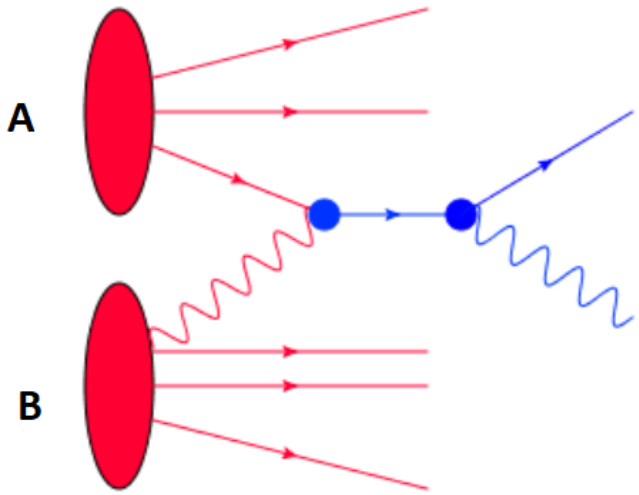

Figure 2.2 – hadron A + hadron $B \rightarrow$ 2 partons.

2.1.1 Parton model

The structure functions F_2 and F_1 were firstly measured in 60's at SLAC[2] and afterwards at DESY using electron beams in 90's. The subsequent years were followed by an extensive set of measurements utilizing electrons and muons. Fig. 2.3 displays the structure function of deuteron, $F_2^d(x, Q^2)$, which is equivalent to the structure function of deuterium, $F_2^D(x, Q^2)$. As one can see, in first approximation F_2^d does not depend on Q^2. If the ratio Q^2/ν is kept constant for higher values of Q^2 and ν, F_2 depends practically only on x, leading to the so-called Bjorken scaling. At the time these measurements were performed, such scaling behavior was viewed with surprise by physicists since it contrasts with the properties of elastic form factors that quickly vanish for higher values of Q^2, instead. [27]

Scaling phenomenon evidences the fact that the virtual photon is absorbed by objects in the nucleon. Historically, these objects were first called partons by R. Feynman [28] and later referred as quarks.

In the Infinitum Momentum Frame - IMF (where the Parton Model was conceived [28]), also known as Breit frame, the nucleon has very large momentum and the momentum fraction carried by the partons relative to the nucleon is written as $x = Q^2/2M\nu$. Within the IMF, the virtual photon has no energy and the partons reverse their longitudinal momentum in the collision process. In this framework, the proton structure functions, F_1 and F_2, may be expressed as

$$F_1 = \frac{1}{2} \sum_i e_f^2 q_f(x) \ , \tag{2.11}$$

$$F_2 = x \sum_i e_f^2 q_f(x) \ , \tag{2.12}$$

in which the index f stands for the quark flavor, e_f is the quark charge and $q_f(x)$ is its distribution function. As seen, in the Parton model $q(x)$ depends only on x. With the expressions above, one can write the well known Callan-Gross relation [30]:

$$F_2(x) = 2xF_1(x) \ , \tag{2.13}$$

what connects the structure functions F_2 and F_1 in the context of the Bjorken scaling.

[2] SLAC - Stanford Linear Accelerator Center is operated by the Stanford University and belongs to the U.S. Department of Energy (DoE). This linear accelerator was built in 1966 and shut down in the 2000s. The energy of the electron beams could reach 50 GeV.

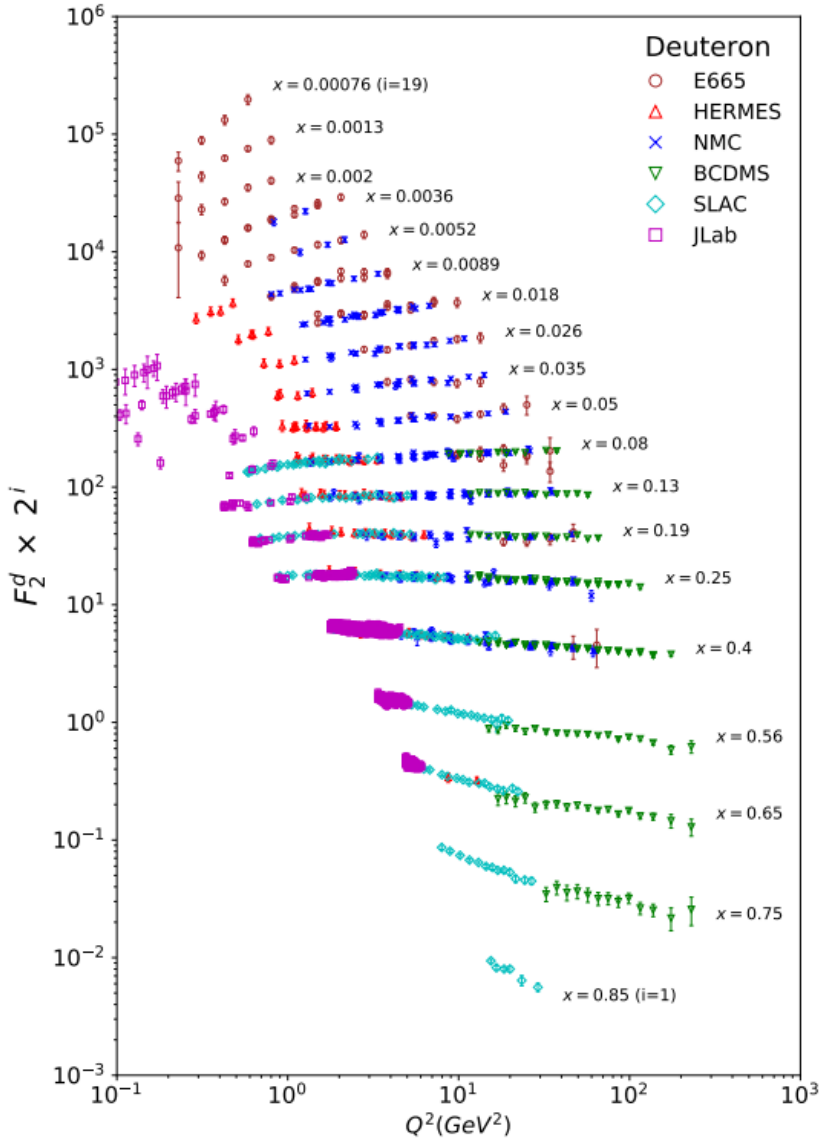

Figure 2.3 – The structure function of deuteron (multiplied by the scale factor 2^i). Taken from the 2018 Particle Data Group (PDG) [29].

2.1.2 The breaking of Bjorken scaling

If one looks at Fig. 2.3, it is clear that F_2 does not depend only on x, but rather on both x and Q^2. For $x < 0.2$, it rises as a function of Q^2, whereas for $x \geq 0.2$ it decreases.

According to QCD, partons have color charge and thus interact between themselves through gluon exchanges. In addition, these gluons inside the proton can auto interact and also split into quark-antiquark pairs named as sea quarks. This implies that in QCD protons are not composed solely by non interacting partons. The valence quarks can radiate gluons which in turn might fluctuate into quark pairs. In that sense, the picture is way more complex compared to that one from the naive Parton Model.

Analogously to QED where α_{em} is defined as the electromagnetic coupling, in QCD one has the strong coupling, being in leading order computed as

$$\alpha_s(Q^2) = \frac{12\pi}{(33 - 2N_f)(\ln\, Q^2/\Lambda^2)} \ , \tag{2.14}$$

where Λ is the QCD mass scale parameter and N_f is the number of quark flavors. Regarding Λ, it is found to be roughly ≈ 200 MeV and sets the Q^2 value from which the nucleon can be simply treated as composed of valence quarks, that is, with no QCD radiation effects. As noticed in Eq. (2.14), when $Q \to \infty$ the variable α_s tends to zero. This phenomenon in QCD is called asymptotic freedom, where the partons behave as quasi-free objects. In the Breit frame where the Parton Model is considered, such behavior is justified.

For large enough Q^2, α_s is less than one and then QCD can be treated perturbatively. The kinematic domain in which it can be handled via perturbation theory is called hard region. For smaller values of Q^2 implying that α_s is greater than one, one has the soft region where perturbative calculations are no longer applicable. Within this domain, non perturbartive approaches have to be apllied, such as the Lattice QCD and Regge theory, for instance (for further analysis on the strong coupling and the kinematic domains of QCD, we quote the seminal work carried out in Ref. [31]).

As mentioned, the plot of F_2^d in Fig. 2.3 attested that this function depends both on x and Q^2. In perturbative QCD, there is a set of coupled equations, the DGLAP equations [5–7], that describe the evolution of PDFs in terms of Q^2 variation. The expressions are the following:

$$Q^2 \frac{\partial \Delta^{f\overline{f}}(x,Q^2)}{\partial Q^2} = \frac{\alpha_s}{2\pi}\int_x^1 \frac{dz}{z} P_{qq}(z)\Delta^{f\ \overline{f}}\left(\frac{x}{z}, Q^2\right) \ , \tag{2.15}$$

$$Q^2 \frac{\partial}{\partial Q^2}\begin{pmatrix}\Sigma(x,Q^2)\\ G(x,Q^2)\end{pmatrix} = \frac{\alpha_s}{2\pi}\int_x^1 \frac{dz}{z}\begin{pmatrix}P_{qq}(z) & P_{qG}(z)\\ P_{Gq}(z) & P_{GG}(z)\end{pmatrix}\begin{pmatrix}\Sigma(x/z,Q^2)\\ G(x/z,Q^2)\end{pmatrix} \ , \tag{2.16}$$

where

$$\Sigma(x,Q^2) = \sum_f [q^f(x,Q^2) + q^{\bar{f}}(x,Q^2)] \ , \tag{2.17}$$

$$\Delta^{f\overline{f}}(x,Q^2) = q^f(x,Q^2) - q^{\overline{f}}(x,Q^2) \ . \tag{2.18}$$

In Eqs. (2.15) and (2.16), $z = (x/x')$, $\Sigma(x,Q^2)$ and $\Delta^{f\bar{f}}(x,Q^2)$ are related to the quarks and anti-quarks distribution functions (as defined in the two previous expressions), $G(x,Q^2)$ is

the gluon distribution and P_{ij} are called Splitting Functions. The latter quantities measure the probability of finding a parton i with momentum fraction x radiated from the parton j with momentum fraction x'. The set of equations above are valid for the domain of large Q^2. In this region, one shall make use of the collinear factorization (a review on QCD collinear factorization may be encountered in Ref. [32]) for which the partons momenta have only longitudinal components. This approximation holds for high values of Q^2, i.e., the hard region, but can not be applicable when it comes to not very hard processes. As Q^2 decreases, one enters the semi-hard region in which the collinear factorization is no longer valid and hence other approaches must be applicable, such as the dipole formalism and the k_T-factorization framework. In Section IV, we will perform a careful discussion on these two approaches.

2.2 Nuclear DIS

The modifications on DIS when one considers nuclei as targets rather than nucleons can be measured through the comparison among the inclusive structure function of a bounded nucleon and that of deuterium, F_2^D, since the latter is assumed as the best approximation of a free nucleon. The reason for comparing the bounded nucleon with deuterium instead of protons is the fact that, especially at large x, protons and neutrons have different structure functions, thus it is more reasonable to use deuterium and not the proton to account for a free nucleon. In summary, the nuclear effects in DIS are translated by the difference between the deuterium structure function and that of a bounded nucleon inside the nucleus. If the latter was merely a collective amount of no interacting nucleons, there would be no difference among these quantities. Instead, it is found that the ratio $2\ F_2^A/A\ F_2^D$ (where A is the nuclear mass number and F_2^A (F_2^D) is the nuclear (deuterium) structure function, respectively) is not the unity, what is a clear signal that there must be some interaction between nucleons [33].

Generally, the nucleus was assumed as composed of feebly bounded nucleons that are confined through a potential due to their mutual interaction. It was a striking result when the EMC experiment revealed that the iron nuclear structure function, F_2^{Fe}, had a systematic nuclear dependence with respect to that of deuterium as the effect reached 20 % for $x \sim 0.5$ [34]. Interestingly, this is notably larger than the effect (less than 5 %)

caused to the natural scale for nuclear effects set by the ratio between the binding energy per nucleon and the nucleon mass.

Afterwards, a large number of fixed-target experiments corroborated the nuclear dependence that had been evidenced earlier, although with significant modifications compared with those results of EMC effect in the small-x regime [35–37]. In Fig. 2.4 it is displayed the experimental data of the ratio between the nuclear structure function (per nucleon) of some nuclei and the nuclear structure function (per nucleon) of deuterium (in terms of x), often named in literature as nuclear modification factor. In addition, it is also shown a schematic curve of this quantity [33] based on these measurements. We can summarize the behavior of this factor into four different regions [38]:

- Shadowing region: $R^A < 1$ for $x \lesssim 0.1$;
- Antishadowing region: $R^A > 1$ for $0.1 \lesssim x \lesssim 0.25$;
- EMC region: $R^A < 1$ for $0.25 \lesssim x \lesssim 0.8$;
- Fermi motion region: $R^A > 1$ for $x \gtrsim 0.8$.

After giving an overview of the nuclear effects that arise in nuclear DIS, below we will discuss separately the four regions cited above, performing a careful analysis on the shadowing region. The reason for aiming such region is that it is contained in the domain of small-x (high energies), being this kinematic regime the main focus of the present work.

1. **The shadowing region**

Strictly speaking, the definition of nuclear shadowing is that the ratio $2F_2^A/AF_2^D$ is less than one for the domain referred above. The shadowing effect is stronger for heavier nuclei and lower x. For not very small x, it is found that the phenomenon weakens slowly as Q^2 increases. At a fixed energy, since Q^2 is related to x as $Q^2 \approx x\sqrt{s}$, for very small x one gets $Q^2 \leq 1$ GeV^2, being this region not contained in the perturbative domain of QCD. The NMC (New Muon Collaboration) [36] and the E665 [37] experiments attested that data with good quality are only found for $x > 0.004$, which is a big limitation for studying shadowing effect in the very small-x regime. If x is kept fixed at low values and Q^2 is enhanced, the shadowing of F_2^A occurs due to shadowing of quark and antiquark distributions [33] (see also Refs. [42, 43]).

The usual understanding of nuclear shadowing is related to multiple scattering [44–55]. Most approaches explain the depletion in the shadowing region by means of the

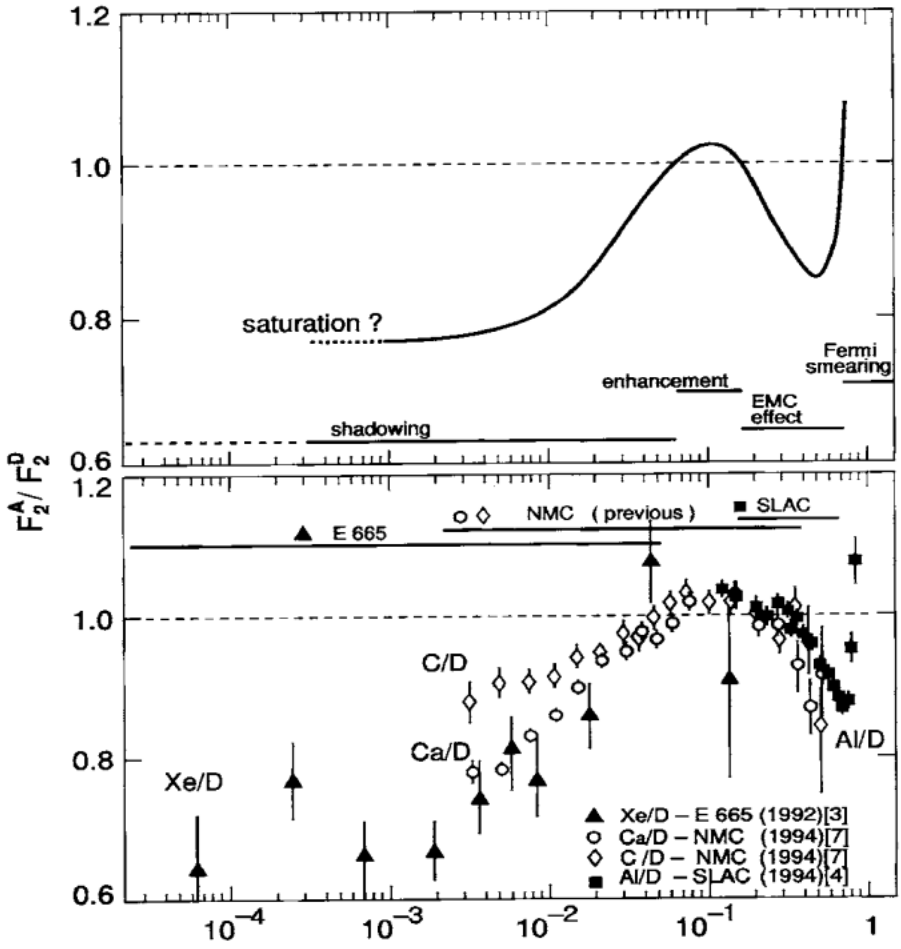

Figure 2.4 – Upper: schematic curve of the nuclear ratio between the nuclear structure function (per nucleon) and the deuterium structure function. Lower: data of the nuclear ratio for different nuclei (Xe, Ca, C and Al) from experiments FNAL-E665 [39], NMC-NA37 [40] and SLAC [41].

hadronic behavior of the virtual photon. At high collision energies and at moderate/low Q^2, the hadronic component of the virtual photon will interact several times with the nucleons contained in the nucleus, giving rise to multiple scattering phenomena. Consequently, this fact yields the decrease of the corresponding cross sections, which will be analyzed in detail shortly [38].

Investigating the nuclear shadowing effect has great importance in the study of QCD at high energies. Beside delivering an experimental testing ground of QCD theory at high energies, it also permits to control the amount of multiple scattering by changing the nuclear size for given values of x and Q^2, since any quantum field theory considers multiple scattering as a consequence of the fundamental principle of unitarity. Furthermore, as the scale Q^2 and x may be varied, the interplay between hard and soft regions of QCD can

be looked into. Through nuclear collisions, the RHIC and the LHC have been studying the content of the nuclear environment by investigating the nuclear parton distributions in the small-x regime [38]. The upcoming EIC will be able to boost the investigation of the nuclear content of the nuclei by constraining the nuclear PDFs, which in turn will be achieved by colliding electron beams with the nucleus. In that sense, the EIC will strongly leverage the study of the nucleus and the overall investigation of the fundamental structure of matter.

Following the Glauber-Gribov theory that takes into account the multiple scattering of the hadronic component of the virtual photon with a nucleus composed of nucleons and neglects their mutual interaction, understanding how multiple scattering leads to shadowing can be done through a simple example. Considering a massless scalar particle scattering on a nucleus whose mass is A, this example consists in calculating the contributions from one and two scatterings in order to compare them. Adopting the light-cone coordinates (see Appendix A) and taking the optical theorem, the imaginary forward amplitudes of the projectile-nucleon and projectile-nucleus contributions read as

$$i\ m(q^2 = t = 0) = -\sigma\ , \qquad i\ M_n(q^2 = t = 0) = -\sigma_A^n\ , \tag{2.19}$$

where σ and σ_A^n are the total cross sections of the projectile-nucleon and projectile-nucleus collisions, respectively. The quantity n accounts for the n-scattering contribution. For one scattering, the amplitude is computed as (see Ref. [38] for a detailed analysis on the calculation procedure, as well as Figure 4 therein that contains the Feynman diagrams of 1-scattering and 2-scattering contributions)

$$\begin{aligned}(2\pi)2p_+\delta(p'_+ - p_+)i\ M_1(t) &= (2\pi)2p_+\delta(p'_+ - p_+)i\ m(t=0)A(p_+ + p'_+)\int d^4x \rho_A(x_+, x_T)e^{ix.(p'-p)} \\ &= (2\pi)2p_+\delta(p'_+ - p_+)i\ m(t=0)A\int d^2x_T\ T_A(x_T)e^{-x_T.(p'_T - p_T)}\ .\end{aligned} \tag{2.20}$$

Above, x_T is the impact parameter, that is, $|x_T| = b$, and ρ_A is the nuclear density (normalized to 1). The nuclear profile function, $T_A(b)$, is simply given by

$$T_A(b) = \int_{-\infty}^{+\infty} dx_+ \rho_A(x_+, x_T)\ . \tag{2.21}$$

If $t = 0$, one obtains from Eq. (2.20) that

$$\sigma_A^1 = A\sigma\ . \tag{2.22}$$

With regards to the 2-scattering contribution, it is calculated as

$$(2\pi)2p_+\delta(p'_+ - p_+)i\ M_2(t) = iA(A-1)[i\ m(t=0)]^2 \int \frac{d^4k}{(2\pi)^4} d^4x_1 d^4x_2 e^{x_1.(k-p)} e^{x_2.(p'-k')}$$

$$\times \frac{(p_+ + k_+)(p'_+ + k_+)}{k^2 + i\epsilon} \rho_A(x_{1+}, x_{1T})\rho_A(x_{2+}, x_{2T}) \ . \tag{2.23}$$

To evaluate the integral above, it should be computed over k_- in the complex plane by closing an integration contour with an infinite semicircle in the lower half-plane. The result is given by

$$i\ M_2(t) = A(A-1)[i\ M(t=0)]^2 \int \frac{d^2k_T}{(2\pi)^2} dx_{1+} dx_{2+} d^2x_{1T} d^2x_{2T} e^{-ik_T^2(x_{2+}-x_{1+})/2p_+}$$

$$\times e^{-i[x_{1T}.(k_T - p_T) + x_{2T}.(p'_T - k_T)]} \rho_A(x_{1+}, x_{1T})\rho_A(x_{2+}, x_{2T})\ \Theta(x_{2+} - x_{1+}) \ , \tag{2.24}$$

where $\Theta(x_{2+} - x_{1+})$ is the Heaviside function. Since the coherent length is defined as $l_c = 2p_+/k_T^2$, coherence effects are embedded in the factor $e^{-ik_T^2(x_{2+}-x_{1+})/2p_+}$. After performing the integration in the previous equation, the variable p_+ will appear multiplying the remaining of the integral result. Thereby, as for low energies p_+ tends to zero, the amplitude $i\ M_2$ also vanishes, that is, $iM_2 \to 0$ when $p_+ \to 0$. Consequently, all the rescattering contributions vanish and the cross section has to be calculated from the superposition of single scatterings, yielding the incoherent limit where there is no shadowing effect and the nuclear modification factor is one. On the contrary, at high energies $p_+ \to \infty$ and thus the exponential factor tends to one, leading to the following expression:

$$iM_2(t) = \frac{A(A-1)}{2} \big[im(t=0)\big]^2 \int d^2x_T e^{-ix_T.(p'_T - p_T)T_A^2(b)} \ . \tag{2.25}$$

For forward scatterings, $p'_T = p_T$. Using Eqs. (2.23) and (2.24),

$$\sigma_A^2 = \frac{-A(A-1)}{2} d^2x_T \big[T_A(b)\big]^2 \sigma^2 \ . \tag{2.26}$$

Noticeably, the cross section above (corresponding to the correction of 2-scattering) is a negative quantity. Thus, successive summation of n-scattering contributions will lower the total cross section and, therefore, it will be a smaller value than that from the summation of independent collisions among projectile and nucleons. By Eq. (2.26), it is clear that for higher cross sections, which means higher energies and lower x, the negative corrections increase and lead to an enhancement of nuclear shadowing. Likewise, as A increases shadowing effect gets stronger.

Shadowing has different understandings according to the frame where the scattering is considered. Consider the case of low energy collisions, e.g., around 2 GeV. Such value implies a γp cross section of about 0.1 mb, which corresponds to a mean free-path of spill over 100 fm in nuclear matter. At high energies where the dipole picture is applicable, as the photon fluctuates into a quark-antiquark pair one could ascribe a cross section of $\sim$ 20 mb, commonly a cross section of strong interactions. For such process, the mean free-path would be about 3.5 fm, considering that the coherence length of the virtual photon fluctuation is $l_{coh} \sim 1/2m_N x$, where m_N is the nucleon mass. If the fluctuation takes place over a larger value of the inter-nucleon distance ($\sim$ 2 fm), the absorption of the photon shadows it. In other words, this absorption avoids the photon from reaching the remaining nucleons [33].

In the Breit frame, shadowing can be viewed as a consequence of saturation phenomena, characterized by a high gluon density in the transverse plane of the target. Saturation was quickly discussed in the Introduction. In the next section we will analyze it in detail and explain its origin.

2. **Anti-shadowing region**

Similarly to the case of shadowing, anti-shadowing effect can be understood by means of Glauber multiple scattering phenomena. Consider the case of two nucleons, as seen in Fig. 2.5. The first contribution for the amplitude comes from standard DIS (left diagram), where only the nucleon 2 interacts with the dipole. On the other hand, in the second contribution (right diagram) there are two amplitudes that must be taken into account. Beside the inelastic scattering of the nucleon 2 with the dipole, there is also a leading-twist Diffractive Deep Inelastic Scattering (DDIS) corresponding to an exchange of two gluons between the nucleon 1 and the quark-antiquark pair. Due to the fact that the second contribution involves two processes, their interference can lead to shadowing or anti-shadowing, depending on the phase of the DDIS amplitude [56].

Within the Regge theory (for a thorough review on Regge theory, we quote Ref. [57]), diffraction takes place via the exchange of Reggeons and Pomerons. In the context of QCD, the Reggeons are associated to quark-antiquark color singlet exchanges, while the Pomeron is analogous to the exchange of two gluons. In few words, shadowing and anti-shadowing are determined through the difference betweeen the phase structure of the exchanged Reggeons and Pomeron. The 0, 1 Reggeons contributions have $\alpha_R = 1/2$ and phase

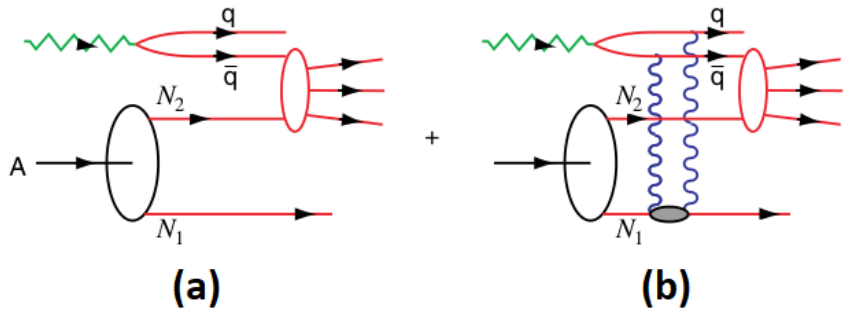

Figure 2.5 – Sum of interfering one-step and two-step amplitudes in DIS on a nucleus A. The scattering on the nucleon N_1 in the two-step amplitude is diffractive DIS, leaving N_1 intact. Then, the system q interacts inelastically with N_2. There is interference between one-step and two-step amplitudes. The nucleon N_2 sees two fluxes coming from the virtual photon and the $q\bar{q}$ system from DDIS on nucleus N_1. In summary, what happens is that N_1 "shadows" N_2. Extracted from [56].

$1/\sqrt{2}(-i+1)$, whereas the Pomeron has positive imaginary part in the phase. As a result, the relative phase may be either constructive or destructive. If DDIS amplitude is due to Reggeons exchange, it will be constructive and will imply in anti-shadowing. On the contrary, if it is due to Pomeron exchange, there will be destructive interference, leading to shadowing. Constructive interference is verified for $0.1 < x < 0.2$. In the context of Regge theory, it is well known that Reggeons dominate at low energies (large-x), whereas the Pomeron is the dominant object at high energies (small-x). Hence, these results fit the verified domains of shadowing and anti-shadowing effects. Lastly, an important remark about anti-shadowing is that, since Reggeons are translated in QCD by quark-antiquark exchanges, this effect is flavor dependent and, thereby, each quark-antiquark pair will have different pattern of interference and then the interval of anti-shadowing effect will vary according to the quark flavors.

3. **The EMC region**

A possible interpretation of the EMC effect is that interactions among nucleons at a wide-interval distances are mediated by meson exchanges. Traditionally, it is predicted a net enhancement of virtual pion distributions as the nuclear density increases comparing with the free nucleon [58, 59]. The reason is that meson interactions are attractive in nuclei, with the pions carrying about 0.2-0.3 of the light-cone momentum fraction of the nucleon. Within these models, the referred pions may carry 5 % of the total momentum

to suit the EMC effect at $x \sim 0.3$. The predicted growth of sea quarks from 10 % to 15 % for $x \sim 0.1 - 0.2$ and $A \geq 40$ can be understood as the result of sea anti-quarks from these pions scattering in the hard probe. However, the usual approach of nuclear binding, i.e., that of pions being exchanging is put in doubt due to the fact that pA collisions at Fermilab demonstrated that anti-quark distribution from Drell-Yan production pairs remain constant in terms of A [60]. Moreover, results from the experiment E91-003 at Jefferson Lab showed no relevant pion excess in eA(AB) reaction [61]. Therefore, the facts raised above indicated that EMC effect is not significantly contributed by pions [33].

As the idea pointed out in the last paragraph had presented no successful description of the EMC effect, authors showed in Ref. [62] that the chiral quark-soliton model could provide reasonable description of such phenomenon. Additionally, it was showed that this model was able to explain the difference among anti-quark up and down distributions from Drell-Yan pairs. A large number of QCD LO (leading order) analyses for Drell-Yan and nuclear DIS data alongside the application of baryon charge and momentum sum rules delivered additional information concerning nuclear effects within this kinematic regime [63–66]. According to these studies, the valence quark distribution in nuclei is increased at $x \sim 0.1 - 0.2$. Since the momentum fraction of gluons in nuclei is about 1 % (what is nearly the same fraction they carry in a free nucleon), considering that gluon shadowing is similar to quark shadowing, this implies an increase of the gluon distribution for this domain [33].

4. **The Fermi motion region**

The Fermi motion region may be explained by the fact that nucleons are not stationary in the nucleus, but rather move with an average momentum k_F. As discussed in the previous section, in the Parton Model the inclusive structure function, F_2, is proportional to the quark distribution in the nucleon. However, it holds only for free nucleons as an hydrogen target, for instance [27].

For measuring x in nuclear targets, it is assumed that the nucleons are stationary, which in fact is an approximation. Actually, the nuclear structure function must be calculated by the convolution between the nucleon momentum distribution in the nucleus, $f_n(z)$, and the bare nucleon structure function, $F_2^n(x, z)$. Therefore, one can obtain the nuclear structure function as follows:

$$F_2^A(x) = \int_x^A dz f_n(z) F_2^n(x/z) \ . \tag{2.27}$$

In Eq. (2.27), z stands for the momentum fraction carried by the nucleon relative to the nucleus times the nuclear mass number, A.

2.3 The interplay among space and time in QCD

Depending on the Bjorken- x variable, i.e., the target's momentum fraction carried by the partons in DIS, the scenario is distinct. For example, assuming that the transverse separation of the dipole is $r \sim 1/Q$, for $x > 0.2$ its longitudinal length is given by $l_{coh} \sim 1/2m_N x$, and thus the virtual photon gets very close to the nucleons, usually reaching the middle of the nucleus. In addition, if Q^2 is large enough, the produced partonic state has a weak interaction with the medium (this is due to the asymptotic freedom phenomenon discussed earlier). For lower x, l_{coh} outpaces the nuclear size even for the heaviest nuclei and, thereupon, for very small x DIS takes place through two separated stages, namely a QED process and a QCD one. Regarding the former, the photon fluctuates into a Fock state of a quark-antiquark pair (leading contribution). After that, this pair interacts with the target (QCD process) and, due to time dilatation, the interaction among partons keeps frozen over large distances. As a result, the interaction between partons and the nucleus is coherent and instantaneous. In the high energy regime, one can consider the interactions as an eikonal that maintains the transverse size of the dipole unaltered [33].

In the context of perturbative QCD, due to large value of Q^2 the transverse size of the dipole is small and this leads to the phenomenon of color transparency (see Ref. [67]), where the quark and antiquark are so close that they behave as a whole object having no net color. At very high energies and moderate Q^2, the target is characterized by a high gluon density in the transverse plane and the projectile is formed by medium/large dipoles. Consequently, interaction among the projectile and the target may be strong. In literature this phenomenon is often referred as color opacity.

Additionally to the time scale of the virtual photon fluctuating into the quark-antiquark pair and the time of interaction between this dipole and the nucleons, another important time scale is the formation time, commonly denoted by the variable τ_h. By

formation time one understands the necessary time for hadronization after the dipole interaction with the nuclear content. Since, in principle, τ_h is greater than the production time of the color dipole, before hadronizing the object suffers successive scattering, i.e., multiple scattering, implying the phenomenon of radiative energy loss and broadening on the momentum distribution. For quarks, the transverse momentum broadening is given by [68, 69]

$$< p_\perp^2 >= \frac{\pi^2 C_F \alpha_s}{2} \rho L \; xg(x, Q^2) \approx 0.5 \alpha_s \left(\frac{L}{5 \text{ fm}} \right) \text{GeV}^2 \; , \tag{2.28}$$

in which ρ is the nuclear matter density, L is the length of matter traversed and C_F is the Casimir factor for quarks whose value is $C_F = 4/3$. In Ref. [70], Drell-Yan data showed that $< p_\perp^2 > \sim 0.12$ GeV^2 for heavy nuclei, what is in accordance with Eq. (2.28). It also agreed with the predicted low size of this effect. Furthermore, it could be attested a difference between the dependence on A of Drell Yan di-muons and J/ψ and Υ decay and production [71]. Such fact is understood in the sense that the vector mesons also interact strongly, which does not occur for di-muons. Nevertheless, the size of this effect alongside the similar broadening of J/ψ and Υ needs a better explanation. Moreover, when it comes to dijets, the $p_\perp$ disparity in nuclear photo-production indicates considerably higher $p_\perp$ broadening effect compared to J/ψ production [72]. Therefore, $p_\perp$ presents a non-universal behavior, which can be also caused by the contamination of the jet from soft debris. In the case of hadron production in hadron-nucleus collisions, this parton $p_\perp$ broadening may occur due to multiple scattering and can originate the abnormal behavior observed for this process at low energy (few GeV) and moderate $p_\perp$. It turns out that in inclusive hadron production for proton-nucleus collision the production ratio is less than one for small p_T but, interestingly, overpasses one for the interval 1 - 2 GeV, what is known as Cronin effect [73].

Concerning the phenomenon of energy loss in nuclear collisions, it is caused by the scattering itself and due to vacuum energy loss, being the latter the dominant effect [74]. For DIS it is observed a small energy loss effect [75–77]. For photon energies about $10 - 20$ GeV, experimental data shows that leading hadron multiplicity is lowered and decreased by 10 % in the case of Nitrogen-14 targets. At smaller-x, that is, at higher energies, these multiplicities progressively become dependent on the nuclear mass number, A, giving rise to absorption of partons, i.e., shadowing effect [78–81].

Finally, it is important to mention that one should expect that the phenomenon of energy loss in terms of modified fragmentation functions is able to agree with HERMES data [82]. Nonetheless, these data were also successfully described in terms of multiple scattering and absorption effects [83, 84]. As the required formation time should be around 0.5 fm [74, 83, 85], at the EIC it is believed that the formalism of modified fragmentation functions might be more feasible [86].

As the processes and corresponding phenomena studied in this work take place at the small-x regime, in the next chapter we aim to approach the theoretical framework of small-x QCD.

3 Small-x regime

The standard approach to address the study of parton densities and hadron structure functions is the collinear factorization, in which the cross sections are written in terms of nonperturbative quantities (the PDFs) and perturbative functions. The former is obtained through the DGLAP set of equations, what can only provide a qualitative comprehension of the small-x regime (where one observes a significant rise of the gluon density) since its applicability domain is limited by the assumptions assumed in its derivation.

The main supposition that is taken by the DGLAP equations is related to Q^2, whose value is considered large enough to enable neglecting of higher twist corrections. Given this fact, the perturbative ressumation is organized in powers of $\alpha_s^m[\alpha_s \log(Q^2)]^n$, where the diagrams that correspond to all n and fixed m give rise to the so-called LLA (leading logarithm approximation). In the small-x region, since gluons are the dominant partons, only the leading contribution to the gluon density growth should be taken. This process is referred as DLA (double logarithm approximation)[1], where contributions of the form $[\alpha_s \log(Q^2)\log(1/x)]^n$ are summed up.

In the case where Q^2 is not very large, one has to perform the ressumation of all the $(\alpha_s \log(1/x)^n)$ contributions. Such procedure is known as "high energy factorization"or "small-x factorization", where the cross sections and corresponding amplitudes are decomposed into impact factors that are then integrated alongside Green's functions in the transverse space. Specifically, the target impact factor that is integrated along with the Green's function generates the so-called unitegrated gluon distribution function (UGD) or simply unintegrated gluon density, in the transverse space. While in the collinear factorization framework it is considered the scattering process taking place entirely along the longitudinal direction (that is, the partons interact collinearly), as Q^2 decreases the transverse momenta of the gluons ought to be taken into consideration as well, and this is made by nonperturbative functions (UGDs) that explicitly depend on their transverse momenta, often denoted as k_T. In this context, one terms this framework as k_T-factorization. As x and Q^2 are directly proportional (see the discussion in the first paragraph of this chapter), lower Q^2 results in smaller x, implying that the suitable domain for the k_T-factorization

[1] One may also find the term DLLA (double leading logarithm approximation) in literature.

approach is that of small-x and moderate Q^2, commonly referred in literature as semi-hard region.

The evolution of the UGDs is established by the BFKL evolution equation, in which a ressumation of higher twist contributions is executed. This equation predicts a strong rise of the gluon density as x decreases, and such rise is greater than that showed by HERA data. We will discuss in detail along the next sections that this phenomenon is known as saturation regime, where equations like DGLAP and BFKL are no longer valid since saturation is contained in the non-linear regime of QCD [87].

Another approach to describe processes at small-x is known as the color dipole picture, where the virtual photon is decomposed into its hadronic states that then interact with the target. The dipole approach is a very convenient way to study the small-x regime due to its robustness and accuracy to compute DIS observables in the high energy domain. We will discuss shortly that the k_T-factorization and the color dipole approaches are in some way connected. While the former is carried out in the k_T space, the latter takes place in the r space, where r is the dipole transverse separation.

3.1 k_T-factorization approach

This section is based on the review work performed in Ref. [88], where the author exposes the main assumptions and the mathematical procedure involved in the k_T-factorization formalism. Here we will briefly discuss the most relevant points analyzed therein. The reader may find all the details concerning the calculations in the reference cited above.

In the Regge limit (high energies) of QCD, the leading contributions for the amplitude are given from leading logarithms of the form $\alpha_s \log s \sim 1$, where $\alpha_s << 1$. Successively summations of $(\alpha_s \log s)^n$ is a LLA procedure[2].

Consider the following processes: $qq \to qq$, the elastic scattering of two quarks. In the Regge limit, gluons dominate and the imaginary part of the amplitude reads as

$$ImA^R(s,t) = \frac{P^R}{2}\sum_n \int d\Phi_{n+2} A(p_1,p_2;n+2)A^*(p_1',p_2';n+2) \ , \tag{3.1}$$

[2] Here we are closely following Ref. [88], where the author writes log s instead of log$(1/x)$. This can be done since $s \sim 1/x$.

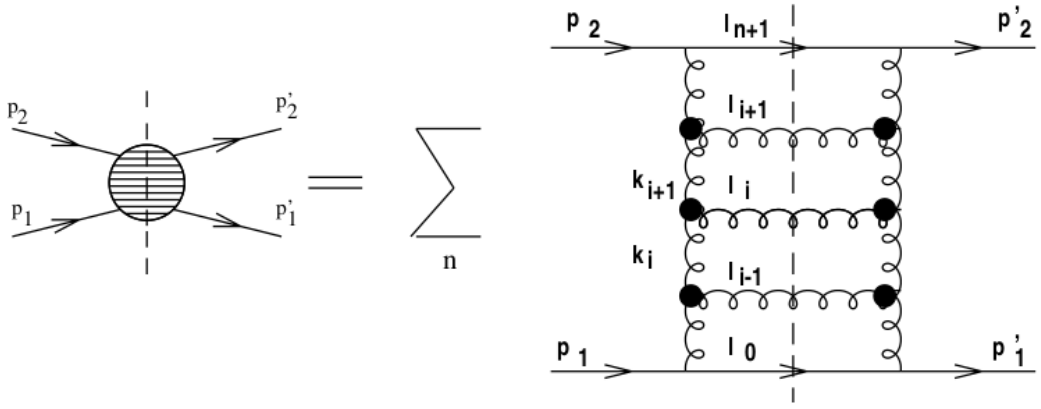

Figure 3.1 – Pomeron exchange. Taken from [88].

where P^R is the color projector, R is the gauge group and Φ stands for the phase space. The referred process is showed in Fig. 3.1. Albeit the amplitude is composed by real and imaginary parts, in the LLA the real part is zero and thus the amplitude is purely imaginary. Fig. 3.1 also presents a ladder diagram of this process in the r.h.s. (right-hand side). The two gluons that are exchanged by the quarks represent the Pomeron, the exchanged object in diffractive processes at high energies in the context of Regge theory. Making use of Sudakov variables (see Appendix B), one shall write

$$l_i = \alpha_i p_1 + \beta_i p_2 + l_{\perp i} \quad . \tag{3.2}$$

Hence,

$$(l_i - l_{\perp i})^2 = \alpha_i^2 p_1^2 + \beta_i^2 p_2^2 + 2 p_1.p_2 \quad . \tag{3.3}$$

Neglecting the quarks masses, $p_1^2 = p_2^2 = 0$. Besides, $s = (p_1 + p_2)^2 = p_1^2 + p_2^2 + 2p_1.p_2 \approx 2p_1.p_2$. In the Regge limit, one has a strong ordering in the α_s's, i.e., $\alpha_i >> \alpha_{i+1}$, implying in a strong ordering in rapidity:

$$y_i >> y_{i+1} \quad . \tag{3.4}$$

The gluons with momenta $l's$ are *reggeized*, and this is a property of the LLA. Gluon *reggeization* means that the standard propagator must be replaced as below:

$$\frac{1}{t_i} \to \frac{1}{t_1}\left(\frac{s_i}{s_o}\right)^{\omega(t_i)} \quad , \tag{3.5}$$

where $t_i = k_i^2 \approx -\vec{k}_{\perp i}^2$ and $s_i = (l_{i-1} - l_i)^2$. The quantity $\omega(t)$ is expressed as

$$\omega(t) = N_c \alpha_s t \int \frac{d^2 k'_\perp}{(2\pi)^2} \frac{1}{k'^2_\perp (k - k')^2_\perp} \quad . \tag{3.6}$$

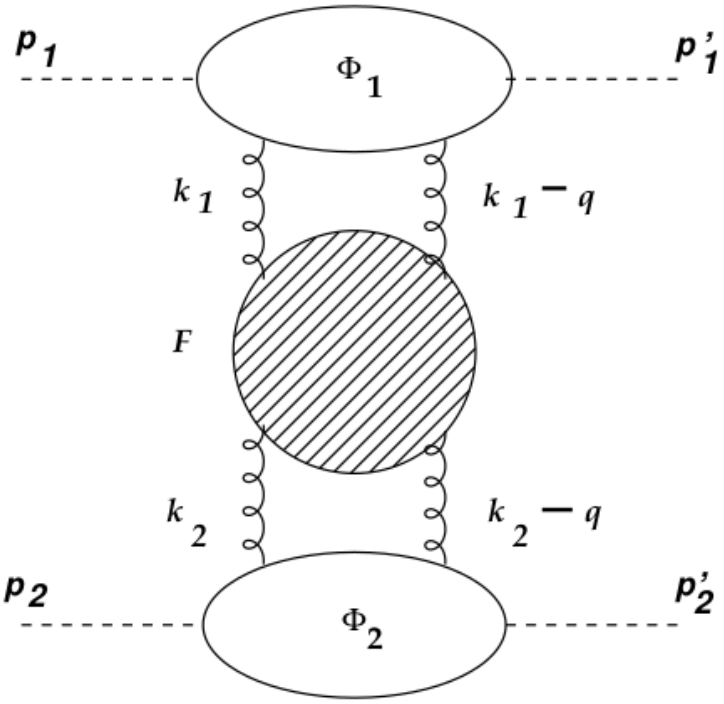

Figure 3.2 – The amplitude $A(\omega, t)$ in the high energy regime. Extracted from [88].

The integral above is divergent and must be regularized. The function $\omega(t)$ sets the negative signature of the Regge trajectory concerning the *reggeized* gluon $\alpha(t) = 1+\omega(t)$. According to Eq. (3.6), $\omega(t) = 0$ for $t = 0$ and therefore $\alpha(t = 0) = 0$, what is the expected result for a spin-1 particle as the gluon.

From Eq. 3.1 and using the optical theorem, one can obtain the total cross section of the elastic scattering of two quarks (the thorough analysis may be found in the original BFKL articles, Refs. [8, 9], as well as in the celebrated book of Forshaw and Ross [89]):

$$\sigma_{tot} = \frac{ImA(s,0)}{s} \ . \tag{3.7}$$

The Mellin transform of the amplitude $A(s,t)$ in Eq. (3.1) is given by

$$A(\omega,t) = \int_1^\infty d\left(\frac{s}{s_0}\right)\left(\frac{s}{s_0}\right)^{-\omega-1}\frac{ImA(s,t)}{s} \ . \tag{3.8}$$

Fig. 3.2 shows the schematic of the amplitude above. After several steps, it reads as

$$A(\omega,t) = \frac{\mathcal{G}}{(2\pi)^4}\int \frac{d^2\vec{k_1}\ d^2\vec{k_2}}{\vec{k_2}^{\,2}(\vec{k_1}-\vec{q})^2}\Phi_1(\vec{k_1},\vec{q})\ \Phi_2(\vec{k_2},\vec{q})\ F(\omega,\vec{k_1},\vec{k_2},\vec{q}) \ . \tag{3.9}$$

Above, $\mathcal{G} = (N_c^2-1)/4N_c^2$ and $t = -\vec{q}^{\,2}$. The impact factors denoted by the Φ's are those of slightly off-shell quarks and regulate the infrared divergence. They are written

as $\Phi_i = \alpha_s \delta_{\lambda\lambda'}$. The function F is driven by the BFKL equation. For $t = 0$ (forward direction),

$$\omega F(\omega, \vec{k_1}, \vec{k_2}, 0) = \delta^2(\vec{k_1} - \vec{k_2}) + \frac{\bar{\alpha_s}}{\pi} \int \frac{d^2\vec{k'}}{(\vec{k_1} - \vec{k'})^2}$$
$$\times \left[F(\omega, \vec{k'}, \vec{k_2}, 0) - \frac{\vec{k_1}^2}{\vec{k'}^2 + (\vec{k_1} - \vec{k'})^2} F(\omega, \vec{k_1}, \vec{k_2}, 0) \right] \ , \tag{3.10}$$

where $\bar{\alpha_s} = N_c \alpha_s / \pi$. The integral above contains a divergence at $\vec{k'} = \vec{k_1}$. Howbeit, this divergence is canceled by the second term in the square brackets of Eq. (3.10). This term corresponds to virtual corrections yielding *reggeization* of the exchanged gluons, while the first term in the square brackets is related to real gluon emission.

Applying the inverse Mellin transform to Eq. (3.7), one obtains the final expression for the total cross section:

$$\sigma_{tot} = \frac{\mathcal{G}}{(2\pi)^2} \int \frac{d^2\vec{k_1}}{k_1^2} \frac{d^2k_2}{k_2^2} \Phi_1(\vec{k_1}, 0) \Phi_2(\vec{k_2}, 0) \mathcal{F}(s, \vec{k_1}, \vec{k_2}, 0) \ . \tag{3.11}$$

The function $\mathcal{F}$ is obtained through the inverse Mellin transform of F and reads as

$$\mathcal{F}(s, k_1, k_2, 0) = \frac{1}{\pi k_1^2} \int_C \frac{d\gamma}{2\pi i} \left(\frac{k_1^2}{k_2^2} \right)^\gamma \int_C' \frac{d\omega}{2\pi i} \left(\frac{s}{s_0} \right)^\omega \frac{1}{\omega - \bar{\alpha} \mathcal{K}(\gamma)} \ , \tag{3.12}$$

where $\mathcal{K}(\gamma)$ is the Lipatov kernel defined in the following way:

$$\mathcal{K}(\gamma) = \int_0^\infty \frac{dv}{v} \left[\frac{v^\gamma - 1}{|v - 1|} + \frac{1}{\sqrt{4v^2 + 1}} \right] . \tag{3.13}$$

In the high energy limit, the asymptotic behavior of the above function is obtained (see Ref. [88] for a detailed and complete analysis):

$$\mathcal{F}(s, k_1, k_2, 0) = \frac{1}{\pi \sqrt{k_1^2 k_2^2}} \left(\frac{s}{s_0} \right)^{\bar{\alpha_s} \mathcal{K}(1/2)} \frac{e^{\frac{-\ln^2(k_1^2/k_2^2)}{2\bar{\alpha_s}\mathcal{K}''(1/2)\ln(s/s_0)}}}{\sqrt{2\pi \bar{\alpha_s} \mathcal{K}''(1/2) \ln(s/s_0)}} \ , \tag{3.14}$$

where $\mathcal{K}''$ stands for the second derivative of the Lipatov kernel. In particular, $\bar{\alpha_s}\mathcal{K}''(1/2) = 28\bar{\alpha_s}\zeta(3)$. The exponent of (s/s_0) in Eq. (3.14) may be defined as ω_0 and its value is given by $\bar{\alpha_s}\mathcal{K}(1/2) = 4\bar{\alpha_s}\ln 2$. Adopting $\bar{\alpha_s} \approx 0.2$, one gets $\mathcal{F} \sim s^{0.5}$, and this indicates a strong rise of $\mathcal{F}$ in terms of the energy. The total cross section follows the same behavior of this function, i.e., $\sigma_{tot} \sim s^{0.5}$, but such behavior is tamed by the saturation phenomena as s increases, otherwise the unlimited growth of the total cross section would violate the fundamental principle of unitarity.

For the case of DIS at small-x, assuming that the virtual photon fluctuates into a quark-antiquark pair, then the gluon ladder couples to this dipole and to the proton. Hence, Eq. (3.11) is written as

$$\sigma_\lambda = \frac{\mathcal{G}}{(2\pi)^2}\int \frac{d^2\vec{k_1}}{k_1^2}\frac{d^2k_2}{k_2^2}\Phi_\lambda(\vec{k_1},0)\Phi_p(\vec{k_2},0)\mathcal{F}(s,\vec{k_1},\vec{k_2},0) \quad , \tag{3.15}$$

where λ stands for the photon polarizations, being either T (transverse) or L (longitudinal). The $\Phi_{\lambda(p)}$ is the photon (proton) impact factor, respectively. The quantity s was replaced by Q^2/s. Due to gauge invariance, $\Phi_\lambda(\vec{k_1}=0,0)=\Phi_p(\vec{k_2}=0,0)$, which avoids infrared divergence of the cross sections.

The virtual photon impact factor is the hard cross section of the subprocess $\gamma^* + g(k) \to q + \bar{q}$, evaluated in pQCD (perturbative QCD) to the lowest order in α_s in terms of transverse momentum of the incoming off-shell gluon with $k \simeq xp + k_\perp$ and $k^2 = -\vec{k^2}$. For the process above, the two relevant diagrams may be seen in Fig. 3.3.

As the virtual photon impact factor is a nonperturbative quantity, the only way to proceed is by modeling it. From Eq. (3.15), we define a function named as unintegrated gluon distribution, which will embed the proton form factor as well as its impact factor:

$$f(\vec{k},x) = \frac{1}{(2\pi)^3}\int \frac{d^2\vec{k_2}}{\vec{k_2}}\Phi(\vec{k_2},0)\vec{k}^2\mathcal{F}(x,\vec{k},\vec{k_2},0) \quad . \tag{3.16}$$

Therefore, Eq. (3.15) is rewritten as

$$\sigma_\lambda(x,Q^2) = \int \frac{d^2\vec{k}}{\vec{k}^4}\Phi_\lambda(Q^2,\vec{k})f(x,\vec{k}) \quad . \tag{3.17}$$

The factor $\mathcal{G}/2\pi$ was embedded in the definition of the photon impact factor in the previous equation. Eq. (3.17) is termed k_T-factorization formula. If its collinear limited is taken, for very large Q^2 the gluon distribution function (used in DGLAP equations) is calculated from the unintegrated gluon distribution function as below:

$$xg(x,Q^2) = \int_0^{Q^2}\frac{d^2k}{k^2}f(x,k^2) \quad , \tag{3.18}$$

where it was assumed a spherical symmetry for $\vec{k}$.

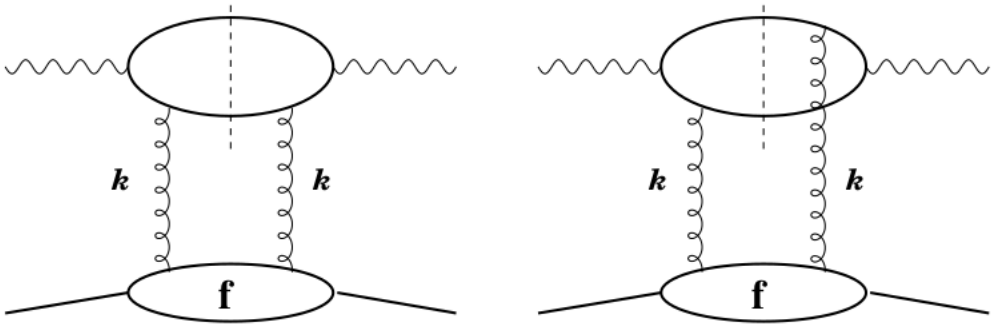

Figure 3.3 – The photon impact factor diagrams. Taken from [88].

3.2 Dipole picture

The dipole picture is a suitable way to deal with scattering processes at high energies. In this formalism applied to DIS, the virtual photon is decomposed into its Fock states, being the leading one the quark-antiquark contribution: $|\gamma^*\rangle = |q\bar{q}\rangle + ...$ If higher orders are neglected, we only consider the $q\bar{q}$ color singlet state interacting with the target, as seen in Fig. 3.4. The variable $r \sim 1/Q$ stands for the transverse separation between the quarks. Q^2 is the photon virtuality ($Q^2 = -q^2$) and P represents the proton target with momentum P (it could be either a nucleus).

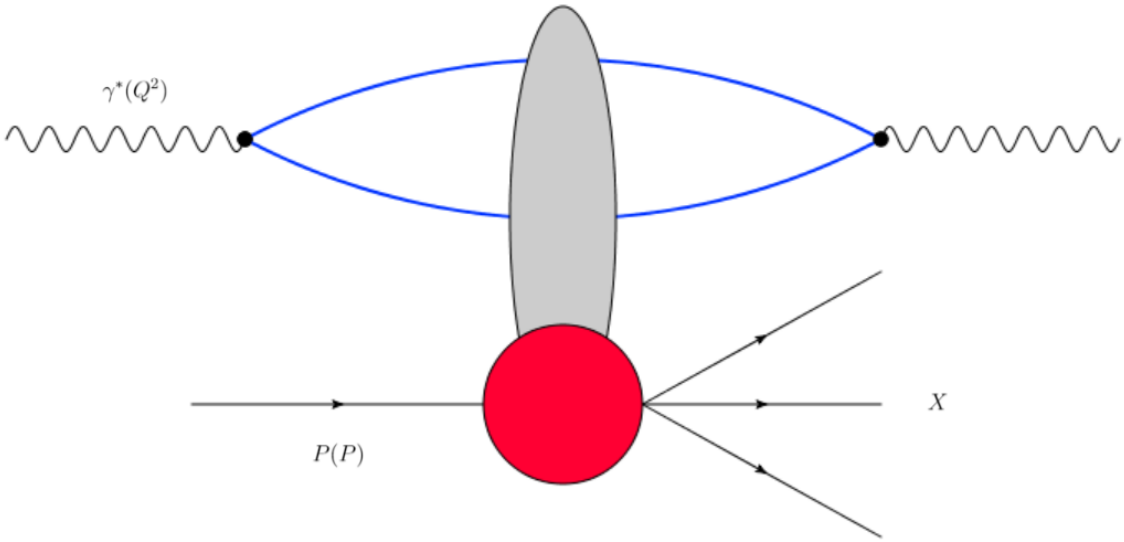

Figure 3.4 – The dipole picture.

At high energies, one can split the diagram in Fig. 3.4 into two stages: a) the virtual photon fluctuating into its Fock states, where the leading contribution is a quark-antiquark pair; b) the dipole interacting with the target which can be either a proton or a nucleus. As

the time of the photon fluctuating in the quark-antiquark pair is much larger than the time of interaction among this pair and the proton (nucleus), such mechanism of factorization facilitates the calculation procedure since the first subprocess is entirely described by QED while the second one is driven by QCD.

The first stage of the process is described by the photon wave function, a well defined quantity in QED that represents the probability of the photon decaying into the dipole. The wave functions corresponding to the photon (with transverse and longitudinal polarizations) are taken from light cone perturbative theory and their expressions are

$$|\Psi_T(z,\vec{r},Q^2)|^2 = \frac{6\alpha_{em}}{4\pi^2}\sum_f e_f^2[z^2(1-z)^2]\epsilon^2 K_1^2(\epsilon r) + m_f^2 K_0(\epsilon r)\ , \tag{3.19}$$

$$|\Psi_L(z,\vec{r},Q^2)|^2 = \frac{6\alpha_{em}}{\pi^2}\sum_f e_f^2[Q^2 z^2(1-z)^2 K_0^2(\epsilon r)]\ , \tag{3.20}$$

where Ψ_L represents the longitudinal part of the wave function, whereas Ψ_T stands for its transverse contribution. The variable $z(1-z)$ accounts for the longitudinal momentum fraction of the quark (antiquark). The quantity m_f is the quark mass with flavor f and K_0 and K_1 are the Modified Bessel Functions of the second kind of order zero and one, respectively.

The second stage is purely driven by QCD and is characterized by the dipole cross section, regarded to the interaction among the dipole and the target. Therefore, one may calculate the total cross section in the following way:

$$\sigma_{tot}(x,Q^2) = \int dz\ d^2\vec{r}\ (|\Psi_T|^2 + |\Psi_L|^2|)\ \sigma_{dip}\ , \tag{3.21}$$

where σ_{dip} is the dipole cross section which can be written in terms of the dipole amplitude, i.e.,

$$\sigma_{dip} = 2\int d^2\vec{b} N(x,\vec{r},\vec{b})\ . \tag{3.22}$$

In the expression above, $\vec{b}$ represents the impact parameter and $N(x,\vec{r},\vec{b})$ is the dipole-proton scattering amplitude, commonly extracted from phenomenological models. Equivalently,

$$\frac{d\sigma_{dip}(x,\vec{r})}{d^2\vec{b}} = 2N(x,\vec{r},\vec{b})\ . \tag{3.23}$$

Having the previous definition, the proton inclusive structure function is expressed as

$$F_2(x,Q^2) = \frac{Q^2}{4\pi^2\alpha_{em}} \sum_f \int dz\ d\vec{r}\ d\vec{b}\ \left(|\Psi_T^f|^2 + |\Psi_L^f|^2\right) \frac{d\sigma_{dip}(x,\vec{r})}{d^2\vec{b}}\ . \tag{3.24}$$

While F_2 is related to transverse and longitudinal parts of the photon wave function, F_1 is only connected to the transverse contribution:

$$2xF_1(x,Q^2) = \frac{Q^2}{4\pi^2\alpha_{em}} \sum_f \int dz\ d\vec{r}\ d\vec{b}\ |\Psi_T^f|^2 \frac{d\sigma_{dip}(x,\vec{r})}{d^2\vec{b}}\ . \tag{3.25}$$

Recalling what was already commented in the previous section, the relation among F_2 and F_1 and is given by

$$F_L(x,Q^2) = F_2(x,Q^2) - 2xF_1(x,Q^2)\ . \tag{3.26}$$

In the naive Parton Model, $F_L = 0$ and it is the so-called Callan-Gross relation [30]. In general words, one can say that while F_1 informs the number of partons with longitudinal momentum fraction x in the hadron, F_2 informs the average of the partons longitudinal momentum fraction multiplied by the number of partons. For a thorough study on the dipole picture, we quote Ref. [23].

Equation (3.21) reflects the k_T-factorization theorem, and this shall be interpreted in the proton rest frame. The formation time of the $q\bar{q}$ pair is regarded to the uncertainty on the energy of the pair, $t_{q\bar{q}} \sim 1/\Delta E$. At high energies (small-x limit), we have that $\Delta E \approx xM_P$ in the proton rest frame (see Ref. [89]). Hence, the formation time $t_{q\bar{q}}$ is much greater than the time of interaction between the dipole and the target, $t_{int} \sim 1/M_P$. Therefore, $t_{q\bar{q}} \gg t_{int}$.

The explanation above means that in the regime of small-x the dipole is formed much before the interaction takes place, and this is described by the photon wave function $\Psi(z,\vec{r},Q^2)$. Afterwards, the dipole scatters off the proton with its coordinates kept frozen during the time of the interaction. Thereupon, one can understand $\sigma_{dip}(x,\vec{r})$ as the cross section of a $q\bar{q}$ with transverse separation r scattering off a proton.

The dipole total cross is obtained from a UGD via its inverse Fourier transform [90–92]:

$$\sigma_{dip}(x,\vec{r}) = \frac{4\pi}{3}\alpha_s \int \frac{d^2k_\perp}{k_\perp^2}(1 - e^{i\vec{k_\perp}.\vec{r}})\phi(x,k_\perp^2) \tag{3.27}$$

where we denoted the UGD by ϕ (we will use this letter when referring to UGDs hereafter).

3.3 Parton saturation

In contrast to the photon (which does not carry electric charge), gluons carry color charge and thus are able to undergo the process of gluon splitting. In other words, it means that a gluon is able (with a certain probability) to radiate other gluons. Each of these gluons has lower energy than their predecessor. This process of gluon splitting keeps increasing the number of partons inside hadrons and nulei as x decreases. However, there is a specific point at which gluons start to recombine. The new gluon that is produced has higher energy than the merged gluons, resulting in a reduction of the gluons with smaller momenta. The dynamical balance between gluon splitting and recombination is named saturation effect [25].

Quantitatively speaking, if one takes the DLA of DGLAP to analyze the gluon distribution function,

$$xg(x,Q^2) \sim \exp[2\sqrt{\bar{\alpha_s}\log(Q^2/Q_0)\log(1/x)}] \ . \tag{3.28}$$

It can be clearly seen that it strongly increases when $Q^2 \to \infty$ or $x \to 0$. The same thing is attested in the next-to-leading order BFKL approach (see the step-by-step demonstration of it in Ref. [88]).

In a frame where the proton momentum is very large, $xg(x,Q^2)$ informs the number of gluons per unit of rapidity of transverse size of the order $1/Q$. The transverse area that is occupied by the gluons is given by the gluon cross section, $\sigma_{gg} \sim \alpha_s(Q^2)/Q^2$, multiplied by the number of gluons. In case this area is comparable to the proton transverse area [88],

$$\frac{\alpha_s(Q^2)}{Q^2} xg(x,Q^2) \sim \pi R^2 \ , \tag{3.29}$$

this generates an overlap in the gluons of the proton and recombination effects start to set it. Furthermore, one can assign a critical point where this effects begin, and this is referred as the saturation scale, $Q_s(x)$. The saturation scale establishes a line that separates the linear regime of QCD from the non-linear one. In the linear regime, DGLAP and BFKL approaches are applicable, whereas for the non-linear domain other formalisms ought to be used, namely the GLR-MQ [93, 94] and BK equations, for example. Much beyond the critical line defined by the saturation scale, the perturbative QCD is no longer valid and only non-pertubative approaches are applicable in the study of this domain, such as Regge

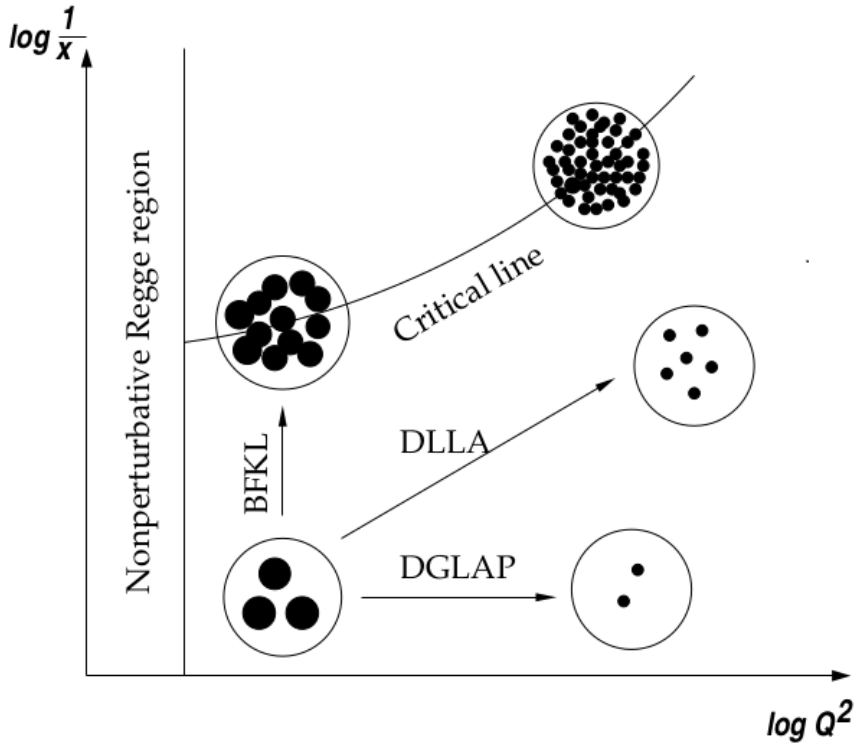

Figure 3.5 – The kinematic domains of QCD. Extracted from [88].

phenomenology and Lattice QCD, for instance. In Fig. 3.5 it is displayed the kinematic domains of QCD, as well as where each equation is valid and the saturation scale (denoted as "critical line"in the figure).

In the processes investigated in present work. the parton saturation phenomenon will be taken into account. In particular, in the diffractive gluon jet production in ep and eA collisions the saturation scale can be extracted from data.

4 Electron-ion colliders

In this chapter we will expose the existing projects of electron-ion colliders. Firstly we analyze the EIC, whose construction has been already approved by the U.S. Department of Energy. There is no estimate for its conclusion, but the particle physics community expectation is that it will be ready for the first run within nearly 10 years.

Secondly, we address the LHeC and the FCC, whose projects belong to CERN. Their constructions have not been approved yet, but plenty of studies and predictions have been already done by the particle physics community involving the design parameters that would be available at these machines.

4.1 EIC

In Janury 2020, the U.S. Department of Energy (DoE) announced that the upcoming Electron-Ion Collider (EIC) will take place at the Brookhaven National Laboratory (BNL), in Upton, New York. This long-awaited machine is expected to bring the possibility of unveiling several nuclear physics measurements in a completely new kinematical domain that still remain unexplored and, not surprisingly, is considered as one of the next physics frontiers.

Initially, there were two projects being considered in U.S. for the next electron - ion collider. The first, called JLEIC, was intended to be built at the Jeferson Lab (JLAB). This machine would employ a new electron and ion ring complex along with the upgrated CEBAF (Continuous Electron Beam Accelerator Facility).

The second project was named eRHIC and planned to be carried out at the BNL. The eRHIC design uses a new electron beam facility based on an Energy Recovery LINAC[1] (ERL). It is aimed to be built inside the RHIC tunnel where it will collide with high energy polarized protons and ion beams from RHIC.

Even though both projects had gained importance in the last years, the DoE established the BNL as the site for the forthcoming electron-ion collider. After that, the machine assumed the name of EIC (Electron - Ion Collider) rather than the previous project name eRHIC. As pointed out above, the EIC will utilize the RHIC's structure.

[1] Linear accelerator.

Additionally, this will be added an electron ring, injector and cooler (see the schematic of the EIC in Fig. 4.1). This facility is proposed to achieve [2]:

- High collision luminosity $\sim 10^{33-34}$ cm^{-2} s^{-1};
- Highly polarized (~ 70 %) electron and nucleon beams;
- Changeable center of mass energies from ~ 20 to ~ 100 GeV, upgradeable to ~ 150 GeV;
- Ion beams from deuteron to the heaviest nuclei (lead or uranium);
- Opportunities of having several interaction regions.

Apart from the hadron storage ring from the existing RHIC (which delivers an energy range of 40-275 GeV), the following will be new at the EIC:

- **Electron storage ring: 2.5-18 GeV**;
  - Electron bunch: $N_e \leq 1.7 \times 10^{11}$;
  - Beam current: 2.5 A;
- **Electron rapid cycling synchrotron;**
  - Frequency: 1-2 Hz;
  - Spin transparent caused by high periodicity;
- **High luminosity interaction region;**
  - Crossing angle: $\theta = 25$ mrad;
  - Number of bunches: $n_b = 1160$;
  - Superconducting magnets;
  - Spin rotators (longitudinal spin);
  - Forward hadron intrumentation.

Together with the fact of opening a new window in particle physics experiments, the EIC will push the accelerator designs to the boundary of current technologies, thus demanding great research and development. As examples of some technologies that have been idealized in the last years one may cite the compact (fiber sampling and crystal) calorimetry, tracking (NaI coated GEMs, GEM size and geometries), particle identification

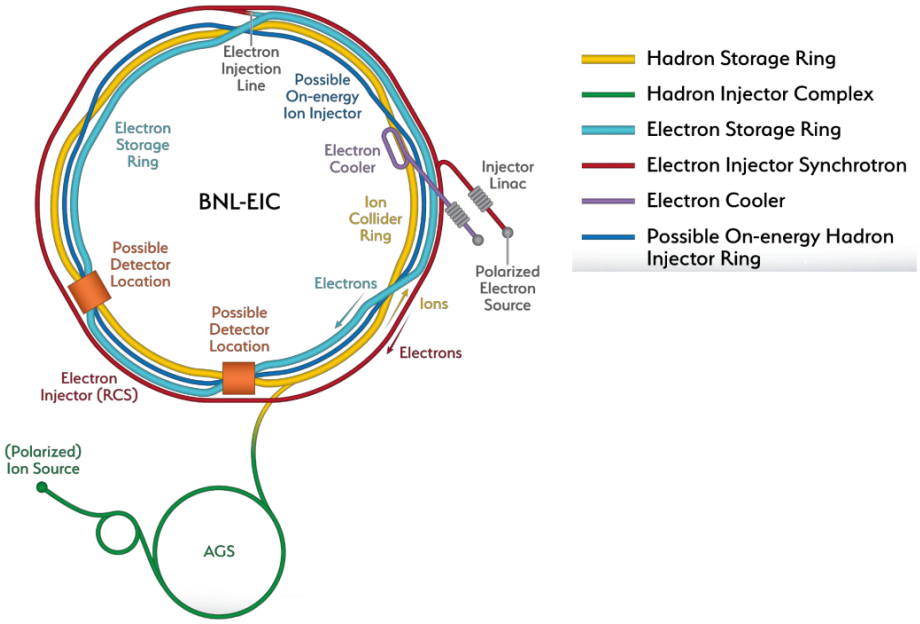

Figure 4.1 – The schematic of the EIC. Taken from [95].

(compact DIRC[2], dual radiator RICH[3] and novel TPC[4]) and high radiation tolerance for electronics. These will maintain U.S. at the forefront of nuclear science and strongly boost the accelerator and detector technologies.

The nucleus can be seen as a "QCD molecule" having a complex structure of bounded nucleons. Understanding the formation of nuclei in QCD is an ultimate long-term goal of nuclear physics. Through its broad kinematic coverage (see Fig. 4.2), the EIC will be the first machine able to study the three-dimensional sea quarks and gluons structure of a fast-moving nucleus. Moreover, nuclei are ideal "QCD laboratories" to explore the behavior of gluon dynamics at high occupation numbers, enabling one to perform a careful analysis towards the non-linear regime of QCD. Colliding electrons with protons and different nuclei and producing snapshots of the particle's internal structure, this forthcoming machine is crucial to explore the matter at its fundamental level. It will be capable of reproducing conditions close to the Big Bang and its future results will undoubtedly power the technologies of tomorrow.

[2] DIRC (Detection of Internally Reflected Cherenkov light) is a ring imaging Cherenkov detector based on total internal reflection and uses long, rectangular bars made from synthetic fused silica ("quartz") as both radiator and light guide.

[3] RICH (Ring-Imaging Cherenkov) is a device for discriminating the type of an electrically charged subatomic particle of known momentum that traverses a transparent refractive medium.

[4] TPC (Time Projection Chamber) is a sort of particle detector that utilizes a combination of magnetic and electric fields alongside a sensitive volume of gas or liquid to execute a three-dimensional reconstruction of a particle trajectory or interaction.

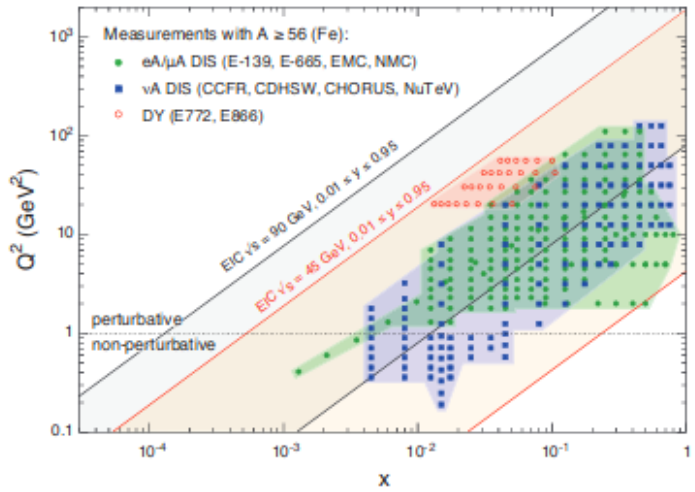

Figure 4.2 – Comparison between the phase space coverage of the EIC and the existing experiments on nuclear DIS. We notice that the EIC will open a completely new kinematical domain at small-x where no measurement exits in the region where saturation is expected to occur. [2]

The EIC will be a new kind of machine compared to the past facilities, becoming not only the world's first polarized electron-ion collider, but also the world first electron-nucleus collider [96]. Physicists will be able to answer fundamental questions that still remain unanswered, such as: where is the exact point where saturation effects set in? How does the nuclear environment affect the distribution of quarks and gluons and how they interact in nuclei? How are the sea quarks and gluons and their spin distributed in space and momentum inside a nucleon? These questions are only a few examples of what will be

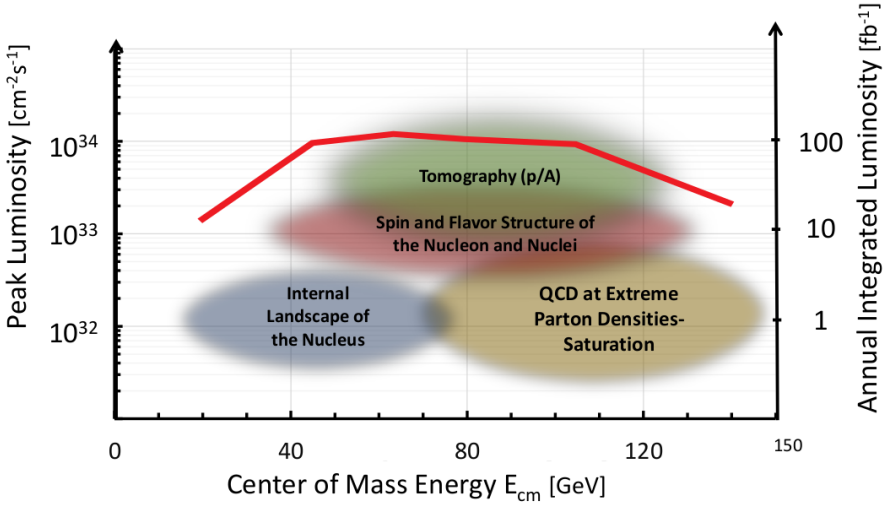

Figure 4.3 – EIC capability overview. Taken from [95].

clarified through the EIC [2]. In Fig. 4.3 it is displayed the kinematic regions where there are specific issues to be looked into.

4.2 LHeC and FCC-eh

Alongside the U.S. project for an electron - ion collider, the CERN has also developed an electron - ion collider programme named as Large Hadron electron Collider (LHeC), to be built at the existing LHC. Differently from the EIC, the LHeC is proposed to be a TeV energy scale electron-proton (ion) collider. In addition, this is designed to be compatible with concurrent operation of the LHC.

The 2012 Conceptual Design Report (CDR) for the LHeC [97] showed that DIS at the LHeC has a great potential and a crucial role in keeping and evolving the LHC programme, taking into account the results from the experiments at the LHC: discovery of Higgs boson, no observation of exotic particles beyond the SM and no detection of SUSY particles. The LHeC is a major opportunity for leveraging the studies in particle physics and comprises an ambitious and exciting physics programme, the development of novel accelerator technology and the maximum exploitation of the existing and upcoming LHC structure.

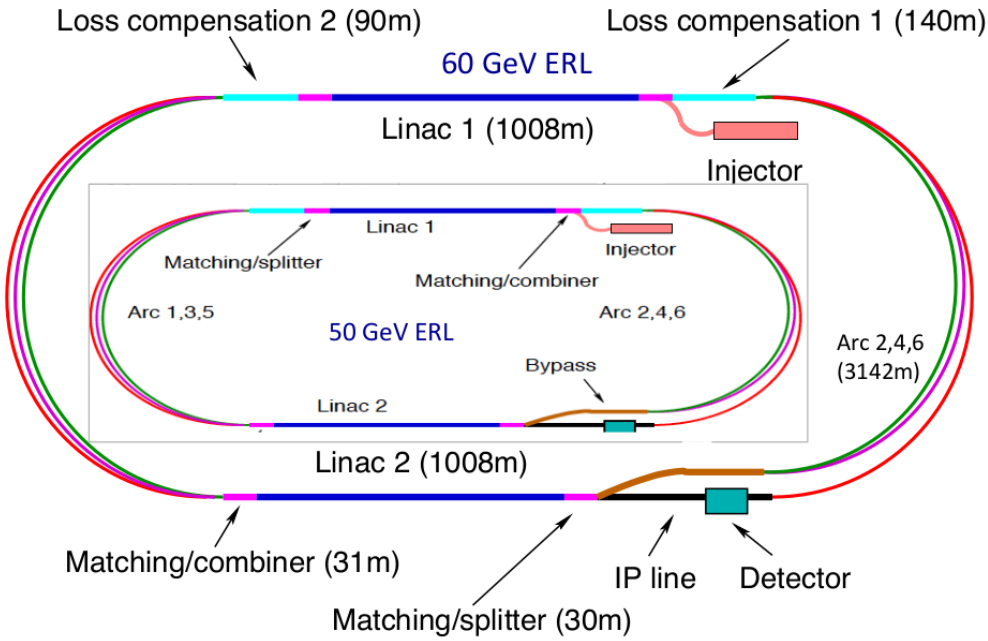

Figure 4.4 – Schematic of the LHeC with two possible configurations: $E_e = 60$ GeV and $E_e = 50$ GeV. Taken from [3].

Table 4.1 – LHeC parameters in electron-ion mode. Table extracted from [3].

Parameter	**LHeC**	**FCC-eh** ($E_p = 20$ TeV)	**FCC-eh** ($E_p = 50$ TeV)
Ion energy E_{Pb} (PeV)	0.574	1.64	4.1
Ion energy/nucleon E_{Pb}/A (TeV)	2.76	7.88	19.7
Electron beam energy E_e (GeV)	50	60	60
Electron-nucleon c.m.s $\sqrt{s_{eN}}$ (TeV)	0.74	1.4	2.2
Bunch spacing (ns)	50	100	100
Number of bunches	1200	2072	2072
Ions per bunch (10^8)	1.8	1.8	1.8
Normalized emittance ϵ_n (μ m)	1.5	1.5	1.5
Electrons per bunch (10^9)	6.2	6.2	6.2
Electron current (mA)	20	20	20
IP beta function β_A^* (cm)	10	10	15
e-N luminosity ($10^{32}\text{cm}^{-2}\text{s}^{-1}$)	7	14	35

The CDR default configuration establishes a 60 GeV energy for the electron beam originated from a racetrack, three-turn, high energy ERL reaching a center-of-mass energy of 1.3 TeV. As mentioned above, the LHC has not discovered any exotic particle so far. Such fact yields the seek for high precision measurement both in pp (A) and ep (A) collisions in order to reach maximum kinematical coverage in the phase space to pursue for rare channels. Furthermore, searches and possible measurements of SUSY particles, heavy neutrinos and new physics overall are more likely to occur the higher the energy is. Perturbative QCD (pQCD) demands $Q^2 \gtrsim 1$ GeV and the kinematic domain of DIS requires high energies since $x \approx Q^2/s$ in case where the inelasticity is one.

The established default electron energy of 60 GeV can be reached through a circumference of 1/3 of that of the LHC. Afterwards, in order to optimize the cost, the electron energy was redefined as 50 GeV having the option to start with 30 GeV. This latter configuration is planned to have a circumference of 5.4 km, which is equivalent to 1/5 of the LHC length. The schematic of the LHeC, taking into consideration the two possible electron beam energies (50 and 60 GeV) may be seen in Fig. 4.4. The design parameters for the LHeC in electron-ion mode operating with an electron beam energy of 60 GeV are displayed in Table 4.1.

The LHeC would provide a significant extension of the DIS kinematic range. This is a basic requirement for physics research at the energy frontier. Concerning the LHC, the ep(A) detector would become a new major experiment. Several topics that demand further

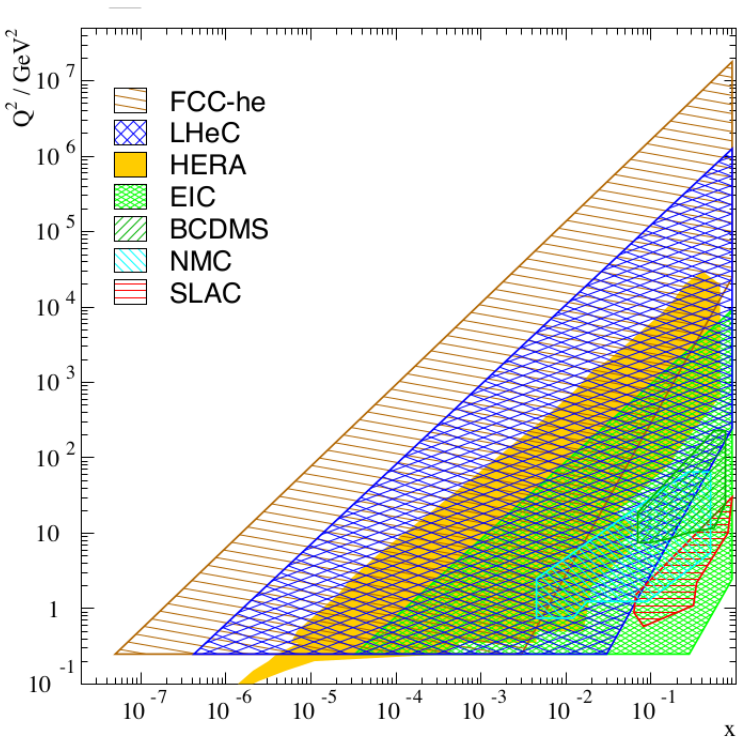

Figure 4.5 – Phase spaces covered by past, current and future ep(A) machines. Extracted from [3].

investigation would be explored with significant discovery and analysis potential. Utilizing the hadron and ion beams of the LHC and applying a point-like probe, the LHeC would become the world's most powerful, cleanest and high resolution microscope for exploring and studying the substructure of matter and its dynamics, perhaps being considered as a "Hubble telescope" for subatomic dimensions.

Beside the LHeC, the CERN has recently published a study of a future circular collider (named as FCC) in the hadron-hadron (hh), electron-hadron (eh) and electron-positron(e^+ e^-) collider complex. The FCC-eh would be an about 3 TeV center-of-mass energy collider and would drastically open the horizons in particle physics. Moreover, it would be able to operate in hA, AA and eA modes, delivering an unprecedented "QCD laboratory" to explore the structure of matter [3]. Table 4.1 shows the design parameters for the FCC-eh with proton beam energies of 20 and 50 TeV.

Such collider would have the potential to deeply change the paradigm of particle physics with high energy discoveries in the 10 TeV energy scale, what can only be reached through FCC-hh(A) along with an eh(A) experiment. The FCC-hh(A)/eh(A) complex could access physics to several hundred TeV and provide substantially new level of information concerning QCD and DIS. One of the principal aims of the FCC would be to

enlighten the Higgs vacuum potential that can not be achieved with e^+ e^- processes. In that sense, this collider has an overwhelming justification much beyond of finding new physics, i.e., measuring "exotic" particles. It has a potential to access rare Higgs boson decays, high scales and, whether combined with ep, it is capable of measuring the SM Higgs couplings to below percent precision. Therefore, this programme may hugely explore strong and electroweak interactions, as well as flavor and heavy ion physics. Due to its great size and cost, the FCC project needs to be established as a global enterprise. In this context, the High Luminosity LHC (HL-LHC) and the LHeC shall be seen as the first steps towards this major new machine, considering both the physics and technology aspects. [3]

In Fig. 4.5 one finds the phase spaces covered by each ep(A) collider. Noticeably, the LHeC and FCC could achieve regions that by far have not been reached by any past or current machines.

Comparing EIC with LHeC, the main difference concerns to the available center-of-mass energy. The typical energy collision of EIC is comparable to HERA machine, whereas LHeC involves TeV scale collisions. It is clearly expected that parton saturation effects would be more salient in TeV scale for a fixed probe hard scale. The scanned phase space in this case is quite amplified, as shown in Fig. 4.5.

5 Studied processes involving electron-ion collisions

In this chapter we present the results concerning the three processes involving electron-ion collisions that we have studied: diffractive gluon jet production, timelike Compton scattering and exclusive Z^0 production.

We will see that diffractive jets could be highly important in the context of saturation in electron-ion collisions. Such observable is directly connected with the saturation, enabling its determination from experiments. Also, we will analyze timelike Compton scattering applying the k_T-factorization approach in electron-nucleus collisions for the first time. Lastly, we investigate the exclusive Z^0 production also within the k_T-factorization framework in eA collisions.

5.1 Diffractive gluon jet production

In this study we aimed to investigate the gluon jet production in the diffractive photon dissociation in the context of the electron-ion colliders. In particular, we analyzed the case for future electron-proton/nucleus colliders in the GeV (EIC) and in the TeV (LHeC and FCC-eh) regimes . We considered the high diffractive mass, M_X, kinematic region with the final state configuration, $e + p(A) \to e' + X + \text{jet} + \text{gap} + p(A)$, having the (gluon) jet near to the edge of the rapidity gap. The definition of the diffrative mass is (see Fig. 5.1)

$$M_X^2 = \frac{k_{\perp q}^2}{z_q} + \frac{k_{\perp \bar{q}}^2}{z_{\bar{q}}} + \frac{k_{\perp g}^2}{z_g} \ . \tag{5.1}$$

At the LHeC and FCC-eh the range of available momentum fraction of the diffractive exchange with respect to the proton can reach down to $x_{I\!P} \simeq 10^{-5}$ for a large range of the momentum fraction of the parton relative to the diffractive exchange, $\beta = Q^2/(Q^2 + M_X^2)$ (with $x = \beta x_{I\!P}$). It was proposed in Ref. [98] that the measurement of the maximum of the differential cross section on the gluon (jet) transverse momentum $k_\perp$, i.e., $k_\perp^2 d^3\sigma_{\text{diff}}^\gamma / d^2k_\perp dM_X$, provides a direct measurement of the saturation scale as a function of $x_{I\!P} = (Q^2 + M_X^2)/(Q^2 + W^2)$. In that sense, we explored this possibility in what follows. Concerning the EIC, it seems to be very challenging to measure this type of events there as the kinematic reach for jet measurements at the EIC is found to be roughly

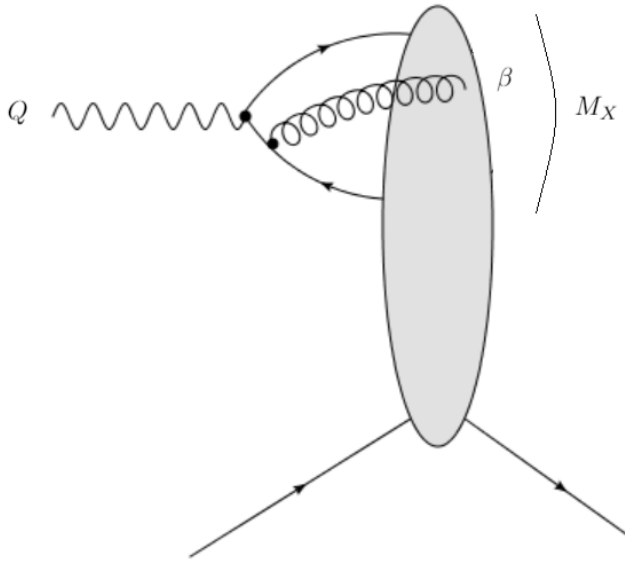

Figure 5.1 – Virtual photon dissociation into a quark-antiquark pair and a gluon. This is the leading contribution to the diffractive cross section in the regime where the diffractive mass is much greater than the photon virtuality.

$0.008 < x < 0.7$ and $Q^2 > 25$ GeV^2 for $\sqrt{s} = 89$ GeV [99]. However, there is a possibility of performing these measurements at high energy machines (LHeC and FCC-eh) or in ultraperipheral AA collisions with a rich content of quasi-real photons at the LHC.

This study can be complementary to recent investigations of diffractive dijet production in $\gamma^* h(A)$ collisions. In this context, below we summarize the main studies along this direction.

The exclusive dijet production is investigated in [100] within the CGC formalism at LO demonstrating that the azimuthal angle correlations and momentum transferred squared, t, distributions are sensitive to parton saturation at small-x. Important points are the relation between the increasing of saturation scale, $Q_{s,A}$, and an enhancement of away-side correlations as well as the presence of dips in t-dependence which is absent in non-saturation models. In Ref. [101] the angular correlation between the transverse momentum of the produced dijet and the recoiled momentum of the nucleon is investigated in the context of the quantum phase space of Wigner distribution of small-x partons. It was pointed out that the gluon Wigner distributions are closely related to the impact parameter dependent dipole and quadrupole scattering amplitudes and they could be measured in diffractive DIS in eA collisions at an electron-ion collider or in ultraperipheral collisions at the LHC. The last case was addressed using NLO (next-to-leading order)

pQCD in Refs. [102, 103] for both diffractive and inclusive dijet production. Similarly, in Ref. [104] the gluon in Wigner and Husimi distributions of nucleons were considered within the CGC formalism including numerical solution of the JIMWLK equations. The anisotropy of these distributions as a function of the angle between impact parameter and transverse momentum has been analyzed and signatures of these angular correlations were proposed for electron-ion colliders. Along the same lines, taking into account the multi-gluon correlations inside nuclear targets at small-x in Ref. [105], the elliptic modulation of diffractive dijets was investigated and it was shown that saturation effects are significant when looking at the nuclear modification of the ratio between the differential inclusive and diffractive dijet cross sections. Authors of [106] studied the soft gluon radiation associated with the final state jets and an all order resummation formula has been derived. They argued that soft gluon resummation plays an important role at electron-ion colliders and helps to explore the nucleus tomography. The impact parameter dependence was studied analytically (including elliptic anisotropy) for coherent diffractive dijet production in ep and eA collisions in Ref. [107]. General relations are found connecting angular correlations of the dipole orientation and b-vector in coordinate space with angular correlations between mean dijet $k_\perp$ and hadron recoil momentum. Finally, from theoretical point of view a complete NLO description of diffractive dijet production is carried out in Ref. [108], where the direct coupling of the Pomeron (viewed as a color singlet QCD shock wave) to the diffractive X state is considered. The numerical results are promising mostly at intermediate to large β values.

Here we aim to analyze the diffractive gluon jet production in diffractive dissociation of photons in DIS, investigating the nuclear effects when taking into account nuclei as targets. This is relevant for the physics to be studied at the EIC and the LHeC/FCC-eh machines. The starting point is to write the diffractive cross section in terms of the decomposition on the Fock states of the incident virtual photon, $|\gamma^*\rangle = |q\bar{q}\rangle + |q\bar{q}g\rangle \ldots$. The second Fock state includes the emission of a soft gluon (small longitudinal momentum fraction, z_g) off a $q\bar{q}$ dipole and its transverse momentum can be identified with the momentum of the jet closest to the rapidity gap. We are interested in this last component, which is dominant in the kinematic regime where the diffractive mass, M_X, is larger than the photon virtuality ($M_X^2 \gg Q^2$). The terms from jets initiated by quarks in such a kinematic interval are suppressed. In the Pomeron language, this corresponds to a momentum fraction of the parton with respect to the diffractive exchange having

$\beta \ll 1$. Although many kinematical configurations can provide such regime, the leading contribution for the cross section is given by the following configuration [98]:

$$\frac{k_{\perp g}^2}{z_g} \gg \frac{k_{\perp q}^2}{z_q} \ , \ \frac{k_{\perp \bar{q}}^2}{z_{\bar{q}}} \ , \ Q^2 \ . \tag{5.2}$$

In the reference quoted above, the diffractive cross section for the production of a gluon having transverse momentum $k_\perp$ and rapidity y in the collision of a $q\bar{q}$ of transverse size r with the target has been derived. The relevant diagrams include the cases where the interaction with the target takes place after and before the gluon emission (see Fig. 5.2). The corresponding differential cross section in leading $\ln(1/\beta)$ accuracy and small Q^2 is given by (the reader may find a thorough explanation concerning the procedure of deriving the expression below in [98] as well as in [109])

$$\frac{d\sigma_{\rm diff}^{q\bar{q}g}}{d^2k_\perp dM_X} = \frac{2M_X}{Q^2+M_X^2}\int d^2\vec{r}d^2\vec{b}\,\rho(r,Q^2)\frac{d\sigma_g(\vec{r},\vec{b})}{d^2k_\perp dy}, \tag{5.3}$$

$$\frac{d\sigma_g(\vec{r},\vec{b})}{d^2k_\perp dy} = \frac{\alpha_s N_c^2}{4\pi^2 C_F}\,A(k_\perp,x_{0,1};\Delta\eta)A^*(k_\perp,x_{0,1};\Delta\eta),$$

where $\rho(r,Q^2)=\int dz(|\psi_T^\gamma(r,z;Q^2)|^2+|\psi_L^\gamma(r,z;Q^2)|^2)$ and $x_{0,1}=b\pm(r/2)$ (x_0 and x_1 are the transverse positions of q and $\bar{q}$, respectively). The quantities $|\psi_T^\gamma(r,z;Q^2)|^2$ and $|\psi_L^\gamma(r,z;Q^2)|^2$ are the virtual photon wave functions whose expressions are defined in Eqs. (3.19) and (3.20), respectively. The rapidity gap is written as $\Delta\eta=\log(1/x_{I\!P})=Y-y$ with $Y=\log(1/x)$ being the total rapidity. The function $A(k_\perp,x_0,x_1;\Delta\eta)$ is written [98] in terms of the elastic S-matrix for the collisions of the dipole on the target evolved at the rapidity $\Delta\eta$, $S(x_0,x_1;\Delta\eta)$, and the elastic S-matrix for the collision of two dipoles, $S^{(2)}(X_0,x_g,x_1;\Delta\eta)$, where x_g is the gluon transverse coordinate. Regardless the specific form for S-matrices, the quantity $k_\perp^2 d\sigma/d^2k_\perp dM_X$ rises as $k_\perp^2$ for small gluon transverse momenta whereas falls as $1/k_\perp^2$ for large ones. A maximum occurs for a typical transverse momentum where parton saturation becomes important, i.e., $(k_\perp)_{max}\propto Q_s$ where $Q_s(x_{I\!P})$ is the saturation scale.

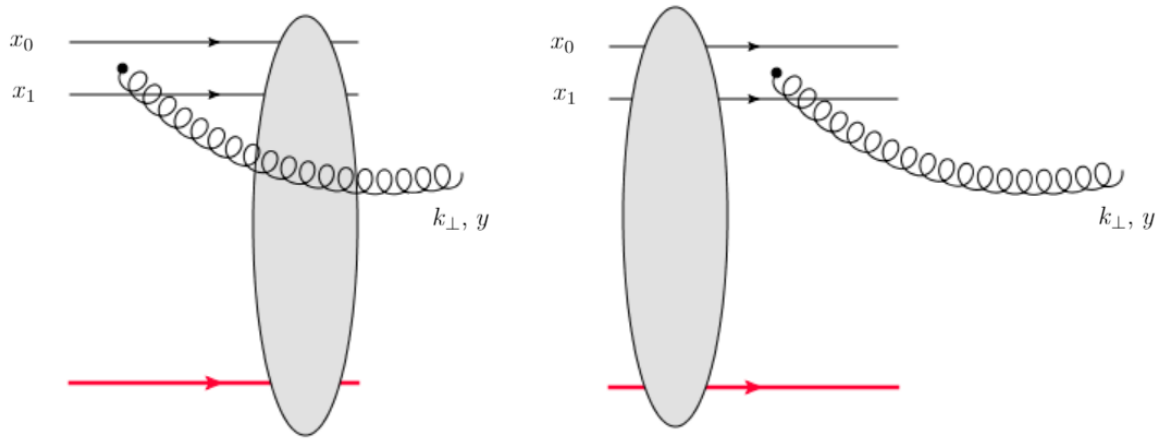

Figure 5.2 – Diffractive gluon jet production. The two diagrams show the emission of the gluon taking place before (l.h.s) and after (r.h.s) the interaction with the target.

Also, in Ref. [98] a simplified model for the S-matrices has been considered. Inspired in the GBW model [110] and neglecting correlations between the two dipoles in $S^{(2)}$, they read as

$$\begin{aligned} S(x_0,x_1;\Delta\eta) &= e^{-\frac{(Q_s r)^2}{4}}\Theta(R-|b|)+\Theta(|b|-R)\ , \\ S^{(2)}(x_0,x_1,x_g;\Delta\eta) &= e^{-\frac{Q_s^2[(x_0-x_g)^2+((x_g-x_1)^2]}{4}}\Theta(R-|b|) \\ &+ \Theta(|b|-R)\ , \end{aligned} \tag{5.4}$$

where R is the target radius and the saturation scale depends on the $x_{I\!P}$ variable. The theta function appearing in S-matrices will give an overall normalization factor after b-integration in Eq. (5.3) in the form $\bar{\sigma}_0 = \pi R^2$. The parameter $\sigma_0 = 2\pi R^2 = 2\bar{\sigma}_0 = 27.32$ mb for the proton target has been fitted against DESY-HERA data of proton structure functions at small-x [110]. In Ref. [111] a different model for the S-matrices has been considered, where the impact parameter dependence was factorized having a profile in the form $T(b) = e^{-b^2/(2B_D)}$, where $B_D \simeq 6$ GeV^{-2} is the diffractive slope and $\sigma_0 = 4\pi B_D$. Moreover, the $S^{(2)}$ is expressed in terms of the color dipole amplitude, $N(r, x_{I\!P})$, taken from Iancu-Itakura-Munier (IIM) [112] saturation model (with $S = 1 - N$). In particular, in the small-β limit it was considered $N^{(2)}(x_0, x_1, x_g, \Delta\eta) = N(|\vec{x}_0 - \vec{x}_g|Q_s, \Delta\eta) + N(|\vec{x}_g - \vec{x}_1|Q_s, \Delta\eta) - N(|\vec{x}_0 - \vec{x}_g|Q_s|, \Delta\eta)N(\vec{x}_g - \vec{x}_1|Q_s, \Delta\eta)$.

Taking into account the GBW-like parametrization, Eqs. (5.4), the integration over impact parameter in Eq. (5.3) can be done. That model contains the main features which

are also present in more sophisticated models for the dipole amplitude. This will give a semi-analytical expression for the differential cross section (with $|\vec{k}_\perp| = \kappa$):

$$\begin{aligned}\frac{d\sigma_{\rm diff}}{d^2k_\perp dM_X} &= \frac{\alpha_s N_c^2 \bar{\sigma}_0}{4\pi^2 C_F}\frac{M_X}{M_X^2+Q^2}\int dr^2 d\theta\, \rho(r,Q^2) \\ &\times \left(\frac{e^{-r^2Q_s^2/2}}{\kappa^2}\right)\frac{1}{\left[\frac{\kappa}{(rQ_s^2)}-\frac{rQ_s^2}{4\kappa}\right]^2+\cos^2\theta} \\ &\times \left[T_1(r,\kappa,Q_s)+T_2(r,\kappa,Q_s)+T_3(r,\kappa,Q_s)\right]\ ,\end{aligned} \tag{5.5}$$

where the auxiliary functions $T_{1,2,3}$ are written as

$$T_1 = \left[\cos\left(\frac{1}{2}\kappa r\cos\theta\right) - e^{-\kappa^2/(2Q_s^2)+Q_s^2r^2/8}\right]^2, \tag{5.6}$$

$$T_2 = \frac{Q_s^4 r^2}{4\kappa^2}\sin^2\left(\frac{1}{2}\kappa r\cos\theta\right), \tag{5.7}$$

$$\begin{aligned}T_3 &= \frac{rQ_s^2}{\kappa}\cos\theta\sin\left(\frac{1}{2}\kappa r\cos\theta\right) \\ &\times \left[\cos\left(\frac{1}{2}\kappa r\cos\theta\right) - e^{-\kappa^2/(2Q_s^2)+Q_s^2r^2/8}\right]\ .\end{aligned} \tag{5.8}$$

Before numerically computing the cross section above, it would be interesting to investigate its qualitative behavior. It is well known that the virtual photon overlap function times the dipole transverse size, $r\rho(r,Q^2)$, presents a peak at $r \simeq d/Q$ (with $d \approx 2$). Furthermore, in the region studied here, $M_X^2 \gg Q^2$, the prefactor $M_X^2/(M_X^2+Q^2) \to 1$. If one considers an angle averaged cross section, Eq. (5.5) simplifies to

$$\begin{aligned}\langle k_\perp^2 \frac{d\sigma_{\rm diff}}{d^2k_\perp dM_X}\rangle &\propto \frac{e^{-d^2Q_s^2/2Q^2}}{\left[\frac{\kappa Q}{(dQ_s^2)}-\frac{dQ_s^2/Q^2}{4\kappa}\right]^2+\frac{1}{2}} \\ &\times \left[\frac{1}{2} - e^{-\frac{\kappa^2}{Q_s^2}+\frac{d^2Q_s^2}{4Q^2}} + \frac{Q_s^4d^2}{4Q^2\kappa^2}\right],\end{aligned} \tag{5.9}$$

that for the case of $Q^2 \gg Q_s^2$ and assuming $d = 2$ gives the qualitative behavior

$$\langle k_\perp^2 \frac{d\sigma_{\rm diff}}{d^2k_\perp dM_X}\rangle \propto \frac{\frac{1}{2} - e^{-(\frac{\kappa^2}{Q_s^2})} + (\frac{Q_s^2}{Q^2})(\frac{Q_s^2}{\kappa^2})}{\left[\frac{1}{2}(\frac{\kappa}{Q_s})(\frac{Q}{Q_s}) - \frac{1}{2}(\frac{Q_s}{\kappa})(\frac{Q_s}{Q})\right]^2+\frac{1}{2}}, \tag{5.10}$$

which is a function dependent on the ratios κ/Q_s and Q/Q_s. For a fixed Q^2 and large $\kappa \gg Q_s$, the differential cross section falls as $1/\kappa^2$.

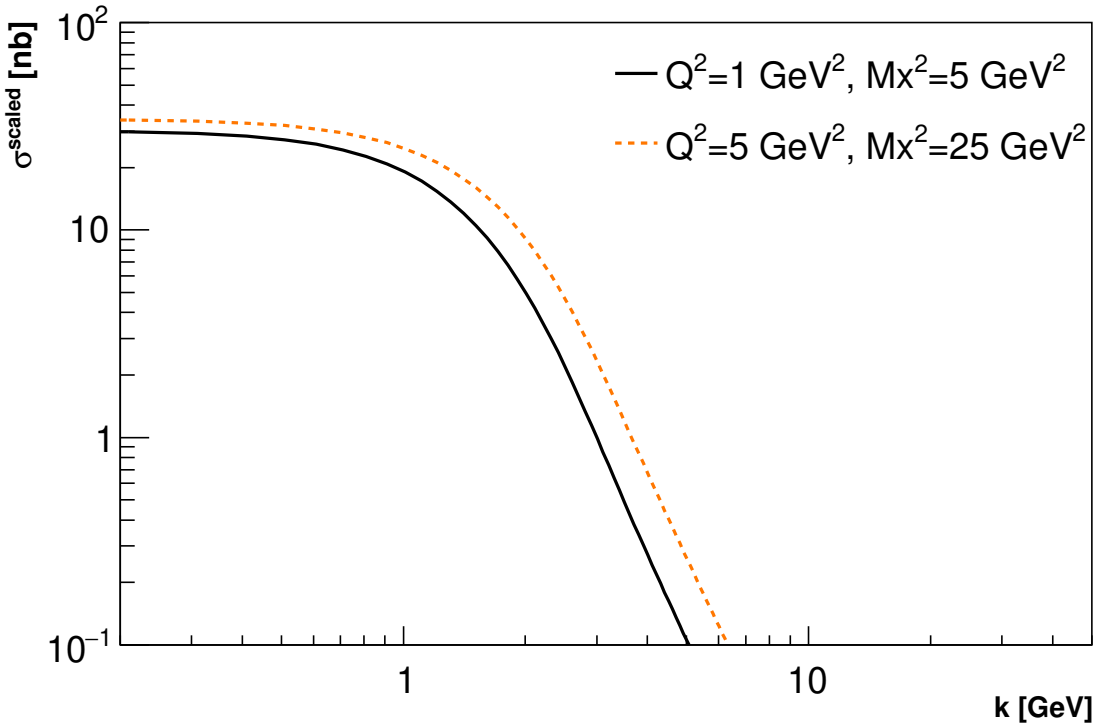

Figure 5.3 – Diffractive jet (gluon) production at EIC ($\sqrt{s} = 92$ GeV) as a function of jet transverse momentum κ for the configurations ($Q^2 = 1$ GeV^2, $M_X^2 = 5$ GeV^2) and ($Q^2 = 5$ GeV^2, $M_X^2 = 25$ GeV^2).

To avoid the uncertainties concerning the running coupling α_s and the parameter σ_0 (which comes from the GBW parametrization; see [113] for recent analyzes), the following quantity is defined:

$$\sigma^{\text{scaled}}(\kappa, Q^2, Q_s) = \frac{1}{\alpha_s \sigma_0} \left(\frac{M_X^2 + Q^2}{M_X^2} \right) M_X \frac{d\sigma_{\text{diff}}}{d^2 k_\perp dM_X} \, . \tag{5.11}$$

Let us now perform the corresponding phenomenology for diffractive gluon jet production in the context of electron-nucleus collisions. For the saturation scale for protons we consider the usual power-like behavior, $Q_{s,p}(x_{I\!P}) = (x_0/x_{I\!P})^{\lambda/2}$ GeV. The parameters λ and x_0 were taken by fitting HERA data and their values are $\lambda = 0.248$ and $x_0 = 4.2 \times 10^{-5}$, respectively [113]. The variable $x_{I\!P}$ represents the longitudinal momentum fraction carried by the Pomeron, what is the exchanged object in diffractive processes. In order to compute the nuclear saturation scale $Q_{s,A}$, we take the simple ansatz proposed in Ref. [114], where the growth on atomic number A depends on the quotient of the transverse parton densities to the power $1/\delta$:

$$Q_{s,A}^2(x_{I\!P}; A) = Q_{s,p}^2(x_{I\!P}) \left(\frac{A\pi R_p^2}{\pi R_A^2} \right)^{1/\delta} \, , \tag{5.12}$$

where $Q_{s,p} = (x_0/x)^{\lambda/2}$ GeV is the saturation scale of a single proton, R_p is the proton radius and R_A is the nuclear radius. For the latter, we take the usual parametrization $R_A = (1.12A^{1/3} - 0.86A^{-1/3})$. The quantities δ and πR_p^2 were fitted [114] from γA collisions at small-x and their values are 0.79 and $\pi R_p^2 = 1.55$ fm^2, respectively. Qualitatively, the nuclear saturation scale behaves like $Q_{s,A}^2 \simeq A^{\Delta} Q_{s,p}^2$ with $\Delta \approx 4/9$. Quantitatively, for gold ($A = 197$) and lead nucleus ($A = 208$) one gets $Q_{s,Au}^2 \approx 2.8\, Q_{s,p}^2$ and $Q_{s,Pb}^2 \approx 3\, Q_{s,p}^2$, respectively. This very same ansatz enables to describe the p_T-integrated multiplicity in symmetric AA collisions at mid-rapidity [114]. For processes probing perturbative typical scales like the photon virtuality $\mu^2 = Q^2$ or $\mu^2 = Q^2 + m_V^2$ as in case of vector meson production, an important part of observables are within the saturation region $\mu^2 \lesssim Q_s^2$.

As above commented, we have shown that $Q_{s,Au}^2 \approx 2.8\, Q_{s,p}^2$ and $Q_{s,Pb}^2 \approx 3\, Q_{s,p}^2$. Notice that the the value for the nuclear saturation scale can vary whether distinct treatments for the nuclear collision geometry are considered. For instance, using a local saturation scale, $Q_s^2(x,b) = Q_s^2(x, b=0) T_A(b)$ (with T_A being the nuclear thickness function), and a Gaussian b-profile, the relation between $Q_{s,A}$ and $Q_{s,p}$ is found [107]. In the hard sphere approximation for the nuclear density ρ_A, we have $Q_{s,A}^2 = 3A(R_p/R_A)^2 Q_{s,p}^2$. This will give $Q_{s,Au}^2 \approx 2.2 Q_{s,p}^2$ and $Q_{s,Pb}^2 \approx 2.3 Q_{s,p}^2$. Thus, typically the theoretical uncertainty on the determination of the saturation scale compared to that of the proton is of order of 20%. Accordingly, in nuclear case the overall normalization will be replaced as $\sigma_0 \to \sigma_A = 2\pi R_A^2$.

A different prescription for introducing nuclear effects can be used as writing down the S-matrices in terms of a Glauber model for the dipole-nucleus cross section, $N_A(x, r, b)$, using the model in Ref. [115], for instance. Another possibility is to consider the recently determined dipole amplitude depending on impact parameter determined from numerical solution of the BK equation with the collinearly improved kernel [116]. Eventually, it can be considered also the model of the proton as constituted by hot spots (representing regions of high gluon density), where its structure changes from interaction to interaction. This idea has been successfully applied for exclusive photonuclear production of vector mesons in Refs. [117, 118]. In the subsequent paragraphs we apply the geometric scaling ansatz of Eq. (5.12) for obtaining estimates of the differential cross section as a function of gluon transverse momentum for planned electron-ion machines bearing in mind the theoretical uncertainties in S-matrix in the nuclear case.

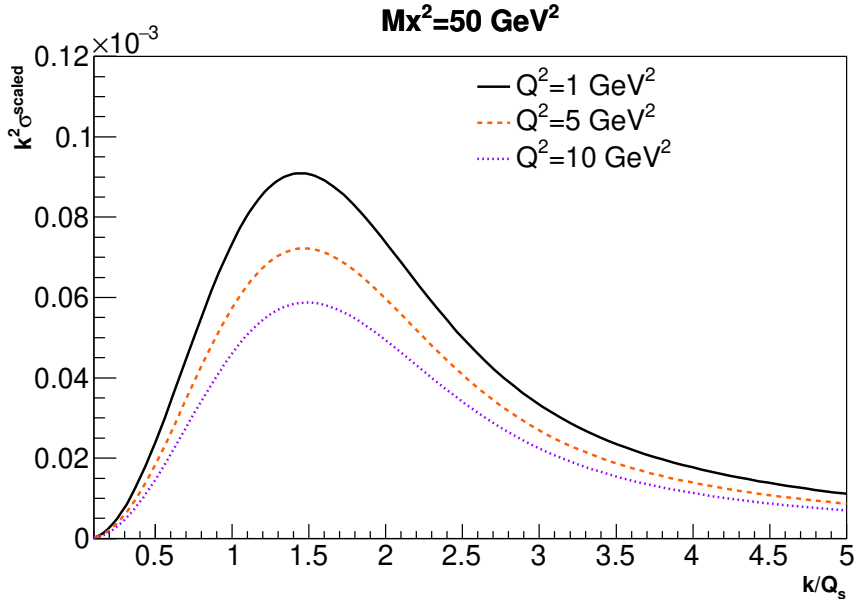

(a)

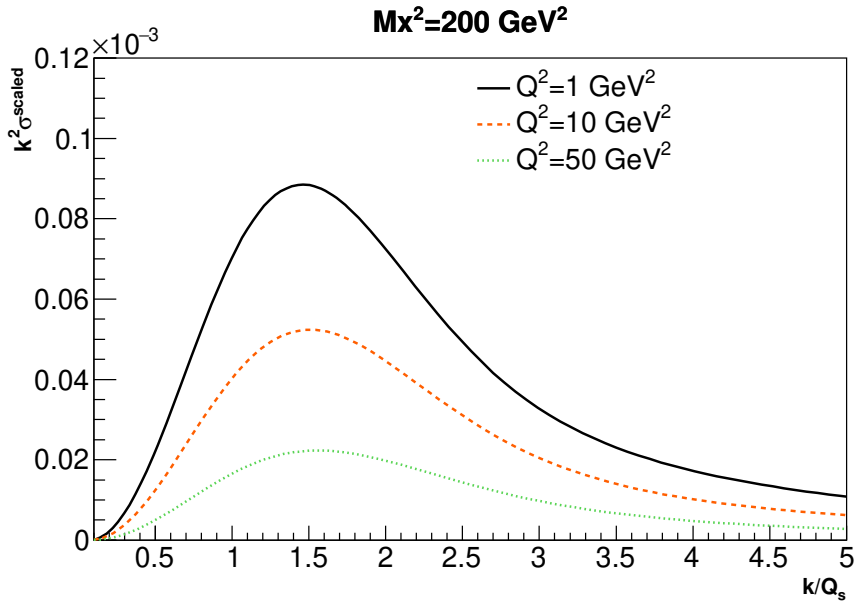

(b)

Figure 5.4 – Differential cross section $\kappa^2\sigma^{\text{scaled}}$ at the LHeC ($\sqrt{s} = 812$ GeV) as a function of $\tau = (\kappa/Q_s)$. The following configurations are shown: (a) for $M_X^2 = 50$ GeV^2 with $Q^2 = 1$, 5, 10 GeV^2 and (b) for $M_X^2 = 200$ GeV^2 with $Q^2 = 1$, 10, 50 GeV^2 . The peak occurs around $\tau_A \approx 1.5$.

Hereafter we start to numerically evaluate the formula for the gluon jet differential cross section, Eqs. (5.5) and (5.11), using the nuclear saturation scale based on geometric scaling property, Eq. (5.12). We perform our analysis for diffraction in eA collisions focusing only on coherent diffraction, $e + A \to e + X + A$, where the incident nucleus remains intact in the final state. Incoherent diffraction, $e + A \to e + X + A^*$, which dominates for large-$|t|$ is out of scope of the present study. We summarize in Table 5.1 the investigated

Table 5.1 – The design center-of-mass energy (in unities of GeV) for electron-nucleus collisions in the machines EIC, LHeC, high energy upgrade of LHeC (HE-LHeC) and FCC-eA, respectively.

Collider	E_e	E_A	$\sqrt{s}$
EIC	21	100	92
LHeC	60	2760	812
HE-LHeC	60	4930	1088
FCC-eA	60	19700	2174

energy configurations (in units of GeV) of planned electron-ion colliders, where $\sqrt{s}$ is the center-of-mass collision energy per nucleon and $xys = Q^2$ (y is the inelasticity variable).

We start the analysis for the EIC presenting the scaled cross section as a function of jet transverse momentum, κ. For a gold nucleus, in Fig. 5.3 the results are shown for the scaled cross section, Eq. (5.11), in the following two kinematic configurations: $Q^2 = 1$ GeV^2 and $M_X^2 = 5$ GeV^2 (solid line) and $Q^2 = 5$ GeV^2 and $M_X^2 = 25$ GeV^2 (dashed line). These values correspond to ($\beta \simeq 0.17$, $x_{I\!P} \simeq 7.0 \times 10^{-4}$) and ($\beta \simeq 0.17$, $x_{I\!P} \simeq 3.5 \times 10^{-3}$), respectively. The rapidity gap is $\Delta\eta \approx 3$ and the more prominent feature is the plateau for $\kappa \lesssim 1$ GeV. This feature is also observed in ep case [98] and explained by the fact that the differential cross section $\kappa^2 d\sigma/d^2k_\perp dM_X$ rises as κ^2 for small transverse momentum as referred already. This happens independently of the particular model for the S-matrices. On the other hand, at relative large κ the cross section falls as $1/\kappa^4$ and the transition region is driven by the nuclear saturation scale, $Q^2_{s,Au}(x_{I\!P} \sim 10^{-3}) \approx 1.3$ GeV^2. By using $\sigma_A \simeq 267$ fm^2 and $\alpha_s = 0.2$ we estimate the following values for the differential cross section at $\kappa = 10$ GeV:

$$
\begin{aligned}
M_X \frac{d\sigma_{\rm diff}}{d^2k_\perp dM_X} &\approx 8\,\frac{nb}{GeV^2},\, Q^2 = 1\,GeV^2, M_X^2 = 5\,GeV^2, \\
M_X \frac{d\sigma_{\rm diff}}{d^2k_\perp dM_X} &\approx 17\,\frac{nb}{GeV^2},\, Q^2 = 5\,GeV^2, M_X^2 = 25\,GeV^2 \quad .
\end{aligned}
$$

We now turn to the LHeC in its heavy-ion mode [119], which would scatter electrons with $E_e = 60$ GeV on a beam of nuclei from the LHC, with $E_A = 2.75$ TeV per nucleon resulting in $\sqrt{s} = 812$ GeV per nucleon. The corresponding integrated luminosity could reach 10 fb^{-1}, being 10× bigger than the full integrated luminosity achieved in ep collisions at DESY-HERA. Due to the high luminosity, the LHeC or equivalent high energy machine opens the opportunity to directly measure the nuclear saturation scale as a function of

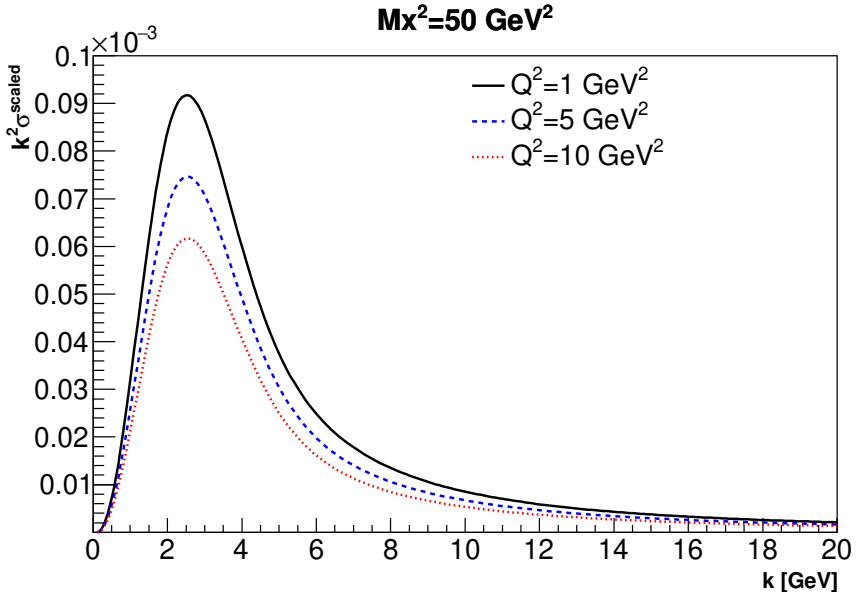

(a)

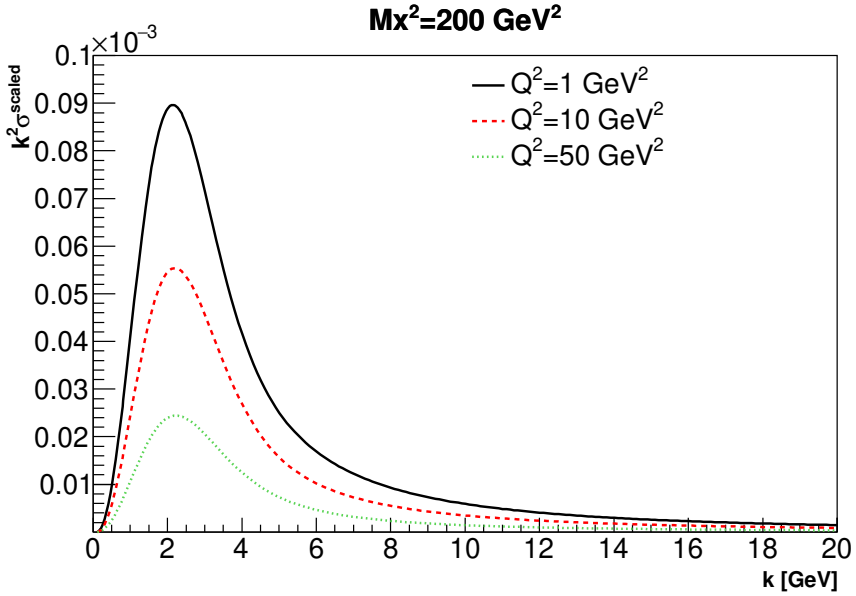

(b)

Figure 5.5 – Differential cross section $\kappa^2\sigma^{\text{scaled}}$ at the HE-LHeC ($\sqrt{s} = 1.088$ TeV) as a function of κ. Three configurations are shown: $M_X^2 = 50$ GeV^2 with $Q^2 = 1$, 5, 10 GeV^2 and $M_X^2 = 200$ GeV^2 with $Q^2 = 1$, 10, 50 GeV^2 .

$x_{I\!P}$ as firstly proposed in [98]. Specifically, whether the cross section $\kappa^2 d\sigma/d^2k_\perp dM_X$ can be measured as a function of κ for distinct values of $x_{I\!P}$, the positions of its maximum is translated into the $x_{I\!P}$-dependence of saturation scale. Using the same reasoning, the absolute value of $Q_{s,A}$ could be determined by considering a wide interval of Q^2 in the limit $\beta \ll 1$. The property is shown in Fig. 5.4, where the cross section $\kappa^2\ \sigma^{\text{scaled}}(\kappa, Q^2, Q^2_{s,Pb})$ is presented as a function of the jet transverse momentum scaled by the nuclear saturation scale, $k/Q_{s,A}(x_{I\!P})$. To quantify the dependence of the position of the bump, we plot the

cross section for 3 distinct values of photon virtuality and it can be clearly seen that the location of the bumps do not depend on Q^2 at all. It is straightforward to notice the marked bumps that separate the saturation region from the linear one. The numerical results are for (a) $M_X^2 = 50$ GeV^2 at virtualities $Q^2 = 1$ GeV^2 (solid line), $Q^2 = 5$ GeV^2 (dashed line) and $Q^2 = 10$ GeV^2 (dotted line) as well as for (b) $M_X^2 = 200$ GeV^2 at virtualities $Q^2 = 1$ GeV^2 (solid line), $Q^2 = 10$ GeV^2 (dashed line) and $Q^2 = 50$ GeV^2 (dotted line). These choices are based on the kinematic phase space for inclusive diffraction in $(x = \beta x_{I\!P}, Q^2)$ for the LHeC presented in Ref. [120]. The location of the bump is strongly related to the value of the saturation scale and to the model we are using, Eq. (5.12), and the coefficient of proportionality between $(k_\perp)_{max}$ and $Q_{s,A}(x_{I\!P})$ is equal to $\kappa_{max}/Q_s \approx 1.5$ (we checked this is the case for any energy even at very low-$x_{I\!P}$). That means the dimensionless cross section as a function of a scaling variable, $\tau_A = \kappa/Q_{s,A}$, is universal. Just to exemplify quantitatively the value of the nuclear saturation scale in the domain considered above, one has $Q^2_{s,Pb} \approx 2.6$ GeV^2 (for $Q^2 = 1$ GeV^2 and $M_X^2 = 50$ GeV^2) and $Q^2_{s,Pb} \approx 1.7$ GeV^2 (for $Q^2 = 50$ GeV^2 and $M_X^2 = 200$ GeV^2), which are a factor 2 higher than in EIC case. This is translated into the jet transverse momentum at the peak, i.e., $(\kappa)_{max} \simeq 2.4$ GeV and $(\kappa)_{max} \simeq 2$ GeV, respectively.

Now we analyze the higher-energy upgrade of the LHeC (HE-LHeC) [119, 121] . The HE-LHC (High-Energy Large Hadron Collider) is a future energy upgrade of the LHC and its heavy-ion mode considers a beam of nuclei with $E_A \simeq 4.9$ TeV per nucleon resulting in $\sqrt{s} \simeq 1.1$ TeV per nucleon. The expected luminosity is $\mathcal{L} = 18 \times 10^{32}$ cm^{-2}s^{-1}. In Fig. 5.5, the cross section $\kappa^2\sigma^{\rm scaled}(\kappa, Q^2, Q_{s,A})$ is plotted as a function of transverse momentum. We present the numerical results taking into account the same configuration as in the previous figure in terms of the jet momentum. The general behavior remains the same, however the nuclear saturation scale has increased up to $Q^2_{s,Pb} \approx 3$ GeV^2 and $Q^2_{s,Pb} \approx 2$ GeV^2 in the bins (Q^2, M_X^2) we had discussed before for the LHeC. The shift on the location of the peak is now seen, where the maximum occurs for larger κ in (a) compared to (b) due to the smaller $x_{I\!P}$ value in that configuration. Accordingly, for the HE-LHeC the relation $(\kappa)_{max} \approx 1.5\ Q_{s,A}$ still remains. As an example of numerical value of the cross section, $M_X d\sigma/d^2k_\perp dM_X \approx 7.4$ mb/GeV^2 at the peak for $Q^2 = 1$ GeV^2 and $M_X^2 = 200$ GeV^2.

Finally, we discuss eA collisions at the FCC-eA [119, 121] machine that would be performed with a lead beam with energy per nucleon of $E_A = 19.7$ TeV, which would give

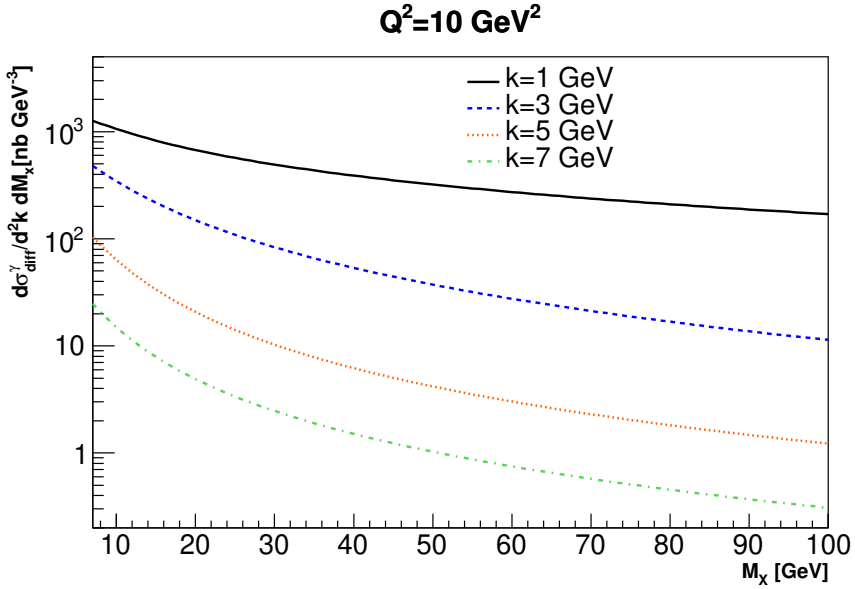

(a)

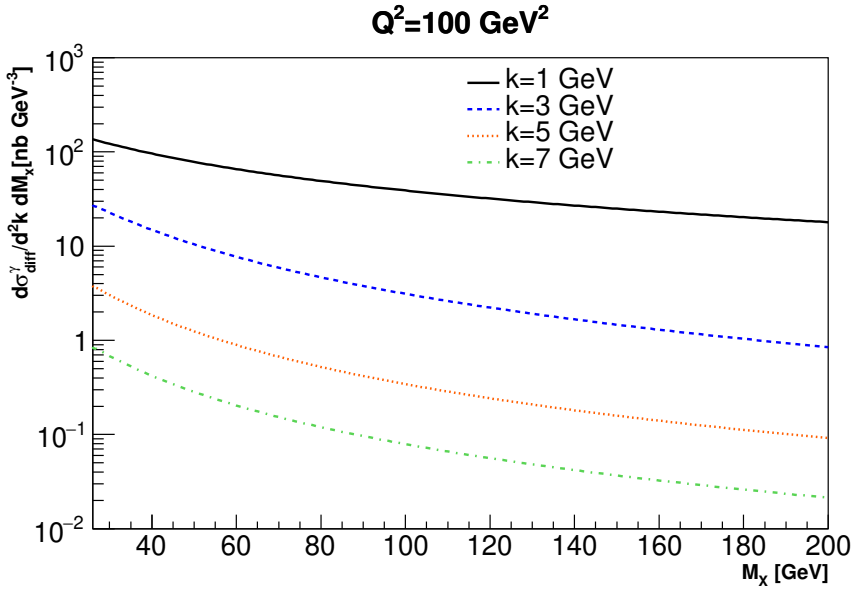

(b)

Figure 5.6 – Differential cross section $d\sigma_{\rm diff}/d^2k_\perp dM_X$ as a function of diffractive mass M_X for fixed Q^2 and κ at the FCC-eA ($\sqrt{s} = 2.174$ TeV). Two configurations are presented: (a) $Q^2 = 10$ GeV^2 and (b) $Q^2 = 50$ GeV^2. The jet transverse momentum increases in the curves from top to bottom.

$\sqrt{s} \simeq 2.2$ TeV per nucleon with expected luminosity of $\mathcal{L} = 54{\times}10^{32}$ cm^{-2}s^{-1}. This is in the context of a Future Circular Collider - hadron-hadron mode (FCC-hh) that would provide pp collisions with $\sqrt{s} = 100$ TeV. In Fig. 5.6, the differential cross section $d\sigma/d^2k_\perp dM_X$ is presented as a function of M_X for (a) $Q^2 = 10$ GeV^2 (for fixed $\kappa = 1,\ 3,\ 5,\ 7$ GeV) and (b) $Q^2 = 100$ GeV^2 (for fixed $\kappa = 1,\ 3,\ 5,\ 7$ GeV). In this figure, the jet transverse momentum increased in the curves from top to bottom in panels (a) and (b). In Fig. 5.7, we summarize the behavior of the scaled cross section times κ^2 for every collider in terms

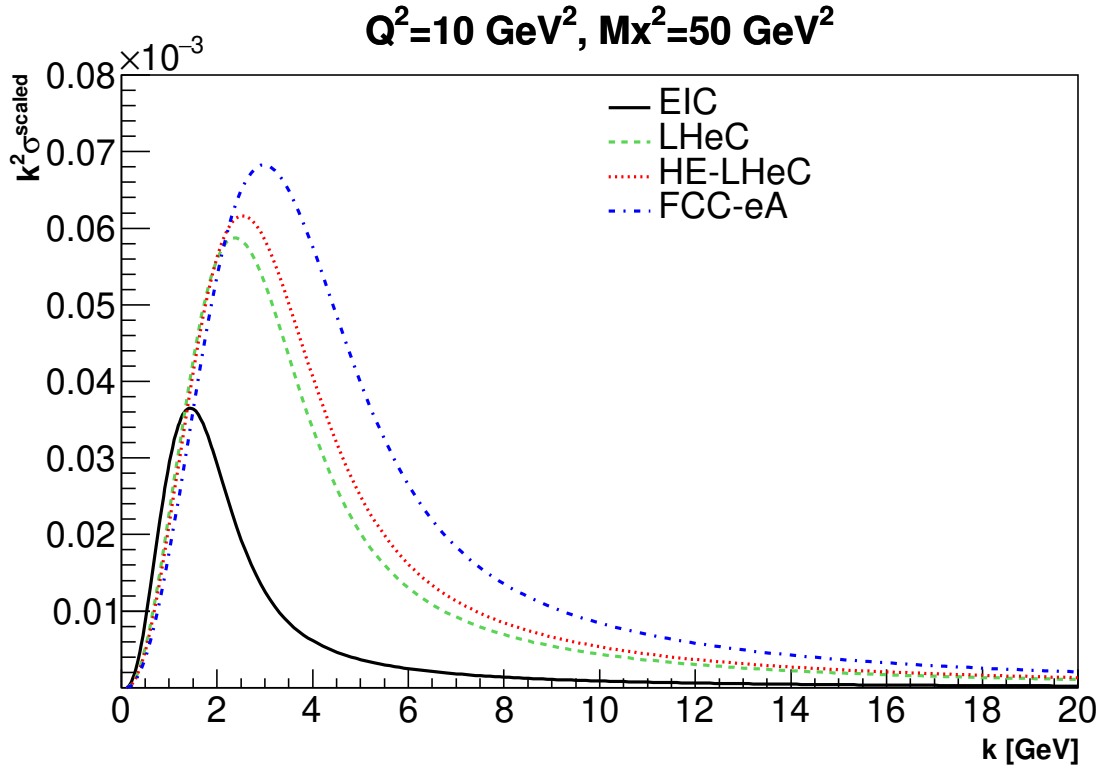

Figure 5.7 – The universal quantity $\kappa\sigma^{\text{scaled}}$ as a function of jet transverse momentum for EIC, LHeC, HE-LHeC and FCC-eA machines for the sample configuration ($Q^2 = 10$ GeV^2, $M_X^2 = 50$ GeV^2). The displacement on the peak is proportional to the increasing nuclear saturation scale.

of the jet momentum for the sample configuration $Q^2 = 10$ GeV^2 and $M_X^2 = 50$ GeV^2. The shift on the peak location is clearly seen, which is explained by the increasing of the nuclear saturation scale, $Q_{s,A}^2 \approx 3(x_0/x_{I\!P})^{0.25}$ GeV^2, where $x_{I\!P} \approx M_X^2/W_{\gamma p}^2$ in the region $\beta \ll 1$. All the findings we have discussed in eA collisions should remain in ep mode, where it is expected energies of order $\sqrt{s} = 1 - 4$ TeV with luminosities $\mathcal{L} \simeq 10^{34}$ cm^{-2}s^{-1}. Particularly, ep collisions at the LHeC can explore very low values of β and a new domain of diffractive masses compared to DESY-HERA (M_X can include W/Z/beauty or any state with 1^- quantum number).

5.2 Timelike Compton scattering

Timelike Compton scattering (TCS) has been recently investigated in Ref. [122] in the context of the k_T–factorization formalism. There, dilepton production was considered within a large range of dilepton invariant masses for the cases of electron-proton and proton-proton collisions. The calculation was based on Refs. [123, 124], where the process

was studied for the first time. Here, the aim is to extend that analysis considering nuclei as targets rather than protons. One interesting process is the electron-nucleus collision. As already mentioned, it is planned to be investigated at the EIC [2] and at the LHeC [97]. Photonuclear reactions can be also studied in ultraperipheral heavy ion collisions [125, 126] and it would be timely to analyze TCS in electromagnetic processes for large impact parameter proton-nucleus and nucleus-nucleus collisions.

Dilepton production can occur through several mechanisms, being the leading one the ordinary Drell-Yan process. The second most important contribution comes from photon fusion, i.e., $\gamma\gamma \to \ell^+\ell^-$, which is used for controlling the luminosity at the LHC. In addition, single and double diffractive Drell-Yan also produce dileptons via different interactions, such as Pomeron - Pomeron ($I\!P I\!P$), Pomeron - Reggeon ($I\!P I\!R$), Reggeon - Reggeon ($I\!R I\!R$), Pomeron - proton ($I\!P p$) and Reggeon - proton ($I\!R p$) reactions [124, 127]. We can still have the reactions $\gamma I\!P$ and $I\!P\gamma$, where the underlying process is TCS. At last, it should be stressed out that the Bethe-Heitler (BH) mechanism contributes at the amplitude level to the physical process of photoproduction of heavy lepton pairs, and it is known that the BH contribution (and its interference with TCS) is large in contrast to timelike Compton scattering itself.

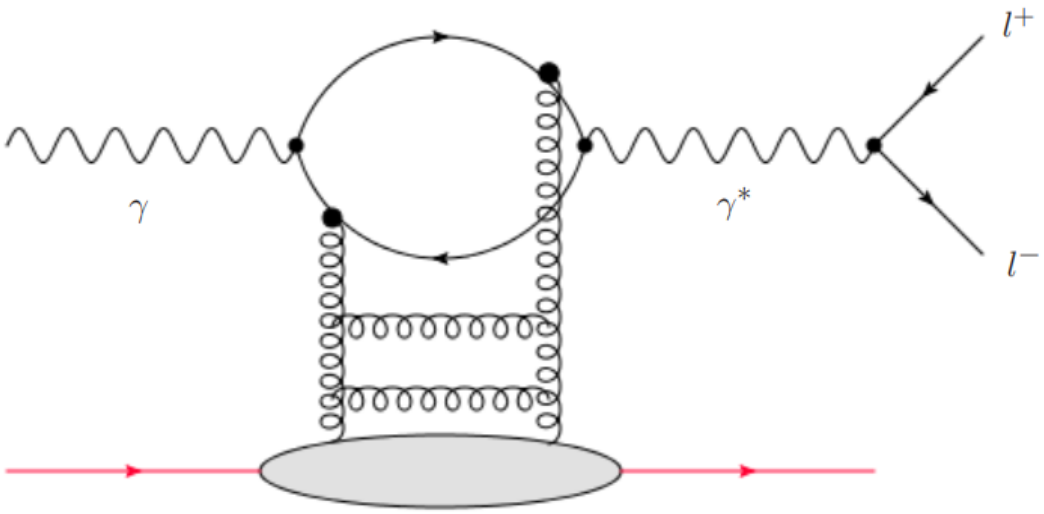

Figure 5.8 – Timelike Compton scattering. The red line represents a nucleus.

Studies on TCS have been often performed within the formalism of Generalized Parton Distributions (GPDs) [128–130] (see also, for example, Refs. [131–133]). One of the goals in the study of these distributions is to understand how quarks and gluons

assemble themselves to hadrons [134–137]. Since the cleanest reactions to obtain the GPDs are the DVCS (deeply virtual Compton scattering) and TCS, studying the latter through distinct reactions could be relevant for their determination. For example, TCS amplitudes and related observables have been recently looked into using leading-twist approximation [138] in the GPD approach. In addition, investigations have been carried out in order to lower the intrinsic model dependence. In Ref. [139], dilepton production through the TCS process was addressed in the context of ultraperipheral collisions (UPCs) at a fixed-target experiment (AFTER@LHC), which was executed utilizing the nucleon and ion beams.

Timelike Compton scattering is the "opposite"process of deeply virtual Compton scattering (DVCS) in the sense that in TCS one has, at the final state, a virtual photon $\gamma p(A) \to \gamma^* p(A)$, whereas in DVCS there is a real photon, $\gamma^* p(A) \to \gamma p(A)$. The former has been carefully studied in Refs. [140,141] for nuclear targets within the dipole formalism in the case of coherent scattering. The referred works were based on a previous paper concerning nuclear DVCS [142] and considered the spacelike approximation. Predictions were presented for electron-ion collisions based on geometric scaling arguments. In Ref. [143] it was verified that in order to calculate the TCS cross section, one needs to deal with a strongly oscillatory integrand in the color dipole approach. To resolve this issue, it is necessary to make use of an analytic continuation of the integrand on the dipole size, r, and integrate it in the complex plane. Such procedure brought numerical difficulties for the calculations. These shortcomings do not appear in the momentum space and this is one of reasons to employ it here.

This study is complementary to our previous study on electron-proton and proton-proton collisions. To adapt our treatment performed in [122] to nuclei targets, we replace the proton UGD by the nuclear one, applying the Glauber-Mueller formalism [144, 145] to introduce the nuclear effects. The goal here is to examine TCS in nuclear targets for the first time in the k_T-factorization approach (see Fig. 5.8). In addition, it opens the possibility of carrying out a detailed study on the role played by the nonlinear QCD effects as the saturation scale is enhanced in nuclei in comparison with proton targets [22].

The main goal is to investigate the nuclear effects in nuclear TCS, focusing on the atomic mass number (A) dependence. As in Ref. [122], we compute the cross section in terms of the dilepton invariant mass and rapidity at the center-of-mass energies of current and future machines for different nuclei. We are aware about the limitation on the use of

factorization in nuclear collisions. In Refs. [146–149] the validity of k_T-factorization for nuclear reactions was investigated and it was shown that linear k_T-factorization is broken in nuclear processes. In this context, it should be stressed out that this is an exploratory study and further investigations should be carried out.

In the k_T-factorization the main ingredient is the UGD. Before presenting the TCS amplitude and cross section, in next paragraphs we briefly discuss and motivate the phenomenological model considered in the calculations: the Moriggi-Peccini-Machado (MPM) model [92].

As aforementioned, the TCS process for ep and pp collisions has been previously calculated in detail in Ref. [122]. The aim here is to extend that analysis to the case of nuclear targets. Within the k_T-factorization formalism, one can compute the nuclear TCS cross section by considering a nuclear UGD instead of the proton one. There are quite a few phenomenological models for the nuclear UGD [115, 150–153]. On the other hand, it was also demonstrated [122] that distinct UGDs present practically the same results in the kinematical region we are taking into consideration. Thereby, we will focus on the MPM model, which was previously proposed by the authors in [92].

Concisely presenting this model (see Ref. [92] for details), it is based on geometric scaling framework and defines an expression for the gluon unintegrated function that depends on the variable τ, being $\tau = k_T^2/Q_s^2$, where k_T^2 is the transverse momentum squared of the gluons and Q_s^2 is the saturation scale. Alongside the quantity τ, the MPM contains also three other parameters. The distribution is given by

$$\phi_{\rm MPM}(x, k_T^2) = \frac{3\sigma_0}{4\pi^2\alpha_s}\frac{(1+\delta n)}{Q_s^2}\frac{k_T^2}{(1+\frac{k_T^2}{Q_s^2})^{2+\delta n}} \ , \tag{5.13}$$

in which $\delta n = a\tau^b$ and $Q_s^2 = (x_0/x)^{0.33}$. In the expression above, σ_0, x_0, a and b were fitted against DIS data in the kinematic domain $x < 0.01$. Beside describing DIS data at small-x, it also drives the spectra of produced hadrons in $pp/p\bar{p}$ processes. This model was built by means of the geometric scaling approach and a Tsallis-like behavior of the measured spectra. Additionally, the strong coupling constant does not depend on the scale μ and thus the value $\alpha_s = 0.2$ is used.

The plan here is to adapt the MPM expression of the proton target, Eq. (5.13), to the case of nuclear targets, and this can be conveniently performed by applying the technique utilized in [115], where the GBW UGD is extended to nuclei by using the

Glauber–Mueller formalism. Following [115], the dipole scattering matrix in position space, r, is determined through the cross section for dipole-proton scattering:

$$S_{dA}(x,r,b) = \mathrm{e}^{-\frac{1}{2}T_A(b)\sigma_{dp}(x,r)} \ . \tag{5.14}$$

The function $T_A(b)$ is the thickness function and depends on the impact parameter, b. Similarly to [115], we will assume a Woods–Saxon-like parametrization for the nuclear density [154] (except for Li, for which the nuclear density will be taken as a Gaussian distribution) whose normalization is $\int d^2bT_A(b) = A$. Thus, the nuclear UGD is written in the following way:

$$\phi_A(x,k_T^2,b) = \frac{3}{4\pi^2\alpha_s}k_T^2\nabla_{k_T}^2\mathcal{H}_0\left\{\frac{1-S_{dA}(x,r,b)}{r^2}\right\} \ , \tag{5.15}$$

where $\mathcal{H}_0\left\{f(r)\right\} = \int dr\, rJ_0(k_T r)f(r)$ is the order zero Hankel transform.

Regarding the proton target, a homogeneous object with radius R_p is considered, which factorizes $S_{dp}(x,r,b)$ into $S_{dp}(x,r,b) = S_{dp}(x,r)\Theta(R_p - b)$. For large dipoles, $S_{dp}(x,r) \to 0$, and the cross section reaches a bound given by $\sigma_0 = 2\pi R_p^2$. In the saturation approach, the gluon distribution presents a maximum at $k_T \simeq Q_s(x)$. This formalism is characterized by geometric scaling, what implies that observables become dependent on the ratio $Q^2/Q_s^2(x)$ instead of Q^2 and x separately.

The dipole cross section in coordinate space r may be evaluated as [92]

$$\sigma_{dp}(\tau_r) = \sigma_0\left(1 - \frac{2(\frac{\tau_r}{2})^\xi K_\xi(\tau_r)}{\Gamma(\xi)}\right) \ , \tag{5.16}$$

where $\xi = 1 + \delta n$ and $\tau_r = rQ_s(x)$ is the scaling variable in the position space. Accordingly, the nuclear gluon distribution is obtained from Eqs. (5.14) and (5.15).

At this point, some considerations are in order. The shadowing of structure functions observed in nuclear DIS in the region of small-x is viewed in the saturation formalism/CGC as the multiple scattering of the photon fluctuations in the nuclear target, giving rise to the modification of nuclear UGD compared to that of free nucleons. It is well known that this effect is enhanced as the atomic mass number, A, increases [155]. Here, we investigate the A-dependence of the cross section for diffractive production of dileptons at current and future colliders (HL-LHC/LHeC, HE-LHC/HE-LHeC and FCC-eA/pA(AA)). At high energies the small-x regime is reached, $x \sim M^2/W^2 \lesssim 10^{-6}$, where it is expected a significant suppression of this observable relative to the ep case. The nuclear structure functions at small-x were constrained experimentally by E665 and NMC collaborations for

the nuclei Li, C, Ca, Sn and Pb [36, 37, 155, 156]. In our analysis, we utilize these nuclei as representative targets and carry out predictions for nuclear TCS. Hereafter, the expression for TCS amplitude is reviewed and the photonuclear case is also discussed.

In what follows, we will expose the main expressions in [122] about TCS in electron-proton collisions (the reader may obtain a careful analysis in the quoted reference). Therein, it was shown that the imaginary part of the TCS amplitude is written as

$$\begin{aligned}\mathrm{Im}\mathcal{A}_f^{\mathrm{TCS}} = \frac{4\alpha_{em}e_f^2}{\pi}\Big[&\Theta(M^2_{\ell^+\ell^-}-4m_f^2)\\ &\times\big(\mathrm{PV}\int_{4m_f^2}^{\infty}\Omega(W^2,M^2_{q\bar{q}},M^2_{\ell^+\ell^-})\;dM^2_{q\bar{q}}\\ &+\pi\mathrm{Re}\mathcal{M}_f(W^2,M^2_{\ell^+\ell^-})\big)+\Theta(4m_f^2-M^2_{\ell^+\ell^-})\\ &\times\int_{4m_f^2}^{\infty}\Omega(W^2,M^2_{q\bar{q}},M^2_{\ell^+\ell^-})\;dM^2_{q\bar{q}}\Big]\;. \end{aligned} \tag{5.17}$$

Analogously, the real part is given by

$$\begin{aligned}\mathrm{Re}\mathcal{A}_f^{\mathrm{TCS}} = \frac{4\alpha_{em}e_f^2}{\pi}\Big[&\Theta(M^2_{\ell^+\ell^-}-4m_f^2)\\ &\times\big(\mathrm{PV}\int_{4m_f^2}^{\infty}\eta(W^2,M^2_{q\bar{q}},M^2_{\ell^+\ell^-})\;dM^2_{q\bar{q}}\\ &-\pi\mathrm{Im}\,\mathcal{M}_f(W^2,M^2_{\ell^+\ell^-})\big)+\Theta(4m_f^2-M^2_{\ell^+\ell^-})\\ &\times\int_{4m_f^2}^{\infty}\eta(W^2,M^2_{q\bar{q}},M^2_{\ell^+\ell^-})\;dM^2_{q\bar{q}}\Big]\;. \end{aligned} \tag{5.18}$$

The definitions of $\Omega(W^2, M^2_{q\bar{q}}, M^2_{\ell^+\ell^-})$ and $\eta(W^2, M^2_{q\bar{q}}, M^2_{\ell^+\ell^-})$ are the following:

$$\Omega(W^2,M^2_{q\bar{q}},M^2_{\ell^+\ell^-}) = \frac{\mathrm{Im}\mathcal{M}_f(W^2,M^2_{q\bar{q}})}{M^2_{q\bar{q}}-M^2_{\ell^+\ell^-}}\;, \tag{5.19}$$

$$\eta(W^2,M^2_{q\bar{q}},M^2_{\ell^+\ell^-}) = \frac{\mathrm{Re}\mathcal{M}_f(W^2,M^2_{q\bar{q}})}{M^2_{q\bar{q}}-M^2_{\ell^+\ell^-}}\;. \tag{5.20}$$

In the previous expressions, e_f is the quark charge of flavor f, while m_f is its mass. The quantities W, $M^2_{q\bar{q}}$ and $M^2_{\ell^+\ell^-}$ are the photon-nucleus center-of-mass energy, dipole invariant mass squared and dilepton invariant mass squared, respectively. For further details on the expressions, see Ref. [122].

Adopting the dipole picture, where the virtual photon fluctuates into a quark-antiquark pair, the spectral distribution in Eq. (5.17) that is related to the diffractive amplitude for the $\gamma A \to q\bar{q}A$ transition is given by

$$\begin{aligned}\mathrm{Im}\,\mathcal{M}_f(W^2,M^2_{q\bar{q}}) &= \frac{1}{\pi M^2_{q\bar{q}}}\int_0^{\kappa^2_{\max}}\frac{d^2\kappa}{\sqrt{1-4\left(\frac{\alpha}{M^2_{q\bar{q}}}\right)}}\\ &\times\;\mathrm{Im}\,M_f(W^2,\kappa^2,z)\;, \end{aligned} \tag{5.21}$$

where $\kappa^2_{\rm max} = (0.25M^2_{q\bar{q}} - m^2_f)$ and

$$\mathrm{Im}M_f(W^2,\kappa^2,z) = \int_0^\infty \frac{d^2k_\perp}{k^2_\perp}\phi_A(x,k^2_\perp)\alpha_s(\mu^2) \tag{5.22}$$

$$\times\big[C_{0f}(z,\kappa^2)D_{0f}(\kappa^2,k^2_\perp) + C_{1f}(z,\kappa^2)D_{1f}(\kappa^2,k^2_\perp)\big]\ . \tag{5.23}$$

The functions C_{0f}, D_{0f}, C_{1f} and D_{1f} are specified in [122]. Recalling the determination of $\mathrm{Re}M_f$, it is computed via the dispersion relation, $\rho = \mathrm{Re}\,M_f/\mathrm{Im}M_f$. The ρ parameter is defined as $\rho = \tan\left(\frac{\pi}{2}\lambda_{\rm eff}\right)$, in which $\lambda_{\rm eff} = \partial\ln(\mathrm{Im}M_f)/\partial\ln(W^2)$.

In order to embed a t dependence in the scattering amplitude, one needs to take into consideration the nuclear form factor. For simplicity and following Ref. [157], an analytical expression based on homogeneous hard sphere and the Yukawa approximation will be considered:

$$F(q) = \frac{4\pi\rho_0}{Aq^3}\big[\sin(qR_A) - qR_A\cos(qR_A)\big] \times\big[\frac{1}{1+r^2_0q^2}\big]\ , \tag{5.24}$$

where $q = \sqrt{|t|}$, $\rho_0 = A/(4/3\pi R^3_A)$ and $R_A = (1.12A^{1/3} - 0.86A^{-1/3})$. The parameter r_0 is the range of a Yukawa potential and its value is $r_0 = 0.7\,\mathrm{fm}$. Therefore, the amplitude depending on t is expressed as follows:

$$A^{\rm TCS}_f(W,t) = F(q)A^{\rm TCS}_f(W,t=0)\ . \tag{5.25}$$

The differential cross section for the $\gamma A \to \gamma^* A$ collision is then

$$\frac{d\sigma}{dt}(\gamma A\to\gamma^*A) = \frac{[\mathrm{Im}(A^{\rm TCS})]^2\left(1+\rho^2\right)}{16\pi}|F(q)|^2\ , \tag{5.26}$$

where $\mathrm{Im}A^{\rm TCS} = \sum \mathrm{Im}A^{\rm TCS}_f$, with the summation over quark flavour. The integrated cross section is given by

$$\sigma(\gamma A\to\gamma^*A) = \left.\frac{d\sigma}{dt}\right|_{t=0}\int_{-\infty}^{t_{min}}|F(q)|^2dt\ . \tag{5.27}$$

Having the TCS cross section, one may express the differential cross section in terms of the dilepton invariant mass distribution:

$$\frac{d\sigma(\gamma A\to\ell^+\ell^-A)}{dM^2_{\ell^+\ell^-}} = \frac{\alpha_{em}}{3\pi M^2_{\ell^+\ell^-}}\sigma^{\rm TCS}(\gamma A\to\gamma^*A)\ . \tag{5.28}$$

Photonuclear reactions can be also investigated in ultrarelativistic heavy ion collisions in the case of large impact parameter. The protons or heavy nuclei are then sources of quasi-real photons. For pA collisions, analogously to the pp case (see Ref. [122]), dilepton production through TCS is dominated by $\gamma I\!P + I\!P\gamma$ reactions at high energies (an analysis on ultraperipheral TCS is performed in Ref. [158]). Within the equivalent photon approximation (EPA), the differential cross section for the nuclear coherent scattering, $p + A \to p + \ell^+\ell^- + A$, in terms of dilepton invariant mass and rapidity reads as [139]

$$\begin{aligned}\frac{d\sigma^{pA}}{dM^2_{\ell^+\ell^-}dy_{\rm pair}} &= k_+\left[\frac{dN(k_+)}{dk_+}\right]_p\left[\frac{d\sigma^{\gamma A\to\ell^+\ell^- A}}{dM^2_{\ell^+\ell^-}}(W_+)\right] \\ &+ k_-\left[\frac{dN(k_-)}{dk_-}\right]_A\left[\frac{d\sigma^{\gamma p\to\ell^+\ell^- p}}{dM^2_{\ell^+\ell^-}}(W_-)\right] \ . \end{aligned} \tag{5.29}$$

In the expression above, k stands for the photon energy, $dN(k)/dk$ is the photon flux and y_{pair} is the rapidity of the lepton pair. The photon flux of the proton will be given by [159]

$$\begin{aligned}\left[\frac{dN(k)}{dk}\right]_p &= \frac{\alpha_{em}}{2\pi k}\left[1+\left(1-\frac{2k}{\sqrt{s}}\right)^2\right] \\ &\times\left(ln\ \chi - \frac{11}{6} + \frac{3}{\chi} - \frac{3}{2\chi^2} + \frac{1}{3\chi^3}\right) \ , \end{aligned} \tag{5.30}$$

in which $\chi = 1+(Q_0^2/Q_{min}^2)$ with $Q_0^2 = 0.71\ GeV^2$ and $Q_{min}^2 = k^2/\gamma_L^2$, where $\gamma_L = \sqrt{s}/2m_p$. For nuclei, the photon flux is written as follows [160]:

$$\begin{aligned}\left[\frac{dN(k)}{dk}\right]_A &= \frac{2Z^2\alpha_{em}}{\pi k}\Big[\Delta K_0(\Delta)K_1(\Delta) \\ &- \frac{\Delta^2}{2}\big(K_1^2(\Delta) - K_0^2(\Delta)\big)\Big] \ , \end{aligned} \tag{5.31}$$

where $\Delta = 2kR_A/\gamma_L$ in AA collisions and $\Delta \approx k(R_p + R_A)/\gamma_L$ for pA collisions.

The photon energy k and the center-of-mass energy W of the photon-nucleus (nucleon) can be written in terms of the dilepton rapidity and its invariant mass:

$$k_\pm = \frac{M_{\ell^+\ell^-}}{2}e^{\pm y_{\rm pair}}, \quad W_\pm^2 = 2k_\pm\sqrt{s} \ . \tag{5.32}$$

The expressions above relate the photon-proton center-of-mass energy to the proton-nucleus and nucleus-nucleus ones. In case of AA collisions, the differential cross section takes the following form:

$$\begin{aligned}\frac{d\sigma^{AA}}{dM^2_{\ell^+\ell^-}dy_{\rm pair}} &= k_+\left[\frac{dN(k_+)}{dk_+}\right]_A\left[\frac{d\sigma^{\gamma A\to\ell^+\ell^- A}}{dM^2_{\ell^+\ell^-}}(W_+)\right] \\ &+ k_-\left[\frac{dN(k_-)}{dk_-}\right]_A\left[\frac{d\sigma^{\gamma A\to\ell^+\ell^- A}}{dM^2_{\ell^+\ell^-}}(W_-)\right] \ . \end{aligned} \tag{5.33}$$

Collider	E_p	E_e
LHeC/HL-LHeC (TeV)	7	0.06
HE-LHeC (TeV)	13.5	0.06
FCC-eh (TeV)	50	0.06
HL-LHC (TeV)	7	-
HE-LHC (TeV)	13.5	-
FCC-hh (TeV)	50	-

Table 5.2 – Configurations of the projected beam energies for future high energy machines [121].

From now on we perform the numerical calculations for exclusive dilepton production in eA and p(A)A collisions.

The TCS cross section will be computed in terms of dilepton invariant masses and rapidity distributions for eA, pA and AA collisions in the kinematic domain of current and future colliders. Their design configurations are summarized in Table 5.2. Different nuclei are considered (light and heavy ones) in order to cover the wide range of the atomic mass number, A. In that sense, the observables will be evaluated for Li (Z=3, A=6), C (Z=6, A=12), Ca (Z=20, A=40), Sn (Z=50, A=118) and Pb (Z=82, A=208). The center-of-mass energies for each nuclear collision are estimated considering the energy of the proton beam for each machine. The energies of the proton and electron beams are based on the prospects in Ref. [121].

First, we present the results for the electron-ion mode. Fig. 5.9 shows the differential cross section (divided by A^2) for dilepton production using Eq. (5.28) at the energies and atomic mass numbers presented in Table 5.6. Namely, we present predictions for the future machine LHeC, using the high luminosity (HL) and high energy (HE) baseline parameters at the LHC. Also, the FCC in eA mode was taken into account. The typical monotonic decrease of cross section on the dilepton invariant mass appears and the low mass region is the dominant contribution. It is clearly seen that there is a small enhancement of the cross section at FCC energy relative to HL/HE-LHC. One realizes that there is a significant decrease of the cross section as A increases, which indicates the presence of suppression due to nuclear effects. In the absence of such effects, one expects that the cross section scales with A^2 since $\sigma(\gamma A \to \gamma^* A)$ depends on the gluon distribution squared and the form factor of Eq. (5.24) gives a nuclear slope which depends, roughly speaking, on $R_A^2 \sim A^{2/3}$. The nuclear shadowing content in the UGD should produce a decreasing of the integrated cross section in terms of A. One can parametrize the growth of the integrated

	LHeC/HL-LHeC (TeV)	HE-LHeC (TeV)	FCC-eA (TeV)
Pb	0.81	1.13	2.18
Sn	0.84	1.17	2.25
Ca	0.92	1.27	2.45
C	0.92	1.27	2.45
Li	0.92	1.27	2.45

Table 5.3 – Estimated center-of-mass energies (per nucleon) of future electron-ion machines given a nucleus beam.

cross section as a power law A^α (with $\alpha = 2 - 2/3 - \delta$), where the parameter δ results from the nuclear shadowing. In Fig. 5.10, we plotted the TCS integrated cross section for dilepton production as a function of the atomic mass number, A. Larger cross section occurs for the FCC - eA energy, as already expected. The lines represent a power law fit[1] A^α with $\alpha = 1.19$ and it seems energy independent. In that sense, the value of α is close to the expected one for weak absorption where it grows as $A^{4/3}$ ($\alpha \approx 1.33$). Such behavior is quite similar to the photonuclear production of heavy vector mesons as J/ψ in the context of vector meson dominance (VMD) and small absorption in the Glauber model calculation. On the other hand, for strong absorption the expected behavior would be the black disk scaling, $\sigma_{\gamma A} \sim A^{2/3}$. For light nuclei the cross section has magnitude of units of nb and for heavy ions it reaches $\sim 100\,\text{nb}$.

With regards to the predicted TCS integrated cross section for the upcoming EIC, we only considered Au (gold) nucleus at collision energy of $\sqrt{s} = 92$ GeV. The obtained value was 52.19 nb and the event rate per year, given the EIC luminosity ($L = 10^{33-34}$ $\text{cm}^{-2}\text{s}^{-1}$) [2], is predicted to be approximately 1.646×10^{10}.

Lastly, we also accounted for the current configurations of the LHC (Run 2). The TCS integrated cross sections for pp ($\sqrt{s} = 13$ TeV), pPb ($\sqrt{s} = 8.16$ TeV) and PbPb ($\sqrt{s} = 5.02$ TeV) are 106 pb, 151 nb and 48 μb, respectively. The corresponding event rates per year, assuming the LHC Run 2 luminosity ($L = 10^{34}$ cm^{-2} s^{-1}) [161] are the following: 3.343×10^7, 4.762×10^{10} and 1.514×10^{13}.

The results for eA collisions can be directly compared to the predictions using the color dipole picture. In Ref. [140] the nuclear TCS cross section has been evaluated. In particular, it was considered a lead nucleus and two models for the dipole-nucleus cross section: the Marquet-Peschanski-Soyez (MPS) [162] and b-SAT [163] models. It was

[1] Although the proton is also displayed in Fig. 5.10, it is not being considered for the fit.

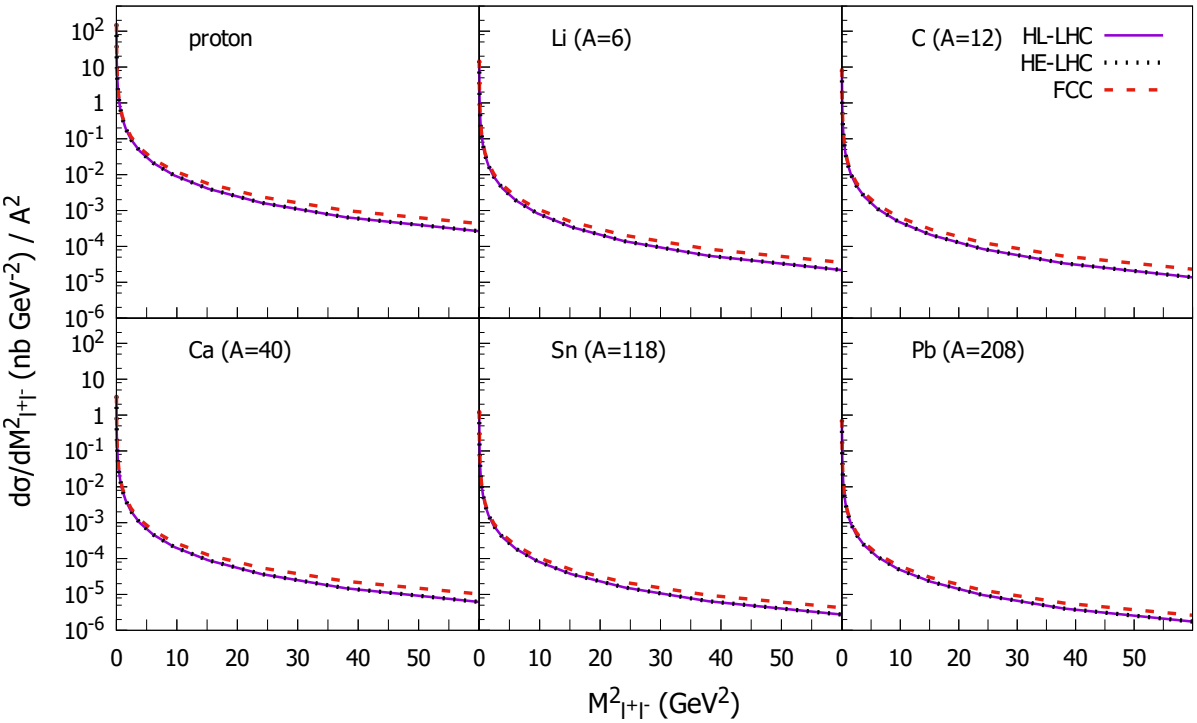

Figure 5.9 – Differential cross section for dilepton production as a function of dilepton invariant mass in eA collisions calculated through Eq. (5.28) for different nuclei at the energies described in Table 5.6.

	HL-LHC [TeV]	HE-LHC [TeV]	FCC-pA (AA) [TeV]
Pb	8.79 (5.52)	16.95 (10.64)	62.79 (39.42)
Sn	9.11 (5.93)	17.58 (11.44)	65.09 (42.37)
Ca	9.90 (7.00)	19.09 (13.50)	70.71 (50.00)
C	9.90 (7.00)	19.09 (13.50)	70.71 (50.00)
Li	9.90 (7.00)	19.09 (13.50)	70.71 (50.00)

Table 5.4 – Estimated center-of-mass energies (per nucleon) of pA (AA) collisions at the HL-LHC, HE-LHC and FCC-pA (AA) given a nucleus beam.

obtained $\sigma^{\rm TCS} \simeq 15$ nb (22 nb) at the LHeC energy (W ≈ 800 GeV), $\sigma^{\rm TCS} \simeq 19$ nb (23 nb) at the HE-LHeC energy (W ≈ 1200 GeV) and $\sigma^{\rm TCS} \simeq 22$ nb (25 nb) at the FCC-eA energy (W $\approx 2200\,$GeV), using the MPS (b-Sat) model, respectively. These values are consistent with ours for $A = 208$ (see Fig. 5.10). There, the integrated TCS cross section considers $M^2_{\ell^+\ell^-} \geq 2.25\,{\rm GeV}^2$, whereas in our work the lower bound of the integral was taken as $M^2_{\ell^+\ell^-} = 1\,{\rm GeV}^2$, thus the results in [140] should be smaller than ours. In addition, in Ref. [140] a spacelike approximation has been considered which provides cross sections smaller than the correct timelike kinematics (see discussion in Refs. [123, 143]).

We now turn to the ultraperipheral heavy ion collisions. The collision energies taken into consideration are outlined in Table 5.4. In Fig. 5.11, the dilepton rapidity

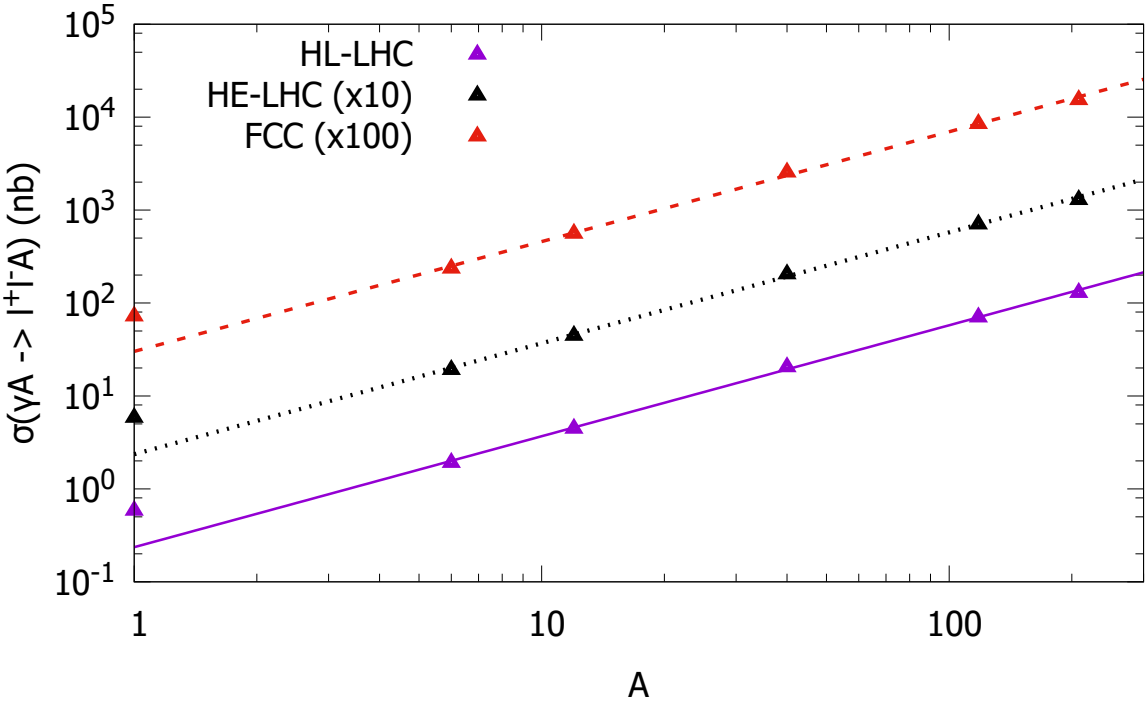

Figure 5.10 – Integrated cross section in eA collisions as a function of the atomic mass number. Each line is a power-like fit, A^{α}, with $\alpha = 1.19$.

distribution is shown for $y = 0$. Due to $Z^2 \sim A^2$, the leading small Δ (equivalently, small k) contribution in Eq. (5.31) and the fact that we obtained $\sigma(\gamma A \to \ell^+\ell^- A)$ scaling with A as $\sigma(\gamma A \to \ell^+\ell^- A) \sim A^{1.19}$, roughly one should have $d\sigma_{AA}/dy \sim A^{3.19}$. Despite the approximations, we got $d\sigma_{AA}/dy \sim A^{\beta}$ (with $\beta = 2.9$), which is close to the theoretical expected value. Concerning the typical order of magnitude, for lead one reaches dozens of μb at midrapidities. This is translated into a event rate for TCS channel of $\sim 10^5$ Hz at the HL-LHC.

The separation of different channels for the dilepton production in pp case involves the investigation of correlations for the outgoing particles, as the transverse momenta of final state protons or outgoing muons. Correlations in the rapidity space for outgoing leptons can be also considered. It was shown in [124] that correlations for the (single, double) diffractive mechanism are more intense than that for the two photon fusion, and the exclusive dilepton (TCS) production has same order of magnitude than the central diffractive one. The same selection can be considered in pA or AA collisions. The low-p_T region is of great interest and in Ref. [164] a careful study has been done in this kinematic domain. It includes the initial contributions due to the incoming photons, the soft photon radiations expressed in a Sudakov resummation, the multiple interactions between the

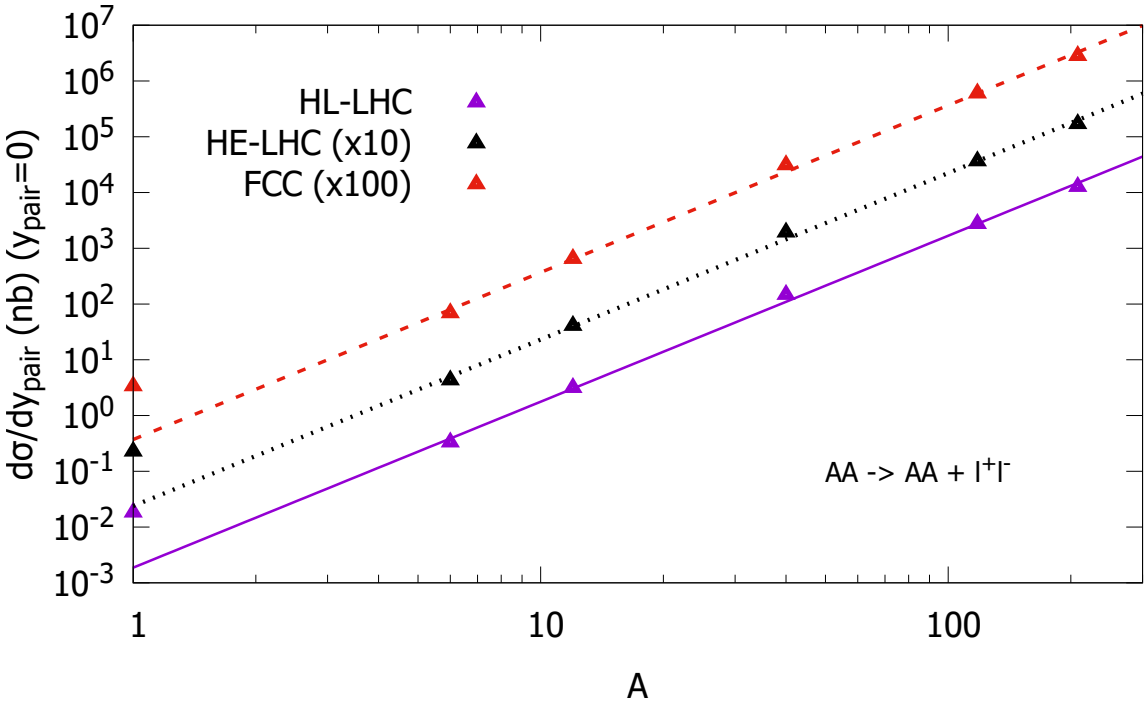

Figure 5.11 – Cross section for AA collisions, $d\sigma/dy_{pair}(AA)$, at $y_{pair} = 0$ as a function of the atomic mass number. Each line is a power-like fit, A^{β}, with $\beta = 2.9$.

lepton pairs and the electric charges inside the QGP and the effects of an external magnetic field.

In Fig. 5.12, the rapidity distribution is shown for pp, pPb and PbPb collisions. The cross sections considerably increase for higher energies. As expected, the pPb case has an asymmetric rapidity distribution, contrary to pp and PbPb collisions. In Table 5.8, numerical estimates for the integrated TCS total cross section are presented for these three collision modes. The values slightly differ from one machine configuration to another. The results for pp are quite similar to those ones presented in our previous work [122], where the theoretical uncertainty coming from the choice of the UGD has been discussed. For PbPb collisions, the TCS channel can be compared with the exclusive production of dilepton from two photon fusion. Recently, in Ref. [165] this channel has been analyzed for the energy of $\sqrt{s_{NN}} = 5.02$ TeV at the LHC and it was found $d\sigma/dy(y = 0) \simeq 250 - 300$ mb without any cut (the band corresponds to different treatments for the photon luminosity). Afterwards, in Ref. [166] the background associated with the diffractive production was investigated and it has been shown that such a channel is strongly suppressed. A new analysis for the exclusive dilepton production in $\gamma\gamma$ reaction in UPCs has been presented in Ref. [167], where the differential cross section is computed using the complete photon's

	HL-LHC	HE-LHC	FCC-hh
pp	0.110 (nb)	0.137 (nb)	0.206 (nb)
pPb	0.155 (μb)	0.228 (μb)	0.360 (μb)
PbPb	0.0500 (mb)	0.0787 (mb)	0.1335 (mb)

Table 5.5 – Integrated cross sections for pp, pPb and PbPb collisions at different configurations at the LHC (*pp* and heavy ion modes).

polarization density matrix resulting from the Wigner distribution framework. The authors claim that the approach provides much better agreement with experimental data than other approaches available in the literature. In the proton-lead collisions, the prediction can be compared to the recent analysis in Ref. [168] where a new experimental method to probe the photon PDF inside the proton at the LHC has been proposed. Interestingly, an unintegrated photon distribution (photon UGD) was considered and it was shown that due to the smearing of dilepton p_T introduced by the k_T-factorization formalism, the cross section is about 1/3 higher than the expected from usual collinear factorization. It would be timely to impose the same cuts in order to understand the background coming from the TCS process.

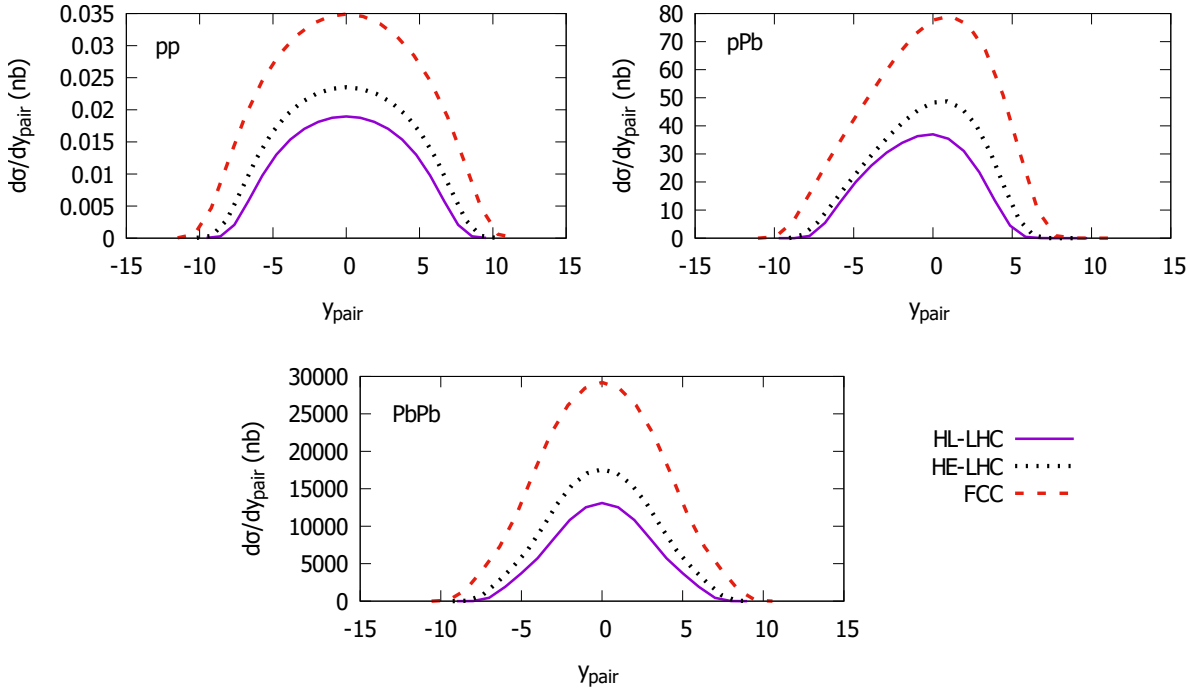

Figure 5.12 – Predictions for rapidity distributions in pp, pPb and PbPb collisions at the energies of the considered colliders.

Finally, concerning the predicted breaking of k_T-factorization mentioned already, some discussion is needed. The factorization theorems in perturbative QCD (pQCD) have the fundamental point that hard scattering cross sections are linear functionals of the suitable parton distributions in the projectile and target [148]. In [146] a remarkable breaking of linear k_T-factorization was verified in forward dijet production in DIS off nuclei. Afterwards, this fact confirmed to be true in case of single-jet spectra in hadron-nucleus collisions [147]. In [148], authors argued that dijet spectra and single-jet spectra in hadron-nucleus collisions clearly proved to be highly non linear of the collective nuclear gluon distribution. In addition, it was seen that the pattern of non linearity for single-jet spectra depends highly on the relevant partonic subprocesses [146]. The breaking of linear k_T-factorization has been attested also in [169, 170]. This means that the color coupled channel aspect of the intranuclear color dipole evolution in general cannot be absorbed into a single nuclear UGD. We are aware of this limitation and the calculation presented here is based on phenomenological arguments. For instance, the nuclear structure functions have been well described using factorization for nuclear targets in Refs. [151, 171–173].

5.3 Exclusive Z^0 production

As discussed, the LHC has been studying physics at TeV scale allowing the access to unexplored kinematical regimes at large luminosities. This machine is able to search and study the physics beyond of the Standard Model (SM) with high accuracy. Traditionally, a baseline SM signal is the Z^0 production [174]. In proton-proton (pp) collisions, the hadronic Z^0 decays are not easy to identify due to the strong background of QCD multijet production from hadronic event environment [175]. The high-statistics measurements in final states with leptons are the main channel at the LHC. On the other hand, the exclusive production of Z^0 at electron-ion colliders or in ultra-peripheral collisions (UPCs) present some advantages. There is an increasing interest on exclusive processes at the LHC. [176, 177]. One of these favorable conditions is the processes to be perturbatively calculable with not so large uncertainties due to the high mass of the boson. Another feature is the clear experimental signature compared to the Z^0 signal coming from hadroproduction. A dedicated experimental search has already been done for $p\bar{p}$ collisions at the Tevatron [178]. No exclusive $Z \to \ell^+\ell^-$ candidates were observed leading to the first

upper limit on the exclusive Z^0 cross section, $\sigma(p\bar{p} \to pZ^0\bar{p}) < 0.96$ pb. Similar searches have been preliminarily carried out at the LHC [179]. Therefore, it is timely to investigate the prediction for both electron-ion colliders and ultra-peripheral collisions given their high energies and integrated luminosities (see Ref. [180] where prospects for exclusive processes which are complementary between the LHC and the Electron-Ion Collider - EIC are discussed).

The exclusive Z^0 photoproduction in electron-proton collisions was first addressed in the pioneering work of Ref. [181], where an analysis using non-forward QCD planar ladder diagrams was done and applied to diffractive (inclusive and semi-inclusive) boson production in ep colliders. The simple two-gluon exchange model of the Pomeron was used in Ref. [182] to compute the boson photoproduction cross section. There, a finite gluon mass has been included in the propagators to suppress the long distance contributions. In the context of the color dipole picture, the exclusive Z^0 production has been analyzed in both space-like [183] and time-like kinematics [143]. The equivalent calculation in $k_\perp$-factorization approach was presented first in Ref. [184]. In Refs. [143, 184], applications to photoproduction in pp collisions at the LHC energies were performed. The analysis for UPCs in pp, pA and AA collisions at the LHC has been done in Ref. [185].

Here, the main goal is to compute the exclusive Z^0 production cross section in ep and eA collisions by using the $k_\perp$- factorization formalism. Different models for the UGDs will be considered. We focus on the energies and phase spaces of the LHeC [186–188] and the FCC [189, 190] in eh mode, FCC-eh. Using the obtained cross section for Z^0 production in photon-proton and photon-nucleus processes, the corresponding predictions for pp and AA collisions are computed. In the last case, the cross section at the energies of the HL-LHC, HE-LHC and FCC are calculated. The sources of theoretical uncertainties are investigated. An important point to be highlighted is that here we extend our previous works on exclusive dilepton production in lepton-hadron and hadron-hadron machines [122, 191].

The calculation of exclusive Z^0 production cross section follows the same formalism of TCS (timelike Compton scattering) [122, 123, 191]. In the context of the k_T-factorization approach it was first proposed in Ref. [184] using only one model for the UGD. Afterwards, in Ref. [122] the present authors computed the TCS cross section for dilepton production in ep collisions by using different and updated UGDs. Specifically, four UGDs containing distinct physical information were analyzed. Moreover, in Ref. [191] we have accounted for dilepton production via TCS in electron-nucleus collisions assuming the UGD proposed in

Nucleus	LHeC/HL-LHeC	HE-LHeC	FCC-eA
O	0.92	1.27	2.45
Ar	0.87	1.21	2.32
Kr	0.85	1.18	2.27
Pb	0.81	1.13	2.18

Table 5.6 – Center-of-mass energies (in units of TeV) at future electron-nucleus colliders (LHeC/HL-LHeC, HE-LHeC and FCC-eA) for different nuclei.

Ref. [192]. Here, we will apply the following models for the UGD: Moriggi-Peccini-Machado - MPM [92], Ivanov-Nikolaev - IN [193] and Golec-Biernat-Wusthoff - GBW [113, 194] (the reader may review the previous section for further details on these models).

Comparing to TCS, one can calculate the cross section for exclusive Z^0 boson production by simply replacing the electromagnetic photon-quark coupling by the electroweak one, $ee_f \to \frac{eg_V^f}{sin2\theta_W}$, where θ_W is the Weinberg angle. Only the weak vector coupling is relevant, where $g_V^f = (I_3^f - 2e_f \sin^2\theta_W)/\sin 2\theta_W)$ [143]. The weak isospin of a quark of flavour f and charge ee_f is I_3^f. Along with the coupling replacement, one has also to redefine x in terms of the Z^0 mass:

$$x = \xi_{\rm sk}\left(\frac{M_Z^2}{W^2}\right), \tag{5.34}$$

where $\xi_{\rm sk}$ is inserted in order to correct the skewedness effect [123]. Following Ref. [184], the value $\xi_{\rm sk} = 0.41$ has been considered.

Taking the equation for the imaginary part of TCS amplitude expressed in Refs. [122, 123, 191] and performing the coupling replacement, one can obtain the forward amplitude for exclusive Z^0 production in ep collisions [184]:

$$\begin{aligned}\mathcal{M}^{\gamma p\to Z^0 p}(W,|t|=0) &= \sum_f \frac{2W^2\alpha_{em}g_V^f}{\pi} \\ &\times \int_0^1 dz\int d^2\vec{\kappa}_\perp \frac{(i+\rho_R){\rm Im}M_f(z,\vec{\kappa}_\perp)}{\kappa_\perp^2 + m_f^2 - z(1-z)M_Z^2 - i\varepsilon},\end{aligned} \tag{5.35}$$

where ρ_R is the ratio of real to imaginary part of amplitude. Moreover, m_f is the quark mass of flavor f and W^2 is the center-of-mass energy squared of the photon-proton system. The quantity ${\rm Im}M_f$ is defined in Eq. (5.23). The following hard scale $\mu^2 = \max(\kappa_\perp^2 + m_f^2, k_\perp^2)$ has been chosen. The corresponding amplitude for the $\gamma p \to Z^0 p$ process within the diffraction cone is written as

$$\mathcal{M}^{\gamma p\to Z^0 p}(W,|t|) = \mathcal{M}^{\gamma p\to Z^0 p}(W,|t|=0)e^{-B_D|t|}, \tag{5.36}$$

Collider	Nucleus	$\sigma_{ep(A)}$ (fb)	Number of events per year
HL-LHC	p	7.11	60.6
	O	70.3	3.28
	Pb	1.97×10^3	7.07
HE-LHC	p	10.9	140
	O	113	13.69
	Pb	3.27×10^3	30.09
FCC	p	30.9	494
	O	349	125.62
	Pb	1.04×10^4	287.98

Table 5.7 – Cross section in units of fb and event rates/year times branching ratio for exclusive Z^0 photoproduction in ep and eA collisions. The results are presented for the MPM UGD model as a baseline. Numerical calculation are presented for O and Pb nuclei.

where the energy dependent diffraction slope, B_D, is parametrized as $B_D = B_0 + 2\alpha'_{\text{eff}} \log(W^2/W_0^2)$. Here, $\alpha'_{\text{eff}} = 0.164$ GeV^{-2}, $B_0 = 3.5$ GeV^{-2} and $W_0 = 95$ GeV [184].

The differential and the integrated production cross sections are, respectively, given by

$$\frac{d\sigma}{dt}(\gamma p \to Z^0 p) = \frac{|\mathcal{M}(W,|t|)|^2}{16\pi}, \tag{5.37}$$

$$\sigma(\gamma p \to Z^0 p) = \frac{\left[\text{Im}(\mathcal{M}^{\gamma p \to Z^0 p})\right]^2 \left(1+\rho_R^2\right)}{16\pi B_D}. \tag{5.38}$$

The cross section in Eq. (5.38) will be evaluated for the LHeC (as well for its high luminosity and high energy upgrades) [3, 186–188] and for the FCC center-of-mass energies [189, 190]. These energies are summarized in Table 5.2. Concerning the quark flavours, u, d, s, c, b are considered.

For Z^0 production in nuclear collisions, we will investigate the nuclei proposed in the LHC prospects (see Refs. [121, 195, 196]), namely O, Kr, Ar and Pb. The energy of the nuclear beams are given by the energy of the proton beam multiplied by the ratio Z/A, where Z is the atomic number while A is the atomic mass number. In Table 5.6, we outline the beam energies along with the center-of-mass energies for electron-nucleus collisions. The energy of the electron beam is 60 GeV.

Interestingly, since for Z^0 production the hard scale associated with the process is $\mu^2 = m_Z r$, one expects that small dipoles (large $k_\perp$ gluons) will be the dominant contribution to the cross section. This means that $\mu^2 \gg Q_{s,A}(x)^2$ and the nuclear shadowing

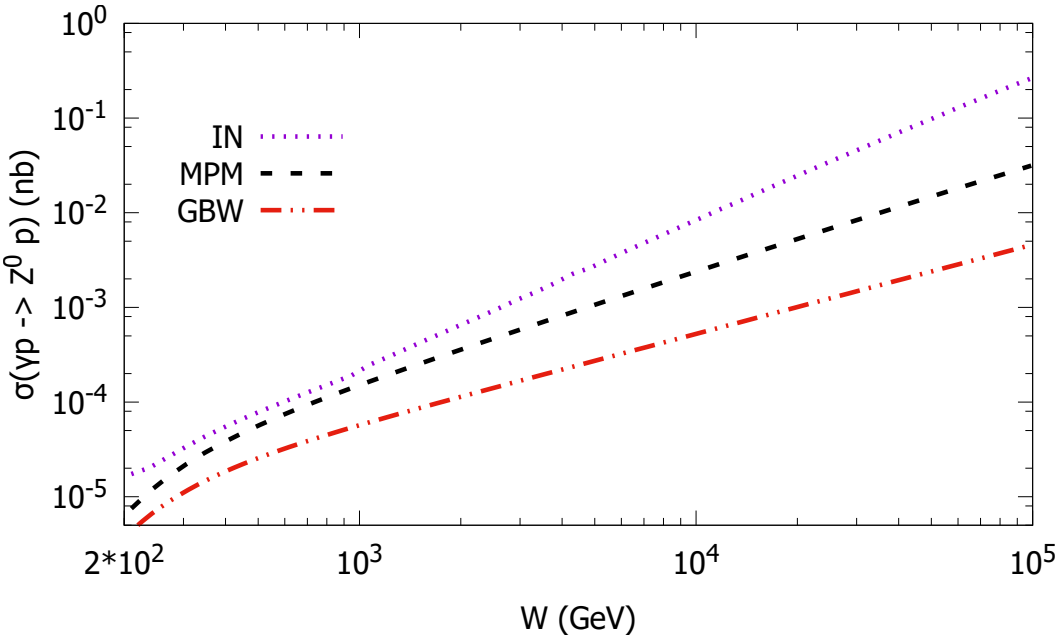

Figure 5.13 – Cross section $\sigma(\gamma^* p \to Z^0 p)$ as a function of photon-proton center-of-mass energy, $W_{\gamma p}$. Numerical results for IN, MPM and GBW phenomenological models are presented.

Table 5.8 – The event rates/year for exclusive Z^0 photoproduction in pp and PbPb collisions in different rapidity ranges. The results are presented for the MPM UGD model as a baseline.

Collider	**pp collisions**		**PbPb collisions**	
	$-2.0 < y < +2.0$	$+2.0 < y < +4.5$	$-2.0 < y < +2.0$	$+2.0 < y < +4.5$
HL-LHC	1.39×10^3	531	364	45.8
HE-LHC	8.15×10^3	461	1.33×10^3	183
FCC	7.54×10^3	6.60×10^4	5.92×10^4	8.31×10^3

should be quite small. A good approximation for the nuclear UGD would be $F_A(x, k_\perp) \approx AF_p(x, k_\perp)$.

Moving now to the numerical results, we first present the Z^0 photoproduction in γp scattering. The corresponding energies for the ep colliders are exhibited in Table 5.2. In Fig. 5.13 the predictions for the IN (dotted curve), MPM (dashed curve) and GBW (dot-dashed curve) models are shown as a function of photon-proton center- of-mass energy, $W_{\gamma p}$. In the TeV energy scale the cross section has the order of magnitude of $\sigma(\gamma^* p \to Z^0 p) \approx 0.1$ pb and a large theoretical uncertainty. Accordingly, the GBW model gives a lower bound for the cross section values and weaker energy behavior compared to MPM and IN. The reason is the DGLAP-like evolution embedded in both IN and MPM models for the UGD. The x value probed at $W_{\gamma p} = 1$ TeV is $\sim 10^{-3}$. The output coming from the MPM

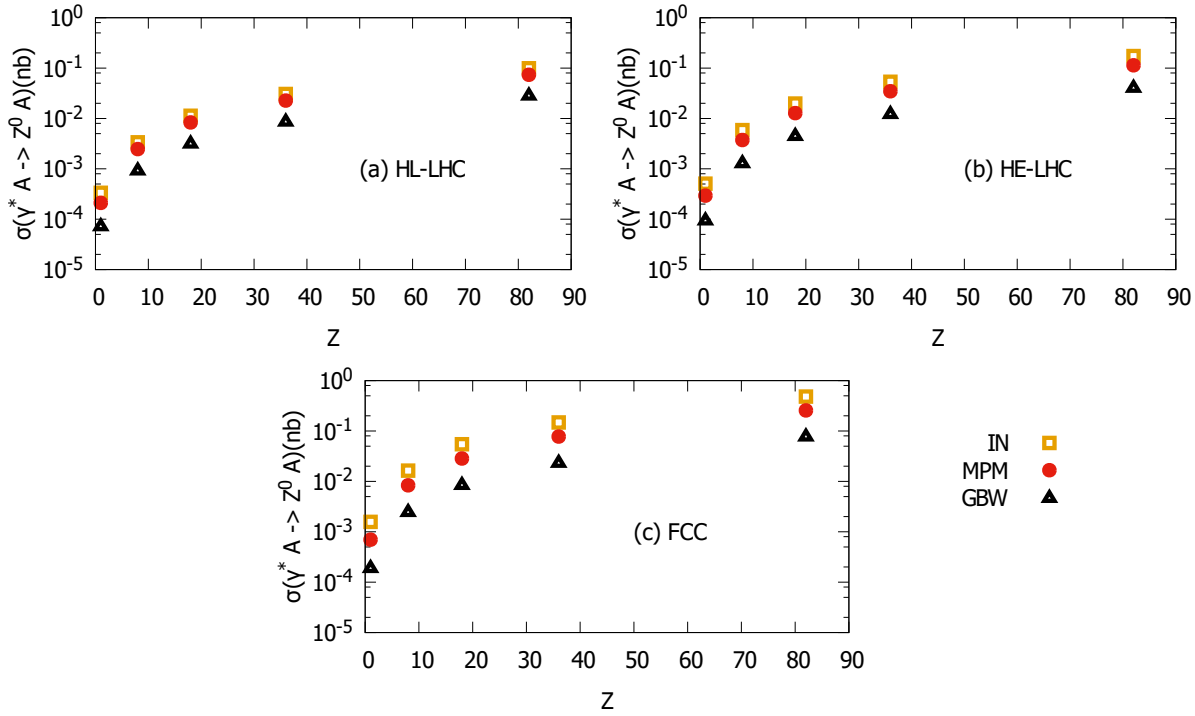

Figure 5.14 – Cross section $\sigma(\gamma^* p(A) \to Z^0 p(A))$ as a function of atomic number Z at the energies of (a) HL-LHC, (b) HE-LHC and (c) FCC. The predictions from IN, MPM and GBW models are shown for O, Ar, Kr, Pb nuclei and proton as well. The corresponding energies are presented in Tab. 5.6.

model can be parametrized in the following way: $\sigma_{\rm MPM}(\gamma p \to Z^0 p) = [180\,{\rm fb}]\,(W_{\gamma p}/W_0)^{1.13}$ (with $W_0 = 10^3\,{\rm GeV}$). Notice that the prediction from Ref. [184] is properly reproduced here by using the Ivanov-Nikolaev UGD. A steeper growth is predicted by Motyka and Watt (MW) in Ref. [143], where the color dipole picture is considered and by using the impact parameter saturation model (IP-SAT) and timelike Z^0 boson. The IP-SAT parametrization includes DGLAP evolution for the dipole cross section and the result scales as $\sigma_{\rm MW}(\gamma p \to Z^0 p) = [37\,{\rm fb}]\,(W_{\gamma p}/W_0)^{1.73}$, with $W_0 = 1.3 \times 10^3\,{\rm GeV}$.

The analyses for nuclear targets are presented in Fig. 5.14. Predictions from the three phenomenological models are shown for the nuclear species presented in Table 5.6 and for proton as a baseline. As examples of order of magnitude one has $\sigma(\gamma Pb \to Z^0 Pb) \approx 84.6\,(260)$ pb and $\sigma(\gamma O \to Z^0 O) \approx 2.46\,(8.3)$ pb at HL-LHC(FCC) energy. The dependence on atomic mass number from MPM model (for $A > 1$) is given by $\sigma^{\gamma A}_{\rm MPM} = \sigma_A\, A^\delta$, where $\sigma_A = 50.5$ fb and $\delta = 1.39$ at the HL-LHC and $\sigma_A = 216$ fb and $\delta = 1.33$ at the FCC. This result is consistent with the weak absorption limit for the nuclear dipole cross section typical for Z^0 production. In the figure the predictions are shown for $W^{max}_{\gamma A} = \sqrt{s_{eA}}$.

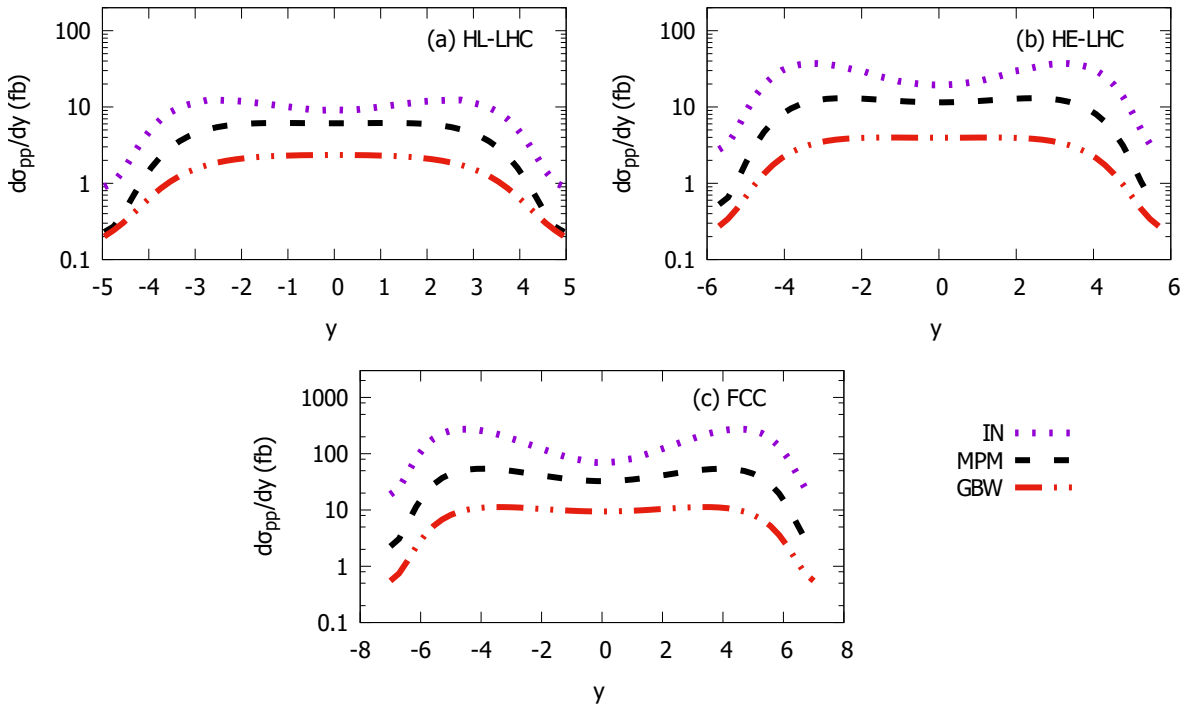

Figure 5.15 – Rapidity distribution for exclusive Z^0 production in pp collisions. Predictions are shown for the energies of (a) HL-LHC, (b) HE-LHC and (c) FCC.

In Table 5.7 the cross section times branching ratio into dileptons (in units of fb) is presented for ep and eA collisions. Here, the interest is in very small $Q^2 \ll 1$ GeV^2 range where the photoproduction cross section is independent of photon virtuality. Therefore, the $ep(A) \to eZ^0p(A)$ cross section can be written as

$$\begin{aligned} \frac{d\sigma}{dW^2} &= \frac{\alpha_{em}}{2\pi s}\left[\frac{1+(1-y)^2}{y}\ln\frac{Q^2_{max}}{Q^2_{min}} - \frac{2(1-y)}{y}\left(1-\frac{Q^2_{min}}{Q^2_{max}}\right)\right] \\ &\times \sigma^{\gamma p(A)}(W^2), \end{aligned} \tag{5.39}$$

where y is the inelasticity variable and $Q^2_{min} = m_e^2 y^2/(1-y)$. The corresponding number of events per year is also presented. The run with Oxigen is comparable in number of events with the proton target. The experimental feasibility is enhanced in eA case compared to the ep machine. This is specially important when kinematic cuts are imposed in order to remove the main dilepton QED background. The predictions considering the decay into hadrons is larger by a factor 20 but the experimental feasibility worsens.

Let us now move to ultra-peripheral collisions. The cross section to produce a Z^0 boson in a proton-proton collision within the Weizsäcker-Williams approximation is given by [125, 157, 197]

$$\sigma(pp \to pp + Z^0) = 2\int_0^\infty \frac{dn_\gamma^p}{d\omega}\sigma(\gamma + p \to Z^0 + p)\, d\omega,$$

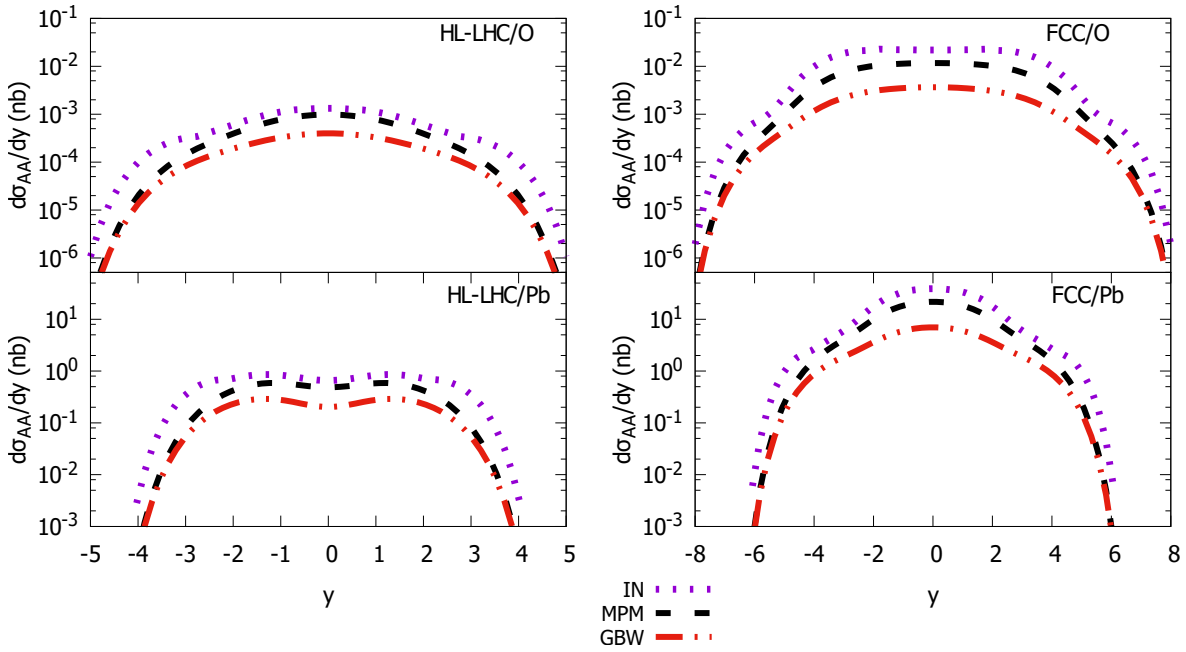

Figure 5.16 – Rapidity distribution for Z^0 production in AA collisions. Predictions are presented for Oxigen (upper plots) and Lead (lower plots) nuclei at the energies of HL-LHC (plots on the left) and FCC (plots on the right).

where ω is the photon energy and $dn^p_\gamma/d\omega$ is the photon spectrum for protons. In the numerical calculations, we have used the photon spectrum from Ref. [159]. The corresponding rapidity distribution is obtained as follows:

$$\frac{\sigma(pp \to pp + Z^0 p)}{dy} = \omega \frac{dn^p_\gamma}{d\omega} \sigma_{\gamma+p\to Z^0+p}(\omega), \tag{5.40}$$

in which the rapidity y of the produced Z^0 state with mass M_Z is related to the photon energy through $y = \ln(2\omega/M_Z)$. The rapidity distributions are shown in Fig. 5.15 and the the calculations are for collision energies of (a) the HL-LHC, (b) HE-LHC and (c) FCC colliders. The dotted, dashed and dot-dashed curves are the results for the IN, MPM and GBW UGDs, respectively. Here, the predictions are presented without absorption effects which depend on the rapidity. For instance, the absorptive correction at 14 TeV for $y = 0$ is $\langle S^2 \rangle \simeq 0.8$ whereas it is $\langle S^2 \rangle \simeq 0.6$ for $y = 2$ [184]. The theoretical uncertainty is still sizable. At the energy of HL-LHC, our predictions are in agreement with those in Refs. [143, 184, 185]. In general, the numerical results obtained using k_T-factorization approach are higher than those from color dipole framework. The rapidity distribution for higher hadron energies (HE-LHC and FCC) can be directly compared with the results of Ref. [185]. There, two dipole cross sections have been considered (bCGC and IP-SAT

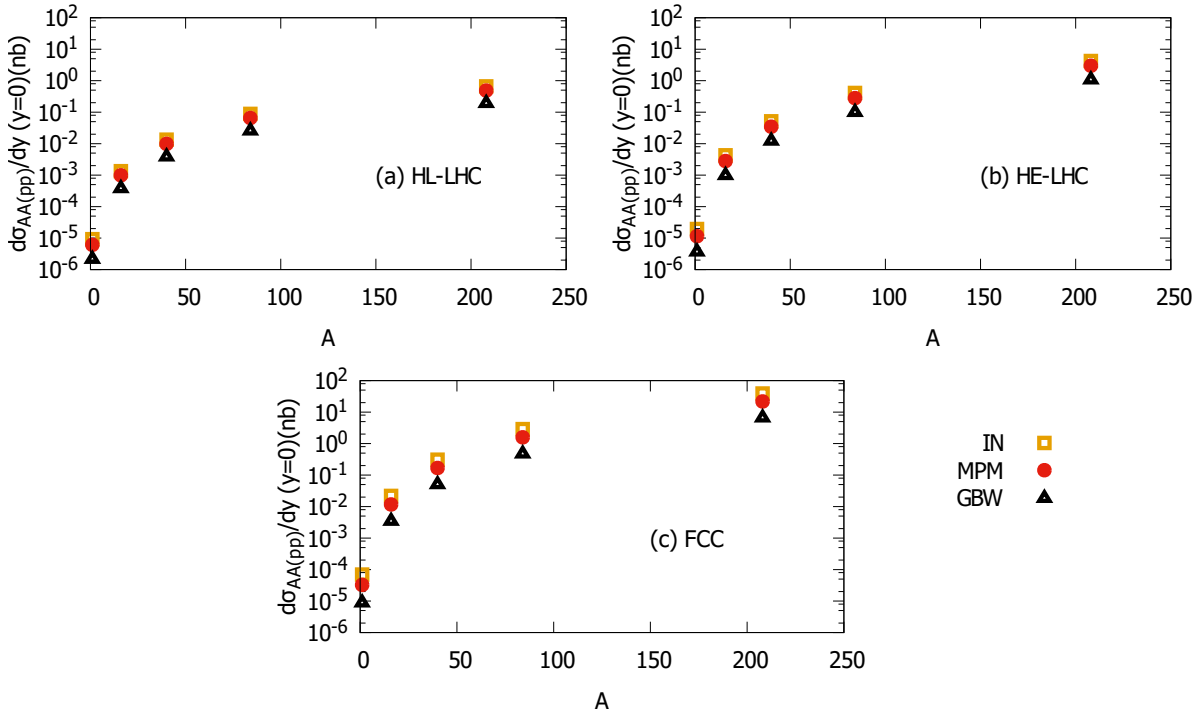

Figure 5.17 – Rapidity distribution for Z^0 production in AA collisions at mid-rapidity $y = 0$ as a function of the atomic mass number A. The predictions from IN, MPM and GBW models are shown for O, Ar, Kr, Pb nuclei and proton as well at the energies of (a) HL-LHC, (b) HE-LHC and (c) FCC.

models) within the color dipole picture. The order of magnitude of the cross sections are in agreement. The experimental feasibility is promising by using the dilepton decay channel. A careful analysis by using kinematic cuts should remove the large background coming from $\gamma\gamma \to \ell^+\ell^-$ process. The search for exclusive Z^0 production in proton-proton collisions can follow similar methodology employed in the corresponding search in $p\bar{p}$ collisions at Tevatron energies [178].

Finally, the Z^0 exclusive production is investigated in ultra-peripheral heavy ion collisions (UPCs). The corresponding rapidity distribution for the coherent production is given by [160]

$$\frac{\sigma(AA \to AZ^0A)}{dy} = \omega \frac{dn_\gamma^A}{d\omega} \sigma_{\gamma+A\to Z^0+A}(\omega), \tag{5.41}$$

where $dn_\gamma^A/d\omega$ is the photon spectrum for nuclei. The analytical photon flux for $b > 2R_A$ has been used in [157]. In Fig. 5.16 the rapidity distribution is shown for Oxigen (O) and Lead (Pb) nuclei: upper and lower plots, respectively. This is presented for the energies of HL-LHC and FCC. The predictions are somewhat larger than the ones presented in Ref. [185] where the color dipole approach is considered. There, $d\sigma_{AA}(y = 0)/dy \simeq 0.6$

nb in contrast with present calculation $d\sigma_{AA}(y=0)/dy \simeq 10$ nb. In both approaches the theoretical uncertainty is large, specially that one associated with the specific model for the dipole cross section or UGD.

In Fig. 5.17 the predictions for rapidity distributions at mid-rapidity, $y = 0$, are shown for the nuclear species presented in Table 5.6 as well as for protons. The cross sections are exhibited as a function of the atomic mass number A for the energies of (a) HL-LHC, (b) HE-LHC and (c) FCC. The predictions for MPM and IN models are quite similar at this scale and a lower bound is given by the GBW model.

In order to summarize the results for pp and PbPb collisions, in Table 5.8 the event rates/year are presented, where the production cross section has been multiplied by branching ratio for decays into dileptons. Two rapidity ranges are considered: $|y| \leq 2$ (central rapidities) and $+2.0 \leq y \leq +4.5$. (forward rapidities). Results are displayed for the MPM model as a representative example of application. The present calculation is more comprehensive than those in Ref. [185] since light nuclei are also taken into account.

6 Summary and Conclusions

Let us now summarize this study and discuss about the main takeaways and conclusions obtained from that.

The diffractive gluon jet production was studied in the small-β region, what is dominated by large diffractive mass, $M_X^2 \gg Q^2$. In the QCD color dipole picture, the main contribution comes from the $q\bar{q}g$ Fock state and the jet is associated with the soft gluon emitted. We studied the potential of the future EIC, LHeC and FCC-eA machines for the measurement of gluon jet diffractive cross section. In the TeV scale machines, one can reach $x_{I\!P} \sim 10^{-5}$ for a wide range of β, corresponding to nuclear saturation scale of order $Q_{s,A} \simeq 2$ GeV. A simplified model for the S-matrices has been used and we would like to point out the possible theoretical sources of uncertainty. As examples of such sources one has more realistic expressions for the dipole-nucleus amplitude (Glauber model, Glauber-Gribov model or numerical solutions of BK equation) or different ansatz for the nuclear saturation scale. Furthermore, we demonstrated that the nuclear saturation scale, $Q_{s,A}$, could be extracted from data as a function of $x_{I\!P}$ by measuring the peak in the differential cross section, $\kappa^2 d\sigma/d^2k_\perp dM_X$, in terms of jet transverse momentum. Correlated strategies for extracting saturation scale from data are already known in literature. For instance, in Ref. [198] the proton saturation scale $Q_{s,p}^2$ is obtained from the multiplicities of charged hadrons in pp collisions by using local parton-hadron duality and geometric scaling property (similar investigations were done for pA [199] and AA collisions [200]). We presented the probable region where the peaks occur, $\kappa \approx a \times Q_{s,A}(x_{I\!P})$ (a is a constant of order of unity), and it was shown that the quantity $\kappa^2\sigma^{\rm scaled}$ presents universal behavior in terms of the scaling variable, $\tau = \kappa/Q_s$. Summarizing, both the LHeC and the highest energy collider project, the FCC-eh, offer unprecedented capabilities for studying the diffractive jet production in photon dissociation both in ep and eA collisions.

Regarding timelike Compton scattering, we have investigated it for the first time in electron-nucleus collisions within the k_T-factorization. We calculated the cross sections for dilepton production at the center-of-mass energies of different machines. Through our fit of TCS cross section in terms of the atomic mass number, it is possible to predict this observable for any nucleus. Predictions are made for eA and ultraperipleral heavy ion collisions as well. This was an exploratory study and is based on the assumption

that k_T-factorization is applicable for nuclei. In that sense, it could be quite pertinent for performing future analyses on this topic as soon as experimental data at electron-ion facilities are available, enabling one to quantify the breaking of linear k_T-factorization.

Finally, the exclusive production of Z^0 boson is investigated in ep and eA collisions within the k_T-factorization formalism. The theoretical uncertainty is studied by comparing the results for different unintegrated gluon distributions available in literature. It was found that the corresponding variance is large when models containing parton saturation effects are contrasted to those where they are not applied. The analysis is done in the kinematic range of interest of EIC and the LHeC. As a by product the Z^0 photoproduction is also investigated in pp and AA collisions. The application was restricted to the coherent scattering and predictions for incoherent scattering would be valuable. A comprehensive study is done concerning different nuclear species relevant for the LHC future runs. The experimental measurement feasibility is briefly discussed. As already stressed out, Z^0 production is a traditional baseline SM signal and looking into it in the context of electron-ion collisions is potentially quite important for the investigation of the existing open questions concerning the SM.

Since the first electron-ion collider is still under way (the EIC is being built and will probably be available within 10 years), we performed several predictions related to processes whose measurements could be highly useful towards the study of the nuclear content through electron-ion collisions, especially if executed at high energy machines such as the LHeC and FCC whose center-of-mass energies reach the TeV scale and therefore are potentially ideal “QCD laboratories” as aforementioned.

Bibliography

[1] M. J. Tannenbaum. How hadron collider experiments contributed to the development of QCD: from hard-scattering to the perfect liquid. *Eur. Phys. J. H*, 43(2):119–183, 2018.

[2] A. Accardi et al. Electron Ion Collider: The Next QCD Frontier: Understanding the glue that binds us all. *Eur. Phys. J. A*, 52(9):268, 2016.

[3] P. Agostini et al. The Large Hadron-Electron Collider at the HL-LHC. 7 2020.

[4] F.D. Aaron et al. Combined Measurement and QCD Analysis of the Inclusive e+- p Scattering Cross Sections at HERA. *JHEP*, 01:109, 2010.

[5] Yuri L. Dokshitzer. Calculation of the Structure Functions for Deep Inelastic Scattering and e+ e- Annihilation by Perturbation Theory in Quantum Chromodynamics. *Sov. Phys. JETP*, 46:641–653, 1977. [Zh. Eksp. Teor. Fiz.73,1216(1977)].

[6] V. N. Gribov and L. N. Lipatov. Deep inelastic e p scattering in perturbation theory. *Sov. J. Nucl. Phys.*, 15:438–450, 1972. [Yad. Fiz.15,781(1972)].

[7] Guido Altarelli and G. Parisi. Asymptotic Freedom in Parton Language. *Nucl. Phys.*, B126:298–318, 1977.

[8] I. I. Balitsky and L. N. Lipatov. The Pomeranchuk Singularity in Quantum Chromodynamics. *Sov. J. Nucl. Phys.*, 28:822–829, 1978. [Yad. Fiz.28,1597(1978)].

[9] E. A. Kuraev, L. N. Lipatov, and Victor S. Fadin. The Pomeranchuk Singularity in Nonabelian Gauge Theories. *Sov. Phys. JETP*, 45:199–204, 1977. [Zh. Eksp. Teor. Fiz.72,377(1977)].

[10] I. Balitsky. Operator expansion for high-energy scattering. *Nucl. Phys.*, B463:99–160, 1996.

[11] Yuri V. Kovchegov. Small x F(2) structure function of a nucleus including multiple pomeron exchanges. *Phys. Rev.*, D60:034008, 1999.

[12] Jamal Jalilian-Marian, Alex Kovner, Andrei Leonidov, and Heribert Weigert. Unitarization of gluon distribution in the doubly logarithmic regime at high density. *Phys. Rev. D*, 59:034007, 1999. [Erratum: Phys.Rev.D 59, 099903 (1999)].

[13] Edmond Iancu, Andrei Leonidov, and Larry D. McLerran. The Renormalization group equation for the color glass condensate. *Phys. Lett. B*, 510:133–144, 2001.

[14] Matthew A.C. Lamont. The importance of e+A collisions at an Electron-Ion Collider. *J. Phys. Conf. Ser.*, 446:012051, 2013.

[15] Larry D. McLerran and Raju Venugopalan. Gluon distribution functions for very large nuclei at small transverse momentum. *Phys. Rev. D*, 49:3352–3355, 1994.

[16] Yuri V. Kovchegov. NonAbelian Weizsacker-Williams field and a two-dimensional effective color charge density for a very large nucleus. *Phys. Rev. D*, 54:5463–5469, 1996.

[17] Jamal Jalilian-Marian, Alex Kovner, Larry D. McLerran, and Heribert Weigert. The Intrinsic glue distribution at very small x. *Phys. Rev. D*, 55:5414–5428, 1997.

[18] Jamal Jalilian-Marian, Alex Kovner, Andrei Leonidov, and Heribert Weigert. The BFKL equation from the Wilson renormalization group. *Nucl. Phys. B*, 504:415–431, 1997.

[19] Elena Ferreiro, Edmond Iancu, Andrei Leonidov, and Larry McLerran. Nonlinear gluon evolution in the color glass condensate. 2. *Nucl. Phys. A*, 703:489–538, 2002.

[20] Alfred H. Mueller. A Simple derivation of the JIMWLK equation. 10 2001.

[21] V.P. Goncalves, M. V. T Machado, F.S. Navarra, and D. Spiering. Coulomb corrections to inclusive cross sections at the future Electron - Ion Collider. *Phys. Rev. C*, 97(1):015204, 2018.

[22] G.M. Peccini, L.S. Moriggi, and M.V.T. Machado. Investigating the diffractive gluon jet production in lepton-ion collisions. 3 2020.

[23] Yuri V. Kovchegov and Eugene Levin. *Quantum chromodynamics at high energy*, volume 33. Cambridge University Press, 8 2012.

[24] Michael E Peskin and Daniel V Schroeder. *An introduction to quantum field theory*. Westview, Boulder, CO, 1995. Includes exercises.

[25] Marek Matas. *Phenomenological studies of QCD at high energies*. PhD thesis, Czech Technical University in Prague, Prague, Czech Republic, 2020.

[26] Davison E. Soper. Parton distribution functions. *Nucl. Phys. B Proc. Suppl.*, 53:69–80, 1997.

[27] Michele Arneodo. Nuclear effects in structure functions. *Phys. Rept.*, 240:301–393, 1994.

[28] Richard P. Feynman. Very high-energy collisions of hadrons. *Phys. Rev. Lett.*, 23:1415–1417, 1969.

[29] M. Tanabashi et al. Review of Particle Physics. *Phys. Rev. D*, 98(3):030001, 2018.

[30] Curtis G. Callan, Jr. and David J. Gross. High-energy electroproduction and the constitution of the electric current. *Phys. Rev. Lett.*, 22:156–159, 1969.

[31] Alan D. Martin. Proton structure, Partons, QCD, DGLAP and beyond. *Acta Phys. Polon.*, B39:2025–2062, 2008.

[32] Lech Szymanowski. QCD collinear factorization, its extensions and the partonic distributions. *PoS*, QNP2012:015, 2012.

[33] Abhay Deshpande, Richard Milner, Raju Venugopalan, and Werner Vogelsang. Study of the fundamental structure of matter with an electron-ion collider. *Ann. Rev. Nucl. Part. Sci.*, 55:165–228, 2005.

[34] J. J. Aubert et al. The ratio of the nucleon structure functions $F2_n$ for iron and deuterium. *Phys. Lett. B*, 123:275–278, 1983.

[35] R. G. Arnold et al. Measurements of the a-Dependence of Deep Inelastic electron Scattering from Nuclei. *Phys. Rev. Lett.*, 52:727, 1984.

[36] M. Arneodo et al. The Structure Function ratios F2(li) / F2(D) and F2(C) / F2(D) at small x. *Nucl. Phys. B*, 441:12–30, 1995.

[37] M. R. Adams et al. Shadowing in inelastic scattering of muons on carbon, calcium and lead at low x(Bj). *Z. Phys. C*, 67:403–410, 1995.

[38] Nestor Armesto. Nuclear shadowing. *J. Phys. G*, 32:R367–R394, 2006.

[39] M. R. Adams et al. Shadowing in the muon xenon inelastic scattering cross-section at 490-GeV. *Phys. Lett. B*, 287:375–380, 1992.

[40] M. van der Heijden and C. Scholz. Structure function ratios: Recent results from NMC. In *25th Rencontres de Moriond: High-energy Hadronic Interactions*, pages 359–368, 1990.

[41] L. W. Whitlow. Deep Inelastic Structure Functions From Electron Scattering on Hydrogen, Deuterium, and Iron at 0.6-GeV$^2 \leq Q^2 \leq$ 30-GeV^2. Other thesis, 3 1990.

[42] M. J. Leitch et al. Nuclear effects on heavy quark production results from Fermilab experiments E772 and E789. *Nucl. Phys. A*, 544:197C–207C, 1992.

[43] D. Naples et al. NuTeV cross-section and structure function measurements. In *11th International Workshop on Deep Inelastic Scattering (DIS 2003)*, pages 104–108, 7 2003.

[44] Leo Stodolsky. Hadron-like behavior of gamma, neutrino nuclear cross-sections. *Phys. Rev. Lett.*, 18:135–137, 1967.

[45] D. Schildknecht. ON SHADOWING IN PHOTOPRODUCTION AND INELASTIC ELECTRON SCATTERING FROM COMPLEX NUCLEI. *Nucl. Phys. B*, 66:398–411, 1973.

[46] Nikolai N. Nikolaev and Valentin I. Zakharov. Parton Model and Deep Inelastic Scattering on Nuclei. *Phys. Lett. B*, 55:397–399, 1975.

[47] Graham Shaw. Shadowing in the Scaling Region. *Phys. Lett. B*, 228:125–128, 1989.

[48] Sergey A. Kulagin, G. Piller, and W. Weise. Shadowing, binding and off-shell effects in nuclear deep inelastic scattering. *Phys. Rev. C*, 50:1154–1169, 1994.

[49] Jan Kwiecinski and Barbara Maria Badelek. Unified Description of Nuclear Shadowing of Virtual Photons. *Phys. Lett. B*, 208:508–512, 1988.

[50] L. L. Frankfurt and M. I. Strikman. Shadowing and Enhancement of Quark Distributions in Nuclei at Small X. *Nucl. Phys. B*, 316:340–354, 1989.

[51] Stanley J. Brodsky and Hung Jung Lu. Shadowing and Antishadowing of Nuclear Structure Functions. *Phys. Rev. Lett.*, 64:1342, 1990.

[52] Nikolai N. Nikolaev and B. G. Zakharov. Color transparency and scaling properties of nuclear shadowing in deep inelastic scattering. *Z. Phys. C*, 49:607–618, 1991.

[53] V. Barone, M. Genovese, Nikolai N. Nikolaev, E. Predazzi, and B. G. Zakharov. Nonuniversality of structure functions and measurement of the strange sea density. *Phys. Lett. B*, 317:433–436, 1993.

[54] Boris Kopeliovich and Bogdan Povh. Scaling variable for nuclear shadowing in deep inelastic scattering. *Phys. Lett. B*, 367:329–334, 1996.

[55] N. Armesto and M. A. Braun. The EMC effect at low x in perturbative QCD. *Z. Phys. C*, 76:81–90, 1997.

[56] Stanley J. Brodsky, Ivan Schmidt, and Simonetta Liuti. Is the Momentum Sum Rule Valid for Nuclear Structure Functions ? 8 2019.

[57] Vincenzo Barone and Enrico Predazzi. *High-Energy Particle Diffraction*, volume v.565 of *Texts and Monographs in Physics*. Springer-Verlag, Berlin Heidelberg, 2002.

[58] B. L. Friman, V. R. Pandharipande, and Robert B. Wiringa. CALCULATIONS OF PION EXCESS IN NUCLEI. *Phys. Rev. Lett.*, 51:763–766, 1983.

[59] V. R. Pandharipande, J. Carlson, Steven C. Pieper, R. B. Wiringa, and R. Schiavilla. Isovector spin-longitudinal and -transverse response of nuclei. *Phys. Rev. C*, 49:789–801, Feb 1994.

[60] D. M. Alde, H. W. Baer, T. A. Carey, G. T. Garvey, A. Klein, C. Lee, M. J. Leitch, J. W. Lillberg, P. L. McGaughey, C. S. Mishra, J. M. Moss, J. C. Peng, C. N. Brown, W. E. Cooper, Y. B. Hsiung, M. R. Adams, R. Guo, D. M. Kaplan, R. L. McCarthy, G. Danner, M. J. Wang, M. L. Barlett, and G. W. Hoffmann. Nuclear dependence of dimuon production at 800 gev. *Phys. Rev. Lett.*, 64:2479–2482, May 1990.

[61] D. Gaskell et al. Longitudinal electroproduction of charged pions from H-1, H-2, He-3. *Phys. Rev. Lett.*, 87:202301, 2001.

[62] Jason R. Smith and Gerald A. Miller. Chiral solitons in nuclei: Saturation, emc effect, and drell-yan experiments. *Phys. Rev. Lett.*, 91:212301, Nov 2003.

[63] L. L. Frankfurt, M. I. Strikman, and S. Liuti. Evidence for enhancement of gluon and valence-quark distributions in nuclei from hard lepton-nucleus processes. *Phys. Rev. Lett.*, 65:1725–1728, Oct 1990.

[64] K. J. Eskola. Scale dependence of nuclear gluon structure. *Nucl. Phys. B*, 400:240–266, 1993.

[65] K. J. Eskola, V. J. Kolhinen, and C. A. Salgado. The Scale dependent nuclear effects in parton distributions for practical applications. *Eur. Phys. J. C*, 9:61–68, 1999.

[66] K. J. Eskola, V. J. Kolhinen, and P. V. Ruuskanen. Scale evolution of nuclear parton distributions. *Nucl. Phys. B*, 535:351–371, 1998.

[67] Dieter Schildknecht. Color Transparency and Saturation in QCD. *Subnucl. Ser.*, 50:45–65, 2014.

[68] R. Baier, D. Schiff, and B. G. Zakharov. Energy loss in perturbative QCD. *Ann. Rev. Nucl. Part. Sci.*, 50:37–69, 2000.

[69] Boris Z. Kopeliovich, Alexander V. Tarasov, and Andreas Schafer. Bremsstrahlung of a quark propagating through a nucleus. *Phys. Rev. C*, 59:1609–1619, 1999.

[70] P. L. McGaughey, J. M. Moss, and J. C. Peng. High-energy hadron induced dilepton production from nucleons and nuclei. *Ann. Rev. Nucl. Part. Sci.*, 49:217–253, 1999.

[71] Michael Leitch. New measurements of the nuclear dependencies of the j/psi and psi' resonances in high-energy proton-nucleus collisions. 04 2000.

[72] D. Naples et al. A-dependence of photoproduced dijets. *Phys. Rev. Lett.*, 72:2341–2344, 1994.

[73] J. W. Cronin, Henry J. Frisch, M. J. Shochet, J. P. Boymond, R. Mermod, P. A. Piroue, and Richard L. Sumner. Production of hadrons with large transverse momentum at 200, 300, and 400 GeV. *Phys. Rev. D*, 11:3105–3123, 1975.

[74] B. Z. Kopeliovich, J. Nemchik, E. Predazzi, and A. Hayashigaki. Nuclear hadronization: Within or without? *Nucl. Phys. A*, 740:211–245, 2004.

[75] A. Airapetian et al. Hadron formation in deep inelastic positron scattering in a nuclear environment. *Eur. Phys. J. C*, 20:479–486, 2001.

[76] M. R. Adams et al. Scaled energy (z) distributions of charged hadrons observed in deep inelastic muon scattering at 490-GeV from xenon and deuterium targets. *Phys. Rev. D*, 50:1836–1873, 1994.

[77] J. Ashman et al. Comparison of forward hadrons produced in muon interactions on nuclear targets and deuterium. *Z. Phys. C*, 52:1–12, 1991.

[78] M. R. Adams et al. Scaled energy (z) distributions of charged hadrons observed in deep inelastic muon scattering at 490-GeV from xenon and deuterium targets. *Phys. Rev. D*, 50:1836–1873, 1994.

[79] J. Ashman et al. Comparison of forward hadrons produced in muon interactions on nuclear targets and deuterium. *Z. Phys. C*, 52:1–12, 1991.

[80] W. Burkot et al. Nuclear attenuation of fast hadrons produced in charged current neutrino and anti-neutrino interactions in neon. *Z. Phys. C*, 70:47–53, 1996.

[81] M. Strikman, M. G. Tverskoii, and M. B. Zhalov. Soft neutron production in DIS: A Window to the final state interactions. *Phys. Lett. B*, 459:37–42, 1999.

[82] Enke Wang and Xin-Nian Wang. Jet tomography of hot and cold nuclear matter. *Phys. Rev. Lett.*, 89:162301, Oct 2002.

[83] T. Falter, W. Cassing, K. Gallmeister, and U. Mosel. Hadron formation and attenuation in deep inelastic lepton scattering off nuclei. *Phys. Lett. B*, 594:61–68, 2004.

[84] Alberto Accardi, Valeria Muccifora, and Hans-Juergen Pirner. Hadron production in deep inelastic lepton nucleus scattering. *Nucl. Phys. A*, 720:131–156, 2003.

[85] W. Cassing, K. Gallmeister, and C. Greiner. Quenching of high p-perpendicular hadrons by (pre)hadronic FSI at RHIC. *J. Phys. G*, 30:S801–S808, 2004.

[86] Jonathan Osborne and Xin-Nian Wang. Multiple parton scattering in nuclei: Twist four nuclear matrix elements and off forward parton distributions. *Nucl. Phys. A*, 710:281–302, 2002.

[87] G. P. Vacca. Small x QCD. In *16th Conference on High Energy Physics*, 8 2004.

[88] Krzysztof Golec-Biernat. *Deep inelastic scattering at small values of the Bkorken x variable*. PhD thesis, Kraków/Hamburg, 2001.

[89] Jeffrey R. Forshaw and D. A. Ross. *Quantum chromodynamics and the pomeron*, volume 9. Cambridge University Press, 1 2011.

[90] V. Barone, M. Genovese, Nikolai N. Nikolaev, E. Predazzi, and B. G. Zakharov. Unitarization of structure functions at large 1/x. *Phys. Lett. B*, 326:161–167, 1994.

[91] Nikolai N. Nikolaev and B. G. Zakharov. On determination of the large 1/x gluon distribution at HERA. *Phys. Lett. B*, 332:184–190, 1994.

[92] L.S. Moriggi, G.M. Peccini, and M.V.T. Machado. Investigating the inclusive transverse spectra in high-energy *pp* collisions in the context of geometric scaling framework. 5 2020.

[93] L. V. Gribov, E. M. Levin, and M. G. Ryskin. Semihard Processes in QCD. *Phys. Rept.*, 100:1–150, 1983.

[94] Alfred H. Mueller and Jian-wei Qiu. Gluon Recombination and Shadowing at Small Values of x. *Nucl. Phys.*, B268:427–452, 1986.

[95] Berndt Mueller. From rhic to the eic. Talk presented at the QEIC Workshop, Mumbai, India, January 4, 2020.

[96] Raju Venugopalan. Why we need an Electron-Ion Collider. *Annalen Phys.*, 528:131–137, 2016.

[97] J. L. Abelleira Fernandez et al. A Large Hadron Electron Collider at CERN: Report on the Physics and Design Concepts for Machine and Detector. *J. Phys. G*, 39:075001, 2012.

[98] Krzysztof J. Golec-Biernat and C. Marquet. Testing saturation with diffractive jet production in deep inelastic scattering. *Phys. Rev. D*, 71:114005, 2005.

[99] Miguel Arratia, Youqi Song, Felix Ringer, and Barbara V. Jacak. Jets as precision probes in electron-nucleus collisions at the future Electron-Ion Collider. *Phys. Rev. C*, 101(6):065204, 2020.

[100] Tolga Altinoluk, Néstor Armesto, Guillaume Beuf, and Amir H. Rezaeian. Diffractive Dijet Production in Deep Inelastic Scattering and Photon-Hadron Collisions in the Color Glass Condensate. *Phys. Lett. B*, 758:373–383, 2016.

[101] Yoshitaka Hatta, Bo-Wen Xiao, and Feng Yuan. Probing the Small- x Gluon Tomography in Correlated Hard Diffractive Dijet Production in Deep Inelastic Scattering. *Phys. Rev. Lett.*, 116(20):202301, 2016.

[102] V. Guzey and M. Klasen. Diffractive dijet photoproduction in ultraperipheral collisions at the LHC in next-to-leading order QCD. *JHEP*, 04:158, 2016.

[103] V. Guzey and M. Klasen. Inclusive dijet photoproduction in ultraperipheral heavy ion collisions at the CERN Large Hadron Collider in next-to-leading order QCD. *Phys. Rev. C*, 99(6):065202, 2019.

[104] Heikki Mäntysaari, Niklas Mueller, and Björn Schenke. Diffractive Dijet Production and Wigner Distributions from the Color Glass Condensate. *Phys. Rev. D*, 99(7):074004, 2019.

[105] Heikki Mäntysaari, Niklas Mueller, Farid Salazar, and Björn Schenke. Multigluon Correlations and Evidence of Saturation from Dijet Measurements at an Electron-Ion Collider. *Phys. Rev. Lett.*, 124(11):112301, 2020.

[106] Yoshitaka Hatta, Niklas Mueller, Takahiro Ueda, and Feng Yuan. QCD Resummation in Hard Diffractive Dijet Production at the Electron-Ion Collider. *Phys. Lett. B*, 802:135211, 2020.

[107] Farid Salazar and Björn Schenke. Diffractive dijet production in impact parameter dependent saturation models. *Phys. Rev. D*, 100(3):034007, 2019.

[108] R. Boussarie, A. V. Grabovsky, L. Szymanowski, and S. Wallon. Towards a complete next-to-logarithmic description of forward exclusive diffractive dijet electroproduction at HERA: real corrections. *Phys. Rev. D*, 100(7):074020, 2019.

[109] Cyrille Marquet. A QCD dipole formalism for forward-gluon production. *Nucl. Phys. B*, 705:319–338, 2005.

[110] Krzysztof J. Golec-Biernat and M. Wusthoff. Saturation in diffractive deep inelastic scattering. *Phys. Rev. D*, 60:114023, 1999.

[111] Cyrille Marquet. A Unified description of diffractive deep inelastic scattering with saturation. *Phys. Rev. D*, 76:094017, 2007.

[112] E. Iancu, K. Itakura, and S. Munier. Saturation and BFKL dynamics in the HERA data at small x. *Phys. Lett. B*, 590:199–208, 2004.

[113] Krzysztof Golec-Biernat and Sebastian Sapeta. Saturation model of DIS : an update. *JHEP*, 03:102, 2018.

[114] Nestor Armesto, Carlos A. Salgado, and Urs Achim Wiedemann. Relating high-energy lepton-hadron, proton-nucleus and nucleus-nucleus collisions through geometric scaling. *Phys. Rev. Lett.*, 94:022002, 2005.

[115] N. Armesto. A Simple model for nuclear structure functions at small x in the dipole picture. *Eur. Phys. J. C*, 26:35–43, 2002.

[116] J. Cepila, J. G. Contreras, and M. Matas. Predictions for nuclear structure functions from the impact-parameter dependent Balitsky-Kovchegov equation. *Phys. Rev. C*, 102(4):044318, 2020.

[117] Jan Cepila, Jesus Guillermo Contreras, and Michal Krelina. Coherent and incoherent J/ψ photonuclear production in an energy-dependent hot-spot model. *Phys. Rev. C*, 97(2):024901, 2018.

[118] D. Bendova, J. Cepila, and J. G. Contreras. Dissociative production of vector mesons at electron-ion colliders. *Phys. Rev. D*, 99(3):034025, 2019.

[119] Oliver Brüning and Max Klein. Exploring the energy frontier with deep inelastic scattering at the LHC. *J. Phys. G*, 46(12):123001, 2019.

[120] Néstor Armesto, Paul R. Newman, Wojciech Słomiński, and Anna M. Staśto. Inclusive diffraction in future electron-proton and electron-ion colliders. *Phys. Rev. D*, 100(7):074022, 2019.

[121] Frederick Bordry, Michael Benedikt, Oliver Brüning, John Jowett, Lucio Rossi, Daniel Schulte, Steinar Stapnes, and Frank Zimmermann. Machine Parameters and Projected Luminosity Performance of Proposed Future Colliders at CERN. 10 2018.

[122] G. M. Peccini, L. S. Moriggi, and M. V. T. Machado. Dilepton production through timelike Compton scattering within the k_T -factorization approach. *Phys. Rev. D*, 102(9):094015, 2020.

[123] W. Schafer, G. Slipek, and A. Szczurek. Exclusive diffractive photoproduction of dileptons by timelike Compton scattering. *Phys. Lett. B*, 688:185–191, 2010.

[124] Gabriela Kubasiak and Antoni Szczurek. Inclusive and exclusive diffractive production of dilepton pairs in proton-proton collisions at high energies. *Phys. Rev. D*, 84:014005, 2011.

[125] Spencer Klein and Peter Steinberg. Photonuclear and Two-photon Interactions at High-Energy Nuclear Colliders. 5 2020.

[126] Wolfgang Schäfer. Photon induced processes: from ultraperipheral to semicentral heavy ion collisions. *Eur. Phys. J. A*, 56(9):231, 2020.

[127] V.P. Gonçalves, M.M. Jaime, D.E. Martins, and M.S. Rangel. Exclusive and diffractive $\mu^+\mu^-$ production in pp collisions at the LHC. *Phys. Rev. D*, 97(7):074024, 2018.

[128] M. Diehl. *Generalized parton distributions*. PhD thesis, 2003.

[129] Xiangdong Ji. Generalized parton distributions. *Annual Review of Nuclear and Particle Science*, 54(1):413–450, 2004.

[130] A.V. Belitsky and A.V. Radyushkin. Unraveling hadron structure with generalized parton distributions. *Phys. Rept.*, 418:1–387, 2005.

[131] M. Boër, M. Guidal, and M. Vanderhaeghen. Timelike Compton scattering off the proton and generalized parton distributions. *Eur. Phys. J. A*, 51(8):103, 2015.

[132] Edgar R. Berger, M. Diehl, and B. Pire. Time - like Compton scattering: Exclusive photoproduction of lepton pairs. *Eur. Phys. J. C*, 23:675–689, 2002.

[133] J. Wagner, B. Pire, F. Sabatié, L. Szymanowski, and H. Moutarde. Next to leading order analysis of DVCS and TCS. *EPJ Web Conf.*, 66:06016, 2014.

[134] Dieter Müller, D. Robaschik, B. Geyer, F.-M. Dittes, and J. Hořejši. Wave functions, evolution equations and evolution kernels from light ray operators of QCD. *Fortsch. Phys.*, 42:101–141, 1994.

[135] Johannes Blumlein, Bodo Geyer, and Dieter Robaschik. The Virtual Compton amplitude in the generalized Bjorken region: twist-2 contributions. *Nucl. Phys. B*, 560:283–344, 1999.

[136] Xiang-Dong Ji. Gauge-Invariant Decomposition of Nucleon Spin. *Phys. Rev. Lett.*, 78:610–613, 1997.

[137] A.V. Radyushkin. Nonforward parton distributions. *Phys. Rev. D*, 56:5524–5557, 1997.

[138] O. Grocholski, H. Moutarde, B. Pire, P. Sznajder, and J. Wagner. Data-driven study of timelike Compton scattering. *Eur. Phys. J. C*, 80(2):171, 2020.

[139] J.P. Lansberg, L. Szymanowski, and J. Wagner. Lepton-pair production in ultraperipheral collisions at AFTER@LHC. *JHEP*, 09:087, 2015.

[140] Magno V.T. Machado. Investigating the exclusive photoproduction of dileptons at high energies. *Phys. Rev. D*, 78:034016, 2008.

[141] C. Brenner Mariotto and M.V.T. Machado. Inclusive and exclusive dilepton photoproduction at high energies. *Phys. Rev. D*, 87(5):054028, 2013.

[142] Magno V.T. Machado. Nuclear DVCS at small-x using the color dipole phenomenology. *Eur. Phys. J. C*, 59:769–776, 2009.

[143] L. Motyka and G. Watt. Exclusive photoproduction at the Tevatron and CERN LHC within the dipole picture. *Phys. Rev. D*, 78:014023, 2008.

[144] R.J. Glauber. Cross-sections in deuterium at high-energies. *Phys. Rev.*, 100:242–248, 1955.

[145] Alfred H. Mueller. Small x Behavior and Parton Saturation: A QCD Model. *Nucl. Phys. B*, 335:115–137, 1990.

[146] N.N. Nikolaev, W. Schafer, B.G. Zakharov, and V.R. Zoller. Nonlinear k-perpendicular factorization for forward dijets in DIS off nuclei in the saturation regime. *J. Exp. Theor. Phys.*, 97:441–465, 2003.

[147] N.N. Nikolaev and W. Schafer. Breaking of k perpendicular-factorization for single jet production off nuclei. *Phys. Rev. D*, 71:014023, 2005.

[148] N.N. Nikolaev, W. Schafer, and B.G. Zakharov. Nonuniversality aspects of nonlinear k-perpendicular-factorization for hard dijets. *Phys. Rev. Lett.*, 95:221803, 2005.

[149] N.N. Nikolaev and W. Schafer. Quenching of Leading Jets and Particles: The p perp Dependent Landau-Pomeranchuk-Migdal effect from Nonlinear k perp Factorization. *Phys. Rev. D*, 74:014023, 2006.

[150] M.A. Betemps and M.V.T. Machado. A Simple model for the nuclear unintegrated gluon distribution. *Eur. Phys. J. C*, 65:427–431, 2010.

[151] E.G. de Oliveira, A.D. Martin, F.S. Navarra, and M.G. Ryskin. Unintegrated parton distributions in nuclei. *JHEP*, 09:158, 2013.

[152] Prithwish Tribedy and Raju Venugopalan. QCD saturation at the LHC: Comparisons of models to p + p and A + A data and predictions for p + Pb collisions. *Phys. Lett. B*, 710:125–133, 2012. [Erratum: Phys.Lett.B 718, 1154–1154 (2013)].

[153] Adrian Dumitru, Andre V. Giannini, Matthew Luzum, and Yasushi Nara. Particle multiplicities in the central region of high-energy collisions from k_T-factorization with running coupling corrections. *Phys. Lett. B*, 784:417–422, 2018.

[154] H. De Vries, C.W. De Jager, and C. De Vries. Nuclear charge-density-distribution parameters from elastic electron scattering. *Atomic Data and Nuclear Data Tables*, 36(3):495 – 536, 1987.

[155] M. Arneodo et al. The A dependence of the nuclear structure function ratios. *Nucl. Phys. B*, 481:3–22, 1996.

[156] M. Arneodo et al. The Q**2 dependence of the structure function ratio F2 Sn / F2 C and the difference R Sn - R C in deep inelastic muon scattering. *Nucl. Phys. B*, 481:23–39, 1996.

[157] Spencer Klein and Joakim Nystrand. Exclusive vector meson production in relativistic heavy ion collisions. *Phys. Rev. C*, 60:014903, 1999.

[158] B. Pire, L. Szymanowski, and J. Wagner. Can one measure timelike Compton scattering at LHC? *Phys. Rev. D*, 79:014010, 2009.

[159] Manuel Drees and D. Zeppenfeld. Production of Supersymmetric Particles in Elastic *ep* Collisions. *Phys. Rev. D*, 39:2536, 1989.

[160] Carlos A. Bertulani, Spencer R. Klein, and Joakim Nystrand. Physics of ultra-peripheral nuclear collisions. *Ann. Rev. Nucl. Part. Sci.*, 55:271–310, 2005.

[161] J.T. Boyd. LHC Run-2 and Future Prospects. In *2019 European School of High-Energy Physics*, 1 2020.

[162] C. Marquet, Robert B. Peschanski, and G. Soyez. Exclusive vector meson production at HERA from QCD with saturation. *Phys. Rev. D*, 76:034011, 2007.

[163] H. Kowalski, L. Motyka, and G. Watt. Exclusive diffractive processes at HERA within the dipole picture. *Phys. Rev. D*, 74:074016, 2006.

[164] Spencer Klein, A.H. Mueller, Bo-Wen Xiao, and Feng Yuan. Lepton Pair Production Through Two Photon Process in Heavy Ion Collisions. *Phys. Rev. D*, 102(9):094013, 2020.

[165] C. Azevedo, V.P. Gonçalves, and B.D. Moreira. Exclusive dilepton production in ultraperipheral *PbPb* collisions at the LHC. *Eur. Phys. J. C*, 79(5):432, 2019.

[166] Victor P. Goncalves, Daniel E. Martins, and Murilo S. Rangel. Exclusive dilepton production at forward rapidities in *PbPb* collisions. 12 2020.

[167] Mariola Kłusek-Gawenda, Wolfgang Schäfer, and Antoni Szczurek. Centrality dependence of dilepton production via $\gamma\gamma$ processes from Wigner distributions of photons in nuclei. 12 2020.

[168] Mateusz Dyndal, Alexander Glazov, Marta Luszczak, and Renat Sadykov. Probing the photonic content of the proton using photon-induced dilepton production in p+Pb collisions at the LHC. *Phys. Rev. D*, 99(11):114008, 2019.

[169] Jean Paul Blaizot, Francois Gelis, and Raju Venugopalan. High-energy pA collisions in the color glass condensate approach. 2. Quark production. *Nucl. Phys. A*, 743:57–91, 2004.

[170] Jamal Jalilian-Marian and Yuri V. Kovchegov. Inclusive two-gluon and valence quark-gluon production in DIS and pA. *Phys. Rev. D*, 70:114017, 2004. [Erratum: Phys.Rev.D 71, 079901 (2005)].

[171] M. Modarres and A. Hadian. The EMC ratios of ^4He, ^3He and ^3H nuclei in the k_t factorization framework using the Kimber–Martin–Ryskin unintegrated parton distribution functions. *Nucl. Phys. A*, 983:118–132, 2019.

[172] M. Modarres and A. Hadian. Application of the Kimber-Martin-Ryskin and Martin-Ryskin-Watt unintegrated parton distributions to the EMC ratio of a ^{6}Li nucleus in the k_t-factorization framework. *Phys. Rev. D*, 98(7):076001, 2018.

[173] M.A. Betemps and M.V.T. Machado. Photon plus heavy quark production in high energy collisions within the target rest frame formalism. *Phys. Rev. D*, 82:094025, 2010.

[174] J. Berryhill and A. Oh. Electroweak physics at the LHC. *Journal of Physics G Nuclear Physics*, 44(2):023001, February 2017.

[175] RT Chislett. *Studies of hadronic decays of high transverse momentum W and Z bosons with the ATLAS detector at the LHC*. PhD thesis, University College London, 09 2014.

[176] M. G. Albrow, T. D. Coughlin, and J. R. Forshaw. Central Exclusive Particle Production at High Energy Hadron Colliders. *Prog. Part. Nucl. Phys.*, 65:149–184, 2010.

[177] L. A. Harland-Lang, V. A. Khoze, and M. G. Ryskin. Exclusive physics at the LHC with SuperChic 2. *Eur. Phys. J. C*, 76(1):9, 2016.

[178] T. Aaltonen et al. Search for exclusive Z boson production and observation of high mass $p\bar{p} \to \gamma\gamma \to p + \ell\ell + \bar{p}$ events in $p\bar{p}$ collisions at $\sqrt{s} = 1.96$ TeV. *Phys. Rev. Lett.*, 102:222002, 2009.

[179] Miguel Medina Jaime. *Produção exclusiva de bósons Z em colisões pp no experimento CMS/LHC*. PhD thesis, Campinas State U., 2015.

[180] Martin Hentschinski et al. White Paper on Forward Physics, BFKL, Saturation Physics and Diffraction. 3 2022.

[181] Jochen Bartels and M. Loewe. The Nonforward QCD Ladder Diagrams. *Z. Phys. C*, 12:263, 1982.

[182] Jon Pumplin. Diffractive photoproduction of Z0. 12 1996.

[183] V.P. Goncalves and M.V.T. Machado. Diffractive photoproduction of Z0 bosons in coherent interactions at CERN-LHC. *Eur. Phys. J. C*, 56:33–38, 2008. [Erratum: Eur.Phys.J.C 61, 351 (2009)].

[184] A. Cisek, W. Schafer, and A. Szczurek. Production of Z0 bosons with rapidity gaps: Exclusive photoproduction in gamma p and pp collisions and inclusive double diffractive Z0's. *Phys. Rev. D*, 80:074013, 2009.

[185] R.O. Coelho and V.P. Gonçalves. Exclusive z0 photoproduction at the large hadron collider and the future circular collider. *Nuclear Physics B*, 956:115013, 2020.

[186] J. L. Abelleira Fernandez et al. A Large Hadron Electron Collider at CERN: Report on the Physics and Design Concepts for Machine and Detector. *J. Phys. G*, 39:075001, 2012.

[187] P. Agostini et al. The Large Hadron-Electron Collider at the HL-LHC. *J. Phys. G*, 48(11):110501, 2021.

[188] K. D. J. André et al. An experiment for electron-hadron scattering at the LHC. *Eur. Phys. J. C*, 82(1):40, 2022.

[189] A. Abada et al. FCC Physics Opportunities: Future Circular Collider Conceptual Design Report Volume 1. *Eur. Phys. J. C*, 79(6):474, 2019.

[190] A. Abada et al. FCC-hh: The Hadron Collider: Future Circular Collider Conceptual Design Report Volume 3. *Eur. Phys. J. ST*, 228(4):755–1107, 2019.

[191] G. M. Peccini, L. S. Moriggi, and M. V. T. Machado. Exclusive dilepton production via timelike Compton scattering in heavy ion collisions. *Phys. Rev. D*, 103(5):054009, 2021.

[192] L. S. Moriggi, G. M. Peccini, and M. V. T. Machado. The role of nuclear gluon distribution on particle production in heavy ion collisions. 12 2020.

[193] I.P. Ivanov and Nikolai N. Nikolaev. Anatomy of the differential gluon structure function of the proton from the experimental data on F(2p) (x, Q**2). *Phys. Rev. D*, 65:054004, 2002.

[194] Krzysztof J. Golec-Biernat and M. Wusthoff. Saturation effects in deep inelastic scattering at low Q**2 and its implications on diffraction. *Phys. Rev. D*, 59:014017, 1998.

[195] Z. Citron et al. Report from Working Group 5: Future physics opportunities for high-density QCD at the LHC with heavy-ion and proton beams. *CERN Yellow Rep. Monogr.*, 7:1159–1410, 2019.

[196] S. Amoroso et al. Snowmass 2021 whitepaper: Proton structure at the precision frontier. 3 2022.

[197] Spencer R. Klein, Joakim Nystrand, Janet Seger, Yuri Gorbunov, and Joey Butterworth. STARlight: A Monte Carlo simulation program for ultra-peripheral collisions of relativistic ions. *Comput. Phys. Commun.*, 212:258–268, 2017.

[198] Takeshi Osada and Takuya Kumaoka. Saturation momentum scale extracted from semi-inclusive transverse spectra in high-energy pp collisions. *Phys. Rev. C*, 100(3):034906, 2019.

[199] Larry McLerran and Michal Praszalowicz. Fluctuations and the rapidity dependence of charged particles spectra in fixed centrality bins in pA collisions. *Annals Phys.*, 372:215–225, 2016.

[200] C. Andres, A. Moscoso, and C. Pajares. Universal geometrical scaling for hadronic interactions. *Nucl. Phys. A*, 901:14–21, 2013.

APPENDIX A – Light-cone coordinates

In the light-cone coordinate system, the collision occurs in the z-axis (longitudinal direction). Adopting the following definitions for the velocity and position four-vectors:

$$v^\mu = (v^0, v^1, v^2, v^3) \ , \ x^\mu = (x^0, x^1, x^2, x^3) \ , \tag{A.1}$$

these variables are defined in the light-cone frame as follows:

$$v^+ = \frac{1}{\sqrt{2}}(v^0 + v^3) \ , \ \frac{1}{\sqrt{2}}(v^0 - v^3) \ , \ v_\perp = (v^1, v^2) \ . \tag{A.2}$$

Hence, one shall define *time* within this frame:

$$x^+ = \frac{1}{\sqrt{2}}(t + z) \ , \tag{A.3}$$

and the *longitudinal* coordinate:

$$x^- = \frac{1}{\sqrt{2}}(t - z) \ . \tag{A.4}$$

The scalar product between momentum and position four-vectors read as

$$p.x = p^- x^+ p^+ x^- - p_\perp x_\perp \ , \tag{A.5}$$

whose result is

$$p^- x^+ p^+ x^- = p^0 x^0 - p^3 x^3 \ . \tag{A.6}$$

The variable p^- is conjugated to x^+ and therefore is termed *energy* in the light-cone frame, while p^+ is conjugated to x^- and called *longitudinal momentum*. For on-shell particles,

$$p^\pm = \frac{1}{\sqrt{2}}(E \pm p_z) \ , \tag{A.7}$$

where E is the total relativistic energy given by $E = \sqrt{\vec{p^2} + m^2}$. Consequently,

$$p^+ p^- = \frac{1}{2}(E^2 - p_z^2) = \frac{1}{2}(m^2 - \vec{p^2} - p_z^2) \ . \tag{A.8}$$

Thus,

$$p^+ p^- = \frac{1}{2}(m^2 + p_\perp^2) = \frac{1}{2} m_\perp^2 \ , \tag{A.9}$$

where $m_\perp$ is called *transverse mass*.

The variable *rapidity* is written in the light-cone frame as

$$y = \frac{1}{2}\ln\left(\frac{E + p_z}{E - p_z}\right) = \frac{1}{2}\ln\left(\frac{p^+}{p^-}\right) = \frac{1}{2}\ln\left(\frac{2p^{+2}}{m_\perp^2}\right) \ . \tag{A.10}$$

Utilizing the light-cone coordinates is convenient because, at high energies, $x^- \approx 0$ and $x^+ \approx 0$. Besides, if there is a boost, $p^+ \to ap^+$ and $p^- \to (1/a)p^-$, where a is an arbitrary constant. Hence, the rapidity is simply transformed as $y \to y + a$.

APPENDIX B – Sudakov parametrization

Consider the two light-like vectors a and b, called *Sudakov vectors*, whose definitions are the following:

$$a_\mu = \frac{1}{\sqrt{2}}(\Lambda, 0, 0, \Lambda) \ , \tag{B.1}$$

$$b_\mu = \frac{1}{\sqrt{2}}(\Lambda^{-1}, 0, 0, \Lambda^{-1}) \ , \tag{B.2}$$

in which Λ is an arbitrary number. These vectors satisfy

$$a^2 = b^2 = 0 \ , \ a.b = 1 \ , \ b^+ = a^- = 0 \ . \tag{B.3}$$

In the light-cone coordinate system, they are written as

$$a^\mu = (\Lambda, 0, \vec{0}_\perp) \ , \tag{B.4}$$

$$b^\mu = (0, \Lambda^{-1}, \vec{0}_\perp) \ . \tag{B.5}$$

Using the Sudakov parameters, a generic vector A^μ is represented as

$$A^\mu = \alpha a^\mu + \beta b^\mu + A^\mu_\perp$$

$$= (A.b) \ a^\mu + (A.a) \ b^\mu + A^\mu_\perp \ . \tag{B.6}$$

where $A^\mu_\perp = (0, \vec{0}_\perp, 0)$.

APPENDIX C – List of publications

C.1 Published articles

1. G. M. Peccini, L. S. Moriggi and M. V. T. Machado. Exclusive dilepton production via timelike Compton scattering in heavy ion collisions. *Phys. Rev. D*, 103:054009, 2021.

2. L. S. Moriggi, G. M. Peccini and M. V. T. Machado. Role of nuclear gluon distribution on particle production in heavy ion collisions. *Phys. Rev. D*, 103:034025, 2021.

3. G. M. Peccini, L. S. Moriggi and M. V. T. Machado. Dilepton production through timelike Compton scattering within the k_T-factorization approach. *Phys. Rev. D*, 102:094015, 2020.

4. L. S. Moriggi, G. M. Peccini and M. V. T. Machado. Investigating the inclusive transverse spectra in high energy pp collisions in the context of geometric scalling framework. *Phys. Rev. D*, 102:034016, 2020.

5. G. M. Peccini, L. S. Moriggi and M. V. T. Machado. Investigating the diffractive gluon jet production in lepton-ion collisions. *Phys. Rev. C*, 102:034903, 2020.

6. G. M. Peccini, F. Kopp, M. V. T. Machado and D. A. Fagundes. Soft diffraction within the QCD color dipole picture. *Phys. Rev. D*, 101:074042, 2020.

7. G. M. Peccini, L. S. Moriggi and M. V. T. Machado. Exclusive Z^0 production in ep and eA collisions at high energies. *Phys.Rev.D*, 106:014002, 2022.

C.2 Press release - Resumo simplificado tipo nota de imprensa (in Portuguese)

Há cerca de um século atrás os cientistas estudavam o átomo e buscavam entender como são constituídos. Entre os objetos que o compõem, o elétron foi o primeiro a ser descoberto, o que ocorreu em 1897 por Joseph John Thomson. Posteriormente, através do espalhamento de Rutherford, descobríamos o próton em 1919. Por fim, em 1932 detectou-se a existência do nêutron.

À medida que avançávamos no século XX, a física moderna foi alcançando grandes feitos, buscando investigar a matéria em escalas cada vez menores e explorar seu nível subatômico. Na década de 60, temos o surgimento da Eletrodinâmica Quântica, teoria que explica uma das quatro interações fundamentais que temos na natureza, o eletromagnetismo. Tal teoria se deve especialmente aos feitos do grande físico Richard Feynman, o qual viria a receber o Nobel de física em 1965. Logo após, já na década de 70, desenvolvemos a Cromodinâmica Quântica, teoria que descreve a interação forte, outra das quatro forças presentes na natureza. Entre os físicos que trabalharam nessa teoria, destaca-se o nome de Murray Gell-Mann, também agraciado com um prêmio Nobel de física em 1969.

Estudar a interação forte não é uma tarefa simples devido à complexidade matemática envolvida e também a muitos fenômenos que ainda não têm explicação ou verificação experimental. O núcleo atômico, formado por prótons e nêutrons, se mantém coeso devido à interação forte. Se essa não existisse, podemos pensar que simplesmente os prótons atrairiam os elétrons e assim o átomo entraria em colapso. Porém, com tal interação é possível manter um núcleo de prótons e nêutrons.

A interação forte leva esse nome não por acaso, pois é a mais intensa dentre as quatro forças fundamentais presentes na natureza: forte, eletromagnética, fraca e gravitacional. Além disso, tem um comportamento contrário à interação eletromagnética, ou seja, sua intensidade diminui à medida que os objetos se aproximam.

Este trabalho visa estudar as colisões entre elétrons e núcleos de átomos ionizados, tais como o chumbo, ouro, criptônio e, com isso, investigar a força forte. O elétron é um excelente microscópio para investigação do núcleo atômico e, devido a isso, existe uma grande expectativa por parte da comunidade científica para com a construção de um colisor elétron - íon. Dessa forma, o departamento de energia dos EUA (em inglês, Department of Energy - DoE), aprovou o projeto do EIC – Electron Ion Collider (em português, Colisor

Elétron - Íon), localizado no Brookhaven National Laboratory - EUA, o qual começou a ser construído há dois anos e provavelmente levará cerca de dez para ser finalizado. Tal feito possibilitará que se estude o núcleo atômico de forma detalhada e profunda e permitirá que os físicos entendam questões ainda em aberto na teoria da Cromodinâmica Quântica.

O fato é que ainda não podemos prever todos os avanços tecnológicos que virão com o estudo aprofundado do núcleo atômico. Há cem anos atrás ninguém previa que o estudo do átomo daria origem a tudo que possuímos hoje, desde a Química até os aparelhos eletrônicos que usamos no nosso cotidiano. Sendo assim, por ora é difícil prever tudo que será alcançado com os avanços na investigação do núcleo atômico. Todavia, temos aplicações tecnológicas imediatas já, como por exemplo a terapia por feixe de prótons (em inglês, Proton Beam Therapy), um dos tratamentos mais modernos contra o câncer e que é devido principalmente ao grande avanço tecnológico atingido através da construção de aceleradores de partículas nas últimas décadas. Não temos certeza sobre como será futuro, mas podemos ter certeza de que o progresso da ciência sempre será importante para o desenvolvimento da humanidade.

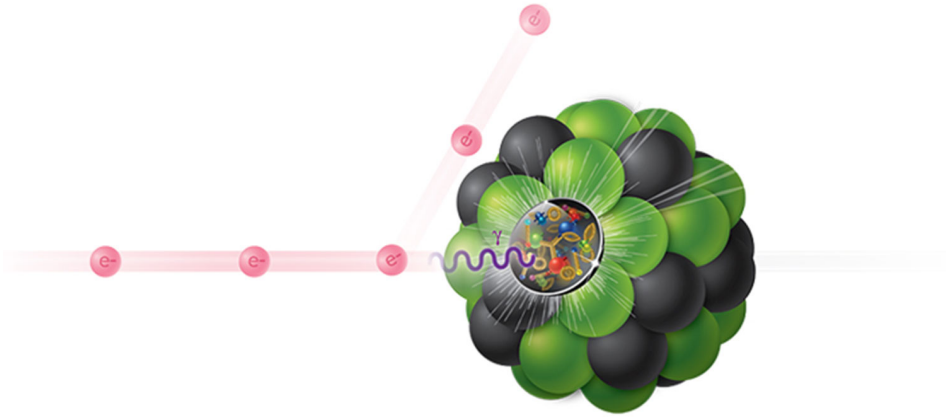

Imagem ilustrativa de uma colisão elétron - núcleo.